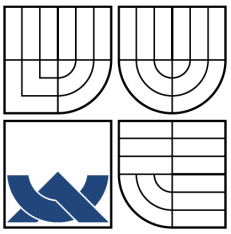

VYSOKÉ UČENÍ TECHNICKÉ V BRNĚ
BRNO UNIVERSITY OF TECHNOLOGY

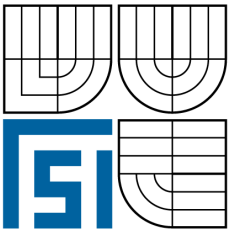

FAKULTA STROJNÍHO INŽENÝRSTVÍ
ÚSTAV FYZIKÁLNÍHO INŽENÝRSTVÍ
FACULTY OF MECHANICAL ENGINEERING
INSTITUTE OF PHYSICAL ENGINEERING

VÝVOJ A APLIKACE METOD ZAŘÍZENÍ PRO STUDIUM LOKÁLNÍCH VLASTNOSTÍ NANOSTRUKTUR

DEVELOPMENT AND APPLICATION OF METHODS USED IN DEVICES FOR STUDY OF LOCAL PROPERTIES OF NANOSTRUCTURES

DIPLOMOVÁ PRÁCE
DIPLOMA THESIS

AUTOR PRÁCE
AUTHOR

ONDŘEJ SHÁNĚL

VEDOUCÍ PRÁCE
SUPERVISOR

prof. RNDr. TOMÁŠ ŠIKOLA, CSc.

BRNO 2008

Abstrakt
Vývoj UHV kompatibilního kombinovaného systému AFM/SEM. Modifikace předchozího AFM mikroskopu pro podmínky spojené s tímto systémem. Výzkum transportu elektrického náboje v organických solárních článcích pomocí měření jejich volt-ampérových charakteristik a povrchového potenciálu. Příprava zlatých hrotů pro STM netoxickou cestou.

Summary
Development of UHV compatible combined AFM/SEM system. Modification of a former AFM microscope to meet requirements related to this task. Investigation of charge transport processes in organic solar cells by I-V measurements and the surface potential. Non-toxic fabrication of STM gold tips.

Klíčová slova
AFM, KP - AFM, SEM, modifikace AFM mikroskopu,UHV komora, organické sluneční články, volt-ampérová charakteristika organických slunečních článků, transport náboje v organických polovodičových zařízeních, příprava zlatých hrotů pro STM

Keywords
AFM, KP - AFM, SEM, modification of AFM microscope, UHV chamber, organic solar cells, I-V characterisctic of organic solar cells, charge transport process in organic semiconductor devices, preparation of STM gold tip

SHÁNĚL, O. *Vývoj a aplikace metod zařízení pro studium lokálních vlastností nanostruktur*. Brno: Vysoké učení technické v Brně, Fakulta strojního inženýrství, 2008. 130 s. Vedoucí diplomové práce prof. RNDr. Tomáš Šikola, CSc.

Prohlášení

Prohlašuji, že jsem tuto diplomovou práci vypracoval samostatně, pouze pod odborným vedením prof., RNDr. Tomáše Šikoly, CSc. a s použitím literatury, kterou uvádím v seznamu.

V Brně 21. května 2008

Acknowledgments

I would like to thank to prof. RNDr. Tomáš Šikola, CSc. for managing my diploma project, to Ing. David Škoda, Ing. Jakub Zlámal, PhD. and Ing. Radek Kalousek, PhD. for correcting my diploma thesis, to Ing. Filip Lopour, PhD. for many stimulating advises in the construction of AFM and vacuum chambers, to Ing. Jan Neuman and Ing. Zdeněk Nováček for helping with the practical aspects of completing the AFM microscope.

I would like to thank to Ms. C. Klára Maturová for assistance and patience related to work on organic solar cells, to Dr. Martijn Kemerink for advices in interpretation of results on measurements of organic solar cells, and to Ms. C. Wytze Keuning for deposition of spacer layers, Ms. C. Frank Veldhoven and Ms. C. Jan Gilot for helping with the preparation of solar cells, Ms. C. Dimitri S. H. Charrier and Erik-Jan Geluk for SEM picturers of gold tips, Ms. C. Wijnand Dijkstra and Ms. C. Gerard Wijers for the help with proposing of the set up for the etching of gold tips.

I would like to thank my mother for her support during my studies at Brno University of Technology.

The great word of thanks beholds to Mgr. Milada Húsková, my teacher at the grammar school, for opening my mind towards mathematics and physics.

At the end I thank to my fiance Marcela Volná for standing by me in beautiful and bad times.

Contents

List of abbreviations

AE	Auger electrons
AFM	Atomic Force Microscopy
AL	active layer
BSE	back scattered electrons
CL	cathodolumiscence
CPD	contact potential difference
EDX	Energy Dissipative X-ray spectroscopy
FMD	frequency modulation demodulator
HOMO	high occupied molecular orbital
ITO	indium tin oxide
KP - AFM	Kelvin Probe - Atomic Force Microscopy
LUMO	low occupied molecular orbitals
MDMO - PPV	poly[2-methoxy-5-(3´,7´-dimethyloctyloxy)-1,4-phenylenevinylene]
PCBM	methano-fullerene[6,6]-phenyl C_{61}-byturic acid methyl ester
PEDOT:PSS	poly(3,4-ethylenedioxythiophene) poly(styrenesulfonate)
PSPD	position sensitive photo - diode
rpm	revolutions per minute
SAM	Scanning Auger Microscopy
SC	solar cell
SE	secondary electrons
SEM	Scanning Electron Microscopy
SFM	Scanning Force Microscopy
SL	spacer layer
SSS - MARRA	Sháněl-Šikola-Spousta Miscellaneous Atomic Resolution Research Apparatus
STM	Scanning Tunneling Microscopy
STS	Scanning Tunneling Spectroscopy
UHV	ultra high vacuum

Chapter 1

Introduction

Nowadays there is an intensive research in the fields of surface science and related areas (including nanotechnology). New problems require more and more sophisticated investigations as higher resolution and using several analytic techniques together. A combined system of Atomic Force Microscopy (AFM) and Scanning Electron Microscopy (SEM) seems to be a promising device for it. The first part of this diploma project is continuation and extension of a previous project done in the Institute of Physical Engineering at Brno University of Technology. The schematic setup of the combined AFM/SEM system and the modification of the former AFM for this system are presented.

The second part of this diploma thesis deals with research on charge transport processes in organic solar cells. They belong to one of alternative energy sources. They are low-cost but their efficiency is very small (around 5 %). Understanding of the charge transport process helps to overcome this disadvantage. Spacer layer of Al_2O_3 or TiO_2 is used to block charge carriers and its investigation is done by I - V measurements and Kelvin Probe Force Microscopy.

Scanning Tunneling Force Microscopy (STM) is now widely exploited in surface and materials science. Commonly used tungsten or platinum tips have a disadvantage under air conditions. They become oxidized a thin layer of their has higher the higher work function than a pure metal. From this reason gold was chosen as the material for a STM tip under air environment. Easy, fast and reproducible way how to prepare them is reported in the last part of this diploma thesis.

Chapter 2

Scanning Force Microscopy

2.1. Introduction

The first scanning force microscope was developed in Switzerland by researchers of IBM Gerd Binnig, Calvin F. Quate and Christopher Gerber in 1986 [1]. They showed how to investigate a sample surface using this instrument with truly atomic spatial resolution. The basic principle of Scanning Force Microscopy is based on the measurement of an interaction forces between the probe and the sample.

This invention sparked a great boom in the research of surfaces and nanostructures in technology, physics, biology and chemistry. Gerd Binnig and Heindrich Rohrer were awarded the Nobel Price in 1986 for invention of this instrument.

Nowadays many variations of Scanning Force Microscopy (SFM) exist varying on the type of detectable forces. Scanning Force Microscopy techniques include Scanning Tunneling Microscopy, Atomic Force Microscopy, Electric Force Microscopy, Magnetic Force Microscopy, Magnetic Resonance Force Microscopy and many other microscopic methods.

2.2. Basic concept

Scanning Force Microscopy is a sort of scanning microscopy based on detection of force between the probe and the sample. This technique visualizes the topography or more precisely the map of force interactions [2]. This detection of the force is realized in the following way. A sharp tip interacting with the sample surface is mounted at the end of a cantilever. The deflection of the cantilever is measured by the deflection detection system. The signal from the detection system is processed by the processing unit (see Fig. 2.1) [2]. The deflection of the cantilever is proportional to the acting force. If the mechanical properties of the cantilever are known this force can be calculated.

2.3. Forces detectable in Scanning Force Microscopy

There are many forces affecting the tip of the cantilever. The most important forces will be described in the following text.

The total force is equal to the sum of all forces acting on the cantilever. It is important to stress different acting range of each force. It can be divided into two groups:

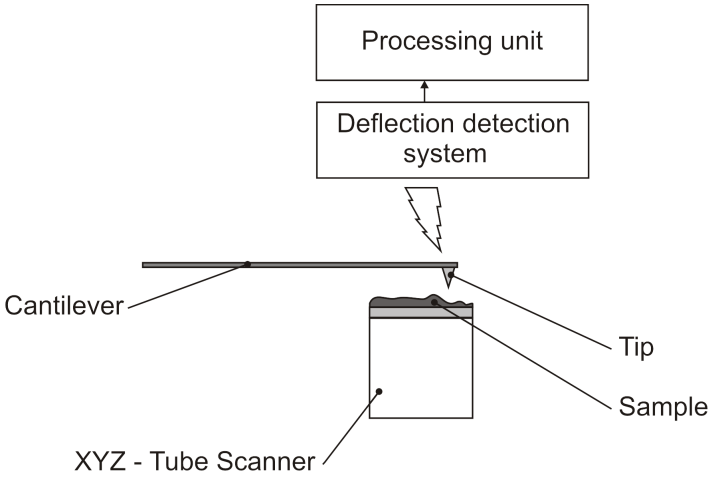

Fig. 2.1: The schematic setup of the SFM microscope.

- **Short range:** These forces originates from the outermost atoms of the tip and the sample, for example the short-range force [2,3],
- **Long range:** They originate from the whole volume of the cantilever, for example the electrostatic force, van der Waals force [2,3], etc.

The description of the total interaction between the tip and the cantilever is complex. The Mie´s potential

$$w(r) = -\frac{A}{r^n} + \frac{B}{r^m}, \tag{2.1}$$

can be used as a good approximation [4], where A and B are positive constants, r is distance between two atoms, m and n are positive integral numbers. The special case of Mie´s potential is Lennard-Jones potential [4]

$$w(r) = 4w_0 \left[\left(\frac{\sigma}{r} \right)^{12} - \left(\frac{\sigma}{r} \right)^{6} \right], \tag{2.2}$$

where σ is the constant ($w(\sigma) = 0$), w_0 is a minimum potential in the equilibrium state. The total force can be expressed as

$$F(r) = -\nabla w = 24w_0 \left[\frac{2\sigma^{12}}{r^{13}} - \frac{\sigma^6}{r^7} \right]. \tag{2.3}$$

The dependance of the total potential and the total force on the distance between two atoms is in Fig. 2.2. The equilibrium position of the atom is in the distance r_0, where the total potential is equal w_0. The total force is attractive in the region from r_0 to infinity and repulsive in the region from zero to r_0.

2.3.1. Short-range force

Short-range force originates from overlapping the wave functions of electrons of the outermost tip areas and sample atoms. This force is attractive when the overlapping of the

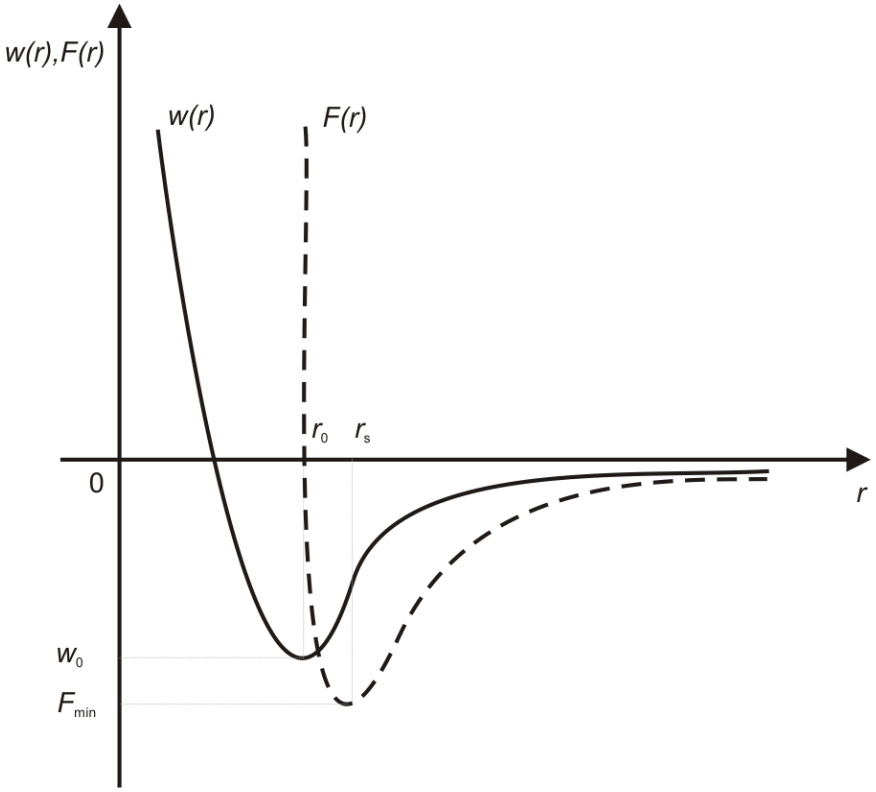

Fig. 2.2: Schematic dependance of total potential and force between two atoms.

wave function of electrons minimizes the total potential of the sample tip system. The force becomes repulsive, when the overlay increases the total energy of the system [2].

Typical interaction range of short-range forces goes from 0.2 nm to 0.5 nm and their magnitude is in the range from 0.2 nN to 1 nN [2].

2.3.2. Van der Waals force

Van der Waals force is force of a dipole-dipole character. It comes from electron fluctuations in an atom shell. These fluctuations act like temporary dipoles being attracted in accordance with the Coulomb law. The van der Waals forces are limited in distance. They become weak when interatomic distances are larger than the distance the light travels during typical lifetime of the electron fluctuation. The van der Waals force F_{vdW} can be calculated as [3]

$$F_{\mathrm{vdW}} = -\nabla W_{\mathrm{TS}}, \tag{2.4}$$

where W_{TS} is an interaction energy between the sample and the tip. The interaction energy W_{TS} can be expressed as

$$W_{\mathrm{TS}} = \int_{\mathrm{V_T}} \int_{\mathrm{V_S}} w(r - r') n_{\mathrm{T}} n_{\mathrm{S}} dV_{\mathrm{T}} dV_{\mathrm{S}}, \tag{2.5}$$

where $w(r - r')$ is the attractive part of the Lennard-Jones potential (see equation 2.2), n_{T} and n_{S} are densities of atoms in the tip and the sample respectively, V_{T} and V_{S} are the volumes of the tip and the sample respectively, r and r' are position vectors in the tip and the sample respectively (see Fig. 2.3). The van der Waals force for two atoms is particulary $F_{\mathrm{vdW}} \sim \frac{1}{r^7}$ for distance smaller than 5 nm and $F_{\mathrm{vdW}} \sim \frac{1}{r^8}$ beyond this limit [2].

It is difficult to calculate the van der Waals force between macroscopic objects by the equations 2.4 and 2.5. A good approximation can be done by Lifshits theory. The tip of

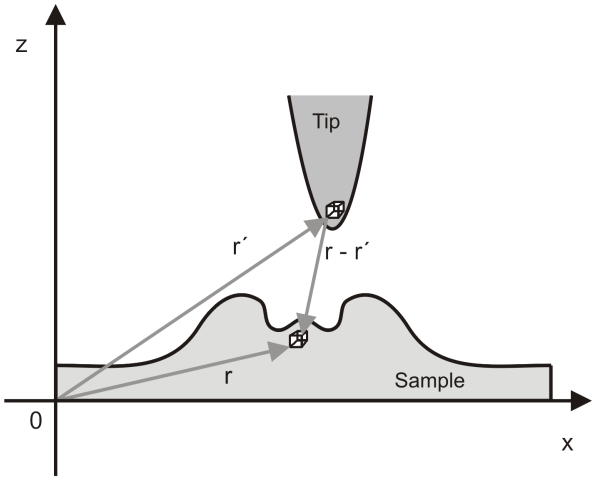

Fig. 2.3: The tip and the sample.

the cantilever is approximated as a sphere and the sample is defined as an infinit plane. Then the force is expressed as [2]

$$F_{\mathrm{vdW}} = \frac{HR}{6D^2}, \tag{2.6}$$

where H denotes the Hamaker constant, R is the tip radius and D is the distance between the sample and the sphere approximating the cantilever. The Hamaker constant is in the order of 10^{-19} J. The van der Waals force for values $R = 20\,\mathrm{nm}$, $D = 0.5\,\mathrm{nm}$ is $F_{\mathrm{vdW}} = 1.3\,\mathrm{nN}$.

The van der Waals force can be determined with higher precession. A realistic truncated cone shape of the cantilever has to be consider. This calculation shows the interaction between the the tip apex and the sample is dominated [5].

It is important to mention the influence of the medium between the cantilever and the sample on the resultant van der Waals force. It can be predicted using simplified Lifshits theory the relation between the van der Waals force and the permeabilities of the materials as [2]

$$F_{\mathrm{vdW}} \sim \frac{\varepsilon_1 - \varepsilon_3}{\varepsilon_2 - \varepsilon_3}, \tag{2.7}$$

where ε_1 is the permeability of the cantilever, ε_2 is the permeability of the sample and ε_3 is the permeability of the medium.

It is clear from equation 2.7 the resultant van der Waals force can be adjusted to a required value by using an appropriate medium. This technique can be used for increasing the resolution in liquids [2].

2.3.3. Electrostatic force

Electrostatic force originates between localized charges or between the conductive materials of different work functions [2, 3]. It is important for the detection of electrostatic forces when one charge is localized on the tip and the second one on the sample. The electrostatic force F_{es} can be calculated from Coulomb law [6]

$$F_{\mathrm{es}} = \frac{1}{4\pi\varepsilon_{\mathrm{r}}\varepsilon_0}\frac{q_1 q_2}{r^2}, \tag{2.8}$$

where ε_0 is the permeability of vacuum, ε_r is the relative permeability of a medium and r is the distance between the charge at the tip q_1 and the sample q_2. The real shape of the tip and the sample has to be taken into account. The electrostatic force can be calculated in the same way as the van der Waals force

$$F_\mathrm{es} = \int_{V_\mathrm{T}} \int_{V_\mathrm{S}} \frac{1}{4\pi\varepsilon\varepsilon_0} \frac{n_{q_\mathrm{T}} n_{q_\mathrm{S}}}{(r - r')^2} \mathrm{d}V_\mathrm{T} \mathrm{d}V_\mathrm{S}, \tag{2.9}$$

where n_{q_T} and n_{q_S} are the charge densities of the tip and the sample respectively, V_T and V_S are the volumes of the tip and the sample respectively, r and r' are position vectors (see Fig. 2.3).

The charge on the sample can be created in various ways, e.g. by [2]:

- ion bombardment,
- RTG exposure,
- cleaving sample in the vacuum,
- charge injection from the tip of the STM/AFM.

The charge on the sample can persist for hours in air and for days in the vacuum [2].

2.3.4. Magnetic force

The magnetic force is caused by the interaction of magnetic dipoles.

The typical setup for measurement of the magnetic force is as follows. A ferromagnetic particle or thin magnetic layer is mounted on the tip of the cantilever and the magnetic domains are present on the sample. The magnetic force can be calculated as [2]

$$\vec{F}_\mathrm{mg} = \nabla(\vec{\mu} \cdot \vec{B}), \tag{2.10}$$

where $\vec{\mu}$ is the magnetic moment of a dipole and $\vec{B}$ is the magnetic induction generated by the second body. If there are more magnetic domains or a domain is large, then it is necessary to sum contributions of each domain or of each small part of large domain on the magnetic dipole localized at the cantilever. The magnetic force is then [2]

$$\vec{F}_\mathrm{mg} = -\nabla \int_{V_\mathrm{T}} \vec{m}_\mathrm{T} \vec{B} dV_\mathrm{T}, \tag{2.11}$$

where m_T is the magnetic moment of a small dipole on the cantilever, $\vec{B}$ is the magnetic induction generated by magnetic dipoles of the sample in the site of the cantilever, V_T is the volume of the tip.

2.3.5. Capillary force

Capillary force comes from environments where a surface is covered by a thin layer of liquid or by condensed water bridges between the tip and the surface (see Fig. 2.4). The capillary force acts always on the sample covered by a liquid layer. There are some conditions on capillary force acting in the vapour environments. The water meniscus

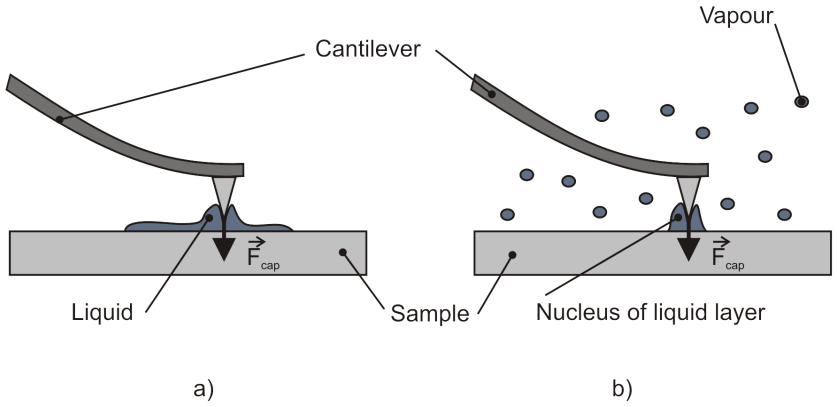

Fig. 2.4: The capillary force in a) liquid layer and in b) vapour environments.

between the cantilever and the sample can be formed when its radius R is smaller or equal to the so-called Kelvin radius R_{K} which is equal [2]

$$R_{\mathrm{K}} = \frac{\gamma V}{RT \log \frac{p}{p_{\mathrm{S}}}}, \tag{2.12}$$

where γ is the surface tension, V is the molar volume, R is the gas constant, T is the temperature, p is the pressure and p_{S} is the saturated vapor pressure. The value of the Kelvin radius for water vapour is 25 nm at temperature $T = 300\,\mathrm{K}$ and pressure ratio $\frac{p}{p_{\mathrm{S}}} = 0.95$.

The capillary force can be estimated as [4]

$$F_{\mathrm{cap}} = \frac{4\pi R_{\mathrm{T}} \gamma \cos\Theta}{1 + \frac{D}{R_{\mathrm{T}}(1-\cos\phi)}}, \tag{2.13}$$

where R_{T} is the radius of tip curvature, Θ is the contact angle, D is the distance between the sample and the tip, ϕ is the angle of the meniscus.

The typical value of the capillary force is in the range of $10^{-8}\,\mathrm{N}$ - $10^{-7}\,\mathrm{N}$.

2.4. Detection system

There are a few ways how to detect the deflection of the cantilever. The detection system has to be very sensitive because the deflections of the cantilever are in the order of $10^{-1}\,\mathrm{nm}$ - $10^{0}\,\mathrm{nm}$. The most used detection system are:

- **Optical beam system:** The laser beam is reflected from the rear side of the cantilever and than detected by a position sensitive photodiode (PSPD) (see Fig. 2.5 a). PSPD is made of four photodiodes. This detection system enables the detection of vertical and horizontal deflections. The deflection is determined as the difference in illumination ΔI on photodiodes as [2, 3]

  $$\Delta I_{\mathrm{v}} = (I_1 + I_2) - (I_3 + I_4) \tag{2.14}$$

  in the vertical direction and as

  $$\Delta I_{\mathrm{h}} = (I_1 + I_3) - (I_2 + I_4) \tag{2.15}$$

in the horizontal direction, where I_1, I_2, I_3 and I_4 denote the illumination of the first, the second, the third and the fourth part of the photodiode respectively.

The optical beam system for the detection of the cantilever deflection is used most frequently [7, 8, 9, 10].

- **Optical interferometer:** This system uses the rear side of the cantilever as the second mirror of the interferometer (see Fig. 2.5 b). Advantages of this technique are a small space requirement and an easy calibration to the wavelength of the used laser light [11, 12].

- **Capacitor system:** The deflection of the cantilever can be detected by difference in capacity. The capacitor consists of the rear side of the cantilever and a small plate above the cantilever (see Fig. 2.5 c). This technique is capable of fast dynamic measurements [2].

- **Cantilever with a piezoceramic layer:** These cantilevers are self-sensing. A piezoceramics layer is deposited on the rear side of the cantilever. The principle of detection is based on changing electric properties of piezoceramics under mechanical stress. Advantages of this technique are a minimal space requirement and capability of fast measurements. On the other hand, the signal-noise ratio is lower than in measurements with optical beam systems. Nevertheless, the first dynamic measurement at atomic resolution was achieved by this detection technique [13].

  There are two basic types of cantilevers with piezoceramic layer. The first type is the piezoresistive layer changing the resistivity under mechanical stress. It consists of four independent piezorezistive layers and enables to detect the lateral forces (see Fig. 2.5 d) [2, 14, 15]. The second type is the piezoelectric layer generating the voltage under mechanical stress (see Fig. 2.5 e) [2].

- **Scanning Tunneling Microscopy (STM) detection:** Binning et al. proposed the STM technique to detect the deflection of the cantilever [1]. This technique is very sensitive but this measurement of the cantilever deflection is strongly influence by the interaction between the STM tip and the cantilever (see Fig. 2.5 f).

2.5. Cantilever

The cantilever is used as a probe for detection of the force interaction with the sample. Its bending determines the magnitude of the acting force.

Two basic shapes of cantilevers are used:

a) triangular (see Fig. 2.6 a) and

b) rectangular (see Fig. 2.6 b).

2.5.1. Mechanical and geometrical parameters of the cantilever

The spring constant and the tip radius are the most important parameters of the cantilever.

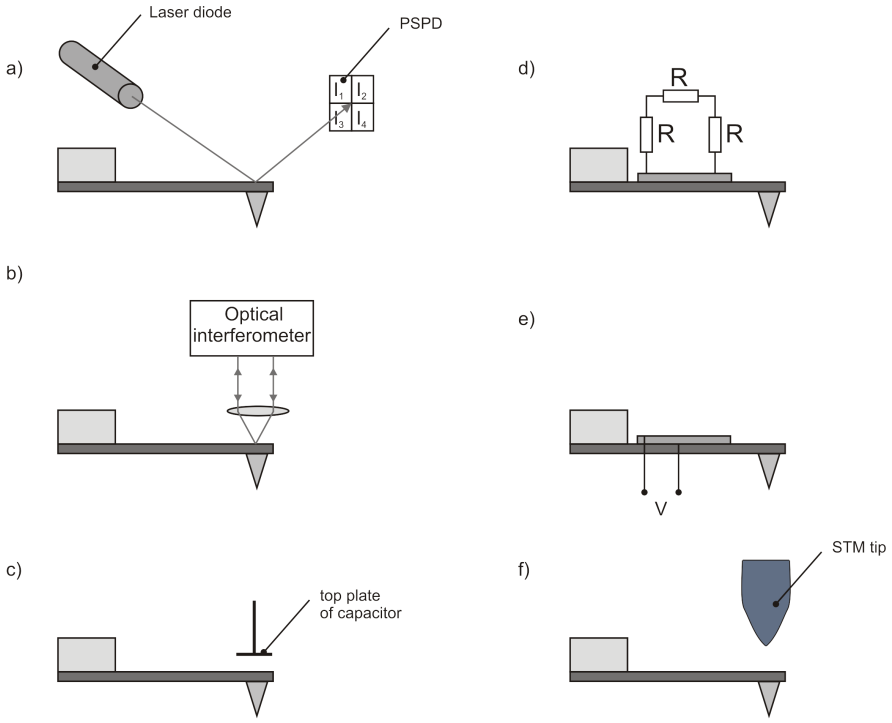

Fig. 2.5: Detection systems of the cantilever deflection: a) optical beam system, b) optical interferometer, c) capacitor system, d) piezorezistive cantilever, e) piezoelectric cantilever, f) STM detection.

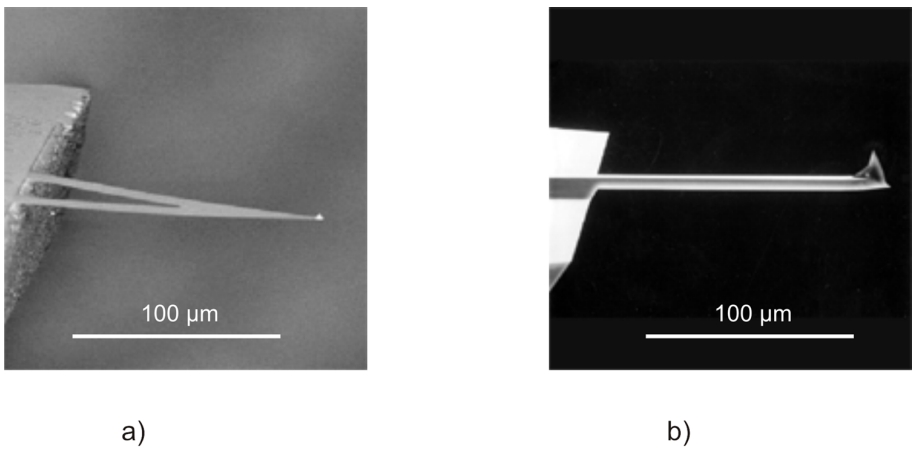

Fig. 2.6: Two basic shapes of cantilevers: a) triangular [16] and b) rectangular [17] (SEM pictures).

The tip radius should be small as much as possible to provide the best resolution of the measurement. The value of the tip radius depends significantly on the way of the tip preparation and typically is in the order of 10^1 nm [16, 17]. Special types of the tips can be prepared, for example the tip with diamond like carbon nanotubes layer deposited on the silicon tip having the tip radius in the order of 10^0 nm [18].

The spring constant can be adjust to a preferable value by changing the proportion parameter as the length and width. The spring constant can be calculated for the normal bending as

$$k_{\mathrm{N_R}} = \frac{Ewt^3}{4l^3} \tag{2.16}$$

for the rectangular cantilever [2], where E is the Young modulus, w is the width, t is the thickness, l is the length (see Fig. 2.7 a), and as

$$k_{\mathrm{N_T}} = \frac{Ewt^3}{2l^2}\cos\theta\left[1 + \frac{4w^3}{b^3}(3\cos\theta - 2)\right]^{-1} \tag{2.17}$$

for the triangular cantilever [19], where E is Young modulus, w is the width of the cantilever arm, t is the thickness, l is the length, θ is the angle between the cantilever arms and b is the distance between the arms at the cantilever stage (see Fig. 2.7 b).

The torsial spring constant can be calculated for the rectangular cantilever as [2]

$$k_{\mathrm{T_R}} = \frac{Gwt^3}{3h^2l}, \tag{2.18}$$

where G is the shear modulus of the material and h is the height of the tip (*see* Fg. 2.7 a). Determination of the torsial spring constant has no sense for the triangular cantilever because this constant is very high and the deflection caused by the lateral forces is minimal [2].

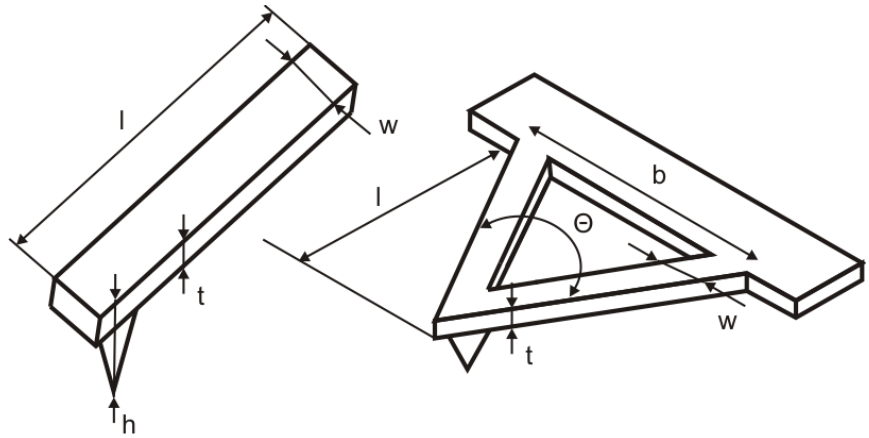

Fig. 2.7: Schematic drawing of two types of the cantilevers: a) rectangular, b) triangular.

Generally, the rectangular cantilevers are softer than the triangular ones. The triangular cantilevers are more resistant towards lateral forces and they are widely used for topographical measurement [2].

The previous calculation of the cantilever spring constant can give a good estimation. However, it is necessary to find the real value of the cantilever spring constant. There are many techniques how to measure this quantity. For example, one of them is described in [20]. It is based on measurement of viscous damping of the cantilever vibrations in the air.

Mechanical and geometrical parameters of the cantilever are limited by few special requirements. For instance, the resonant frequency of the cantilever should be above the resonant frequency of buildings (1 - 100 Hz) and the sound waves (20 - 20000 Hz).

If an atomic resolution is needed then the spring constant of the cantilever should have the same value as the atomic spring constant. Its simple estimation can be done as [2]

$$k_{\text{atom}} = m\omega^2, \tag{2.19}$$

where m is the atom mass and ω is the phonon frequency (typically in the order of 10^{13} Hz). The atomic spring constant is 5 N/m for silicon ($m = 5 \cdot 10^{-26}$ kg).

The other restrictions to the cantilever design is the presence of thermal vibrations. The simple estimation of the thermal vibration can be done as [2]

$$k_{\text{therm}} = \frac{k_{\text{B}}T}{\langle \Delta z^2 \rangle}, \tag{2.20}$$

where k_{B} is the Boltzmann constant and T is the temperature. The spring constant of the cantilever should be higher than k_{therm}, which according to equation 2.20 equals to 0.4 N/m for T=300 K.

Nowadays the typical parameters of the cantilevers are shown in Tab. 2.1 [21, 22, 23].

Parameter	Value
length	50-500 μm
width	20-50 μm
thickness	2-5 μm
spring constant	1-100 N/m
resonant frequency	10-500 kHz
tip radius	1-50 nm

Tab. 2.1: Typical parameters of cantilevers.

2.5.2. Fabrication of the cantilever

Cantilevers are fabricated by the polylitography. The cantilevers are made of Si⟨110⟩. The fabrication process consists of twelve basic steps [3, 24] as follows:

1) The layer of a photoresist is spinned on the Si surface and exposed through a mask (see Fig. 2.8 a).

2) Etching process removes an unexposed part of photoresistive layer protected by the photomask in previous the step (see Fig. 2.8 b).

3) The implantation of boron ions is done. Ions penetrate 10 μm deep into Si substrate (see Fig. 2.8 c). Boron ions are used to the protect bottom layers from etching processes.

4) Solvent is applied to remove the rest of photoresist (see Fig. 2.8 d).

5) Substrate is annealed to built boron built into the Si lattice (see Fig. 2.8 e).

6) Photoresist is deposited on the rear side of the Si substrate and exposed to light through a mask (see Fig. 2.8 f).

7) Solvent is used to remove an exposed part of the photoresist and the layer of Si_3N_4 is deposited (see Fig. 2.8 g). Si_3N_4 is used to protect the bottom layer in the etching process in the step i.

8) Solvent removes the rest of exposed part of the photoresist (see the step f in Fig. 2.8 h).

9) The next etching process removes Si up to the layer implanted with boron ion (see Fig. 2.8 i).

10) The Si plate is turned over (see Fig. 2.8 j).

11) Photolitography process is done through a mask with a motive of small holes to fabricate a tip of the cantilever (see Fig. 2.8 k and l).

12) A special etchant is applied to etch the boron-doped Si layer (see Fig. 2.8 m). The etching solution removes the Si layer from both sides and in this way the tip of the cantilever is created. The principle of the tip fabrication is shown in Fig. 2.8 n.

The next fabrication process of cantilevers depends on the purpose of their application. The special layer of gold or aluminium can be deposited on the rear side of the cantilever to increase the reflection of the laser beam used in the optical beam detection system. Various conductive or magnetic layers can be deposit on the tip as well [2, 3, 22, 21, 23].

2.6. Modes of Scanning Force Microscopy

Nowadays there are available various modes of Scanning Force Microscopy. The names of the modes reflect characteristic properties of these measurement modes. Generally, these modes can be divided into three basic groups: contact mode, non-contact mode and semi-contact mode with depending whether the tip is or is not in contact with the sample. Each mode uses a specific range of interaction forces and distances between the tip and the sample (see Fig. 2.9) [2, 3].

Following description of modes is done for Atomic Force Microscopy. Other techniques from Scanning Force Microscopy use the same general principle but the exact setup is modified depending on the force interaction.

2.6.1. Contact mode

This mode is based on the measurement static deflection of the cantilever. The force acting on the tip can be attractive or repulsive depending on the type of the force and the distance between the sample and the tip. The resultant force can be determined directly from the deflection of the cantilever as [2, 3]

$$F = k_C \Delta r, \tag{2.21}$$

where k_C is the spring constant, and Δr is the deflection from the equilibrium state.

The scanning process in the contact mode can be divided in two scanning techniques: scanning at the constant height above the sample and scanning with constant cantilever deflection (constant force measurement).

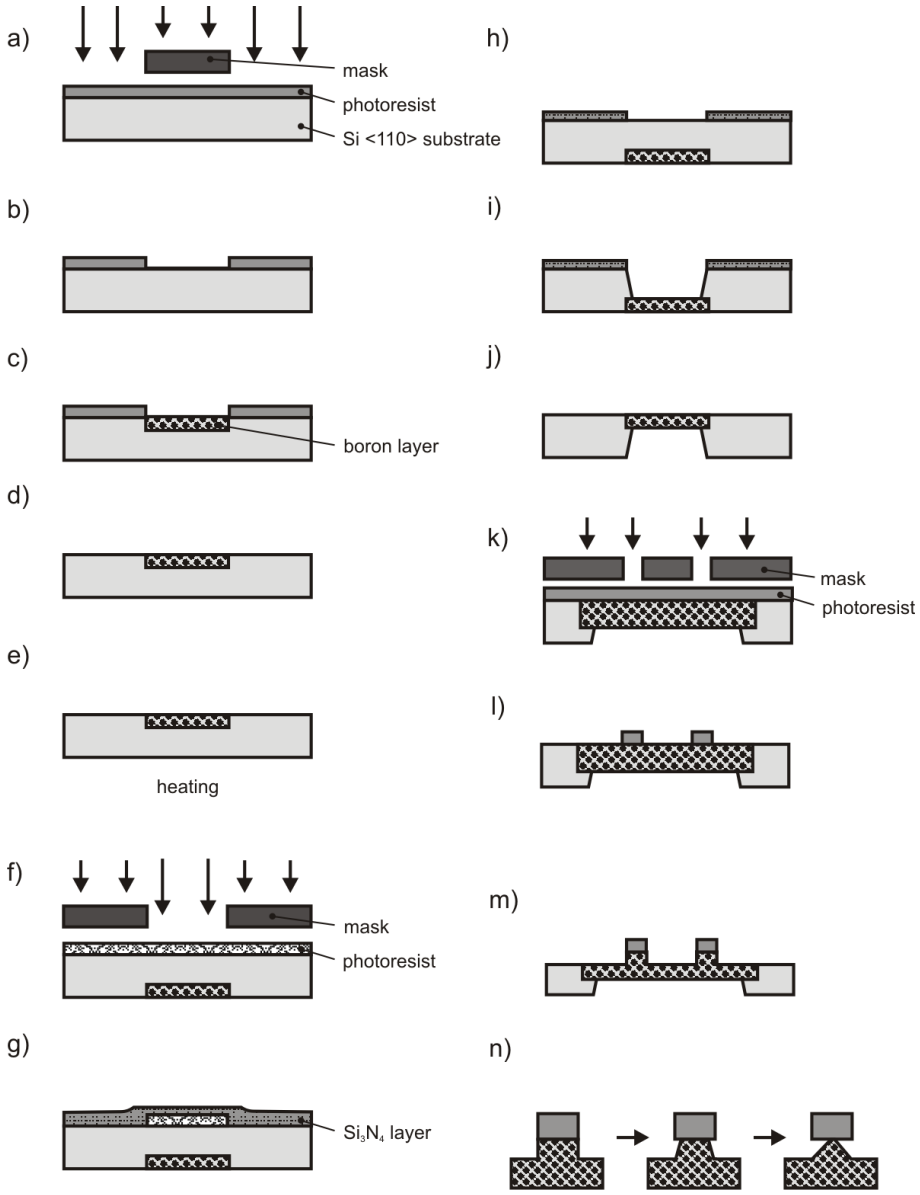

Fig. 2.8: Schematic steps of the cantilever fabrication: a) photolitography, b) etching of photoresist, c) boron ion implementation, d) removing the photoresist, e) annealing, f) photolitography, g) deposition of Si_3N_4 layer, h) etching of photoresist, i) etching of Si plate j) turn the Si plate to top side, k) photolitography, l) etching the photoresist, m) etching the layer with boron ions, n) principle of tip creation.

- **Scanning at the constant height:** The tip scans at a constant distance above the sample and its deflection changes with the interaction force (see Fig. 2.10). The result of this measurement is a map of forces above the sample. This technique is used for the samples with small surface corrugations in the order of 10^{-1} nm - 10^{0} nm.

- **Scanning with a constant cantilever deflection (Constant force measure):** This technique is based on keeping the constant deflection of the cantilever. It is done by a feedback control unit which drives the piezoscanner. If the cantilever deflection is changed, the feedback control unit adjusts the distance between the tip and the sample by the piezoscanner (see Fig. 2.11).

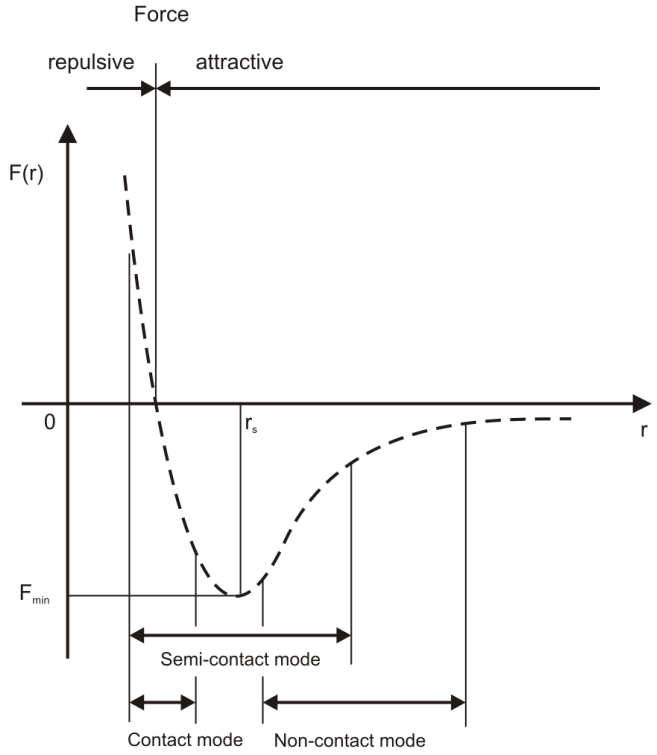

Fig. 2.9: Modes of Scanning Force Microscopy and range of interaction forces and distances between the sample and the tip.

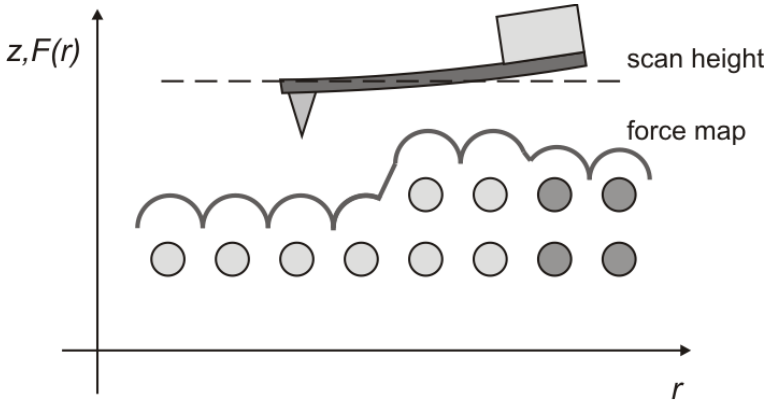

Fig. 2.10: Contact mode - scanning in constant height.

Soft cantilevers are used in the contact mode to increase the sensitivity and to avoid damaging of the tip or the sample. Nevertheless it is important to mention that the tip or the sample might be damaged after contact measurement.

The atomic resolution can be reached only when force affecting on the tip (and thus the force from the tip on the surface) is around zero.

2.6.2. Non-contact mode

This mode uses a cantilever oscillating technique to detect the force affecting the cantilever. The cantilever oscillates above the sample at certain distance (see Fig. 2.12).

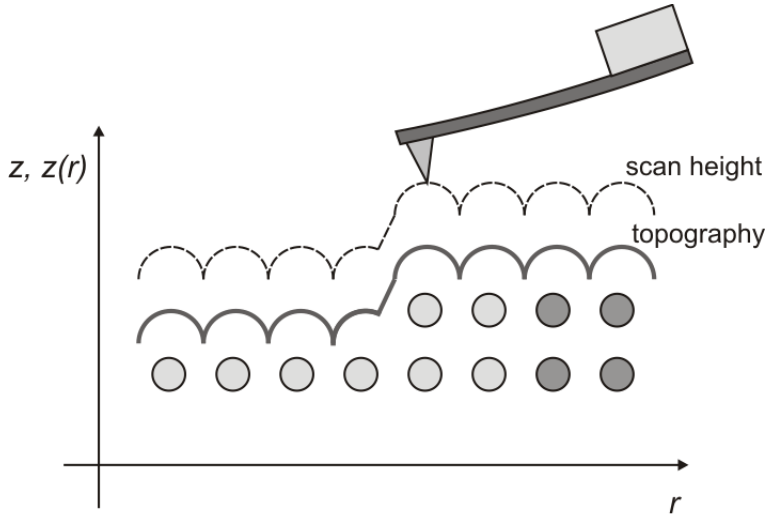

Fig. 2.11: Contact mode - scanning with a constant deflection.

The force affecting the cantilever is determined from differences of the cantilever dynamic parameters. These parameters such as amplitude, frequency shift or phase shift can be used for feedback control.

The cantilever with a high resonant frequency above 50 kHz is usually used for the non-contact mode. The advantage of non-contact mode is its capability to measure soft samples as organic or biologic materials without damaging them. The distance between the tip and the sample is in the order of 10^1 nm.

The principle of the non-contact mode can be demonstrated by the oscillating cantilever with its mass concentrated only in the tip, amplitude of oscillations in the order of nanometers and driving force $F\cos(\omega_0 t)$. The cantilever is mounted on a holder being driven by the driving force (see Fig. 2.12).

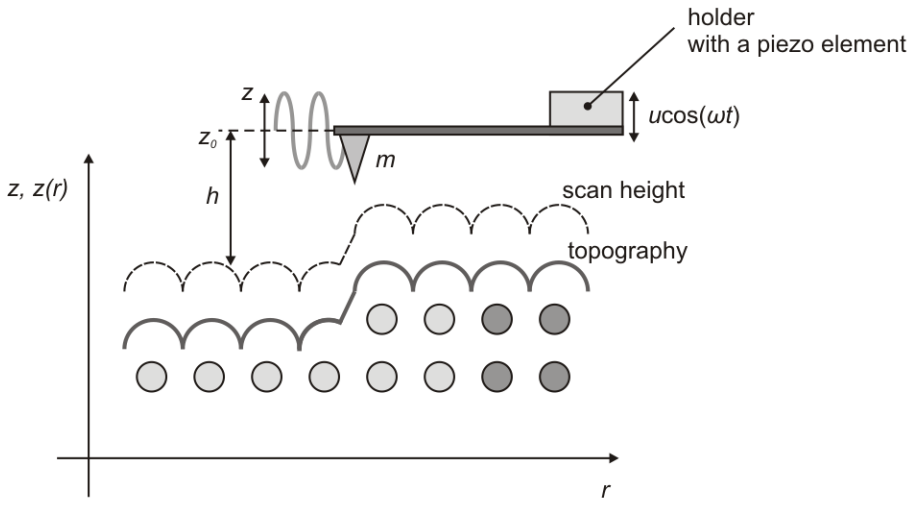

Fig. 2.12: Non-contact mode - schematic setup.

At first, the system without interaction force between the sample and the tip is described to explain free behaviour of cantilever vibrations. The equation of motion of this system can be written as [3]

$$m\ddot{z} = k_{\mathrm{C}}[u\cos(\omega t) - z] - \gamma\dot{z} + F_0, \tag{2.22}$$

where m is the mass of the tip, k_C is the spring constant, u is the amplitude of the driving piezoelement, ω is the frequency of the driving force, t is the time, z is the deflection of the tip from the equilibrium position, γ is the constant of viscous damping and F_0 is the constant force affecting the cantilever for example gravity (see Fig. 2.12). It is know that the constant force causes a shift of the equilibrium position of the system but does not change the dynamic properties of the cantilever [3]. Let us define a new variable

$$a = z + \frac{F_0}{k_C}. \tag{2.23}$$

Now we rewrite the equation 2.22 using equation 2.23 as

$$m\ddot{a} + \gamma\dot{a} + ka = ku\cos(\omega t). \tag{2.24}$$

We adjust the equation 2.24 for the next computation as

$$\ddot{a} + \frac{\omega_0}{Q}\dot{a} + \omega_0^2 a = \omega_0^2 u\cos(\omega t), \tag{2.25}$$

where ω_0 is defined as

$$\omega_0 = \sqrt{\frac{k}{m}} \tag{2.26}$$

and Q is so-called the quality factor of the cantilever defined as

$$Q = \frac{m\omega_0}{\gamma}. \tag{2.27}$$

The equation 2.25 is the nonhomogeneous differential equation of the second order and finding the solution in the range of real numbers is not straight forward. Hence, we rewrite the equation 2.25 onto complex plane as

$$\ddot{A} + \frac{\omega_0}{Q}\dot{A} + \omega_0^2 A = \omega_0^2 u e^{-\mathrm{i}\omega t}, \tag{2.28}$$

where A is complex coordinates. The solution of this equation is not easy again. So we consider steady state of the system. It is vindicable assumption because the transient state of motion is very fast. So the we estimate solution of the equation 2.28 as

$$A = Be^{-\mathrm{i}\omega t}. \tag{2.29}$$

We substitute the relation 2.29 to the equation 2.28. The solution of this equation gives us the complex amplitude

$$B = \frac{u\omega_0^2}{\omega_0^2 - \omega^2 - \mathrm{i}\frac{\omega_0\omega}{Q}}. \tag{2.30}$$

The real part of the complex amplitude B is equal to the cantilever amplitude b [3]

$$b = \frac{u\omega_0^2}{(\omega_0^2 - \omega^2)^2 + \frac{\omega_0^2\omega^2}{Q^2}}. \tag{2.31}$$

The phase shift $\zeta(\omega)$ between the oscillation of the cantilever and the driving vibrations can be determined as

$$\zeta(\omega) = \arctan\left(\frac{Im\{B\}}{Re\{B\}}\right) = \arctan\left[\frac{\omega_0\omega}{Q(\omega_0^2 - \omega^2)^2}\right]. \tag{2.32}$$

The resonant frequency of the system ω_{res} can be calculated as

$$\left.\frac{db}{d\omega}\right|_{\omega=\omega_{\mathrm{res}}} = 0, \tag{2.33}$$

$$\omega_{\mathrm{res}} = \omega_0\sqrt{1-\frac{1}{2Q^2}}. \tag{2.34}$$

The frequency shift $\Delta\omega$ can be calculated from equation 2.34 as

$$\Delta\omega = \omega_0 - \omega_{\mathrm{res}} = \omega_0\left(1-\sqrt{1-\frac{1}{2Q^2}}\right). \tag{2.35}$$

It is shown in the previous text how the cantilever behaves without a tip-sample force. Now we add to the equation 2.22 the force originated between the sample and the tip, for example the van der Waals force. We consider the gradient of this force is constant in the region of cantilever oscillations. Thus, we can write for additional force

$$F_{\mathrm{A}} = F_{\mathrm{A},0} + \left.\frac{\partial F_{\mathrm{A}}}{\partial z}\right|_{z=z_0} z = F_{\mathrm{A},0} + F'z, \tag{2.36}$$

where $F_{\mathrm{A},0}$ is the constant part of force F_{A} at the distance z_0 and $\left.\frac{\partial F_{\mathrm{A}}}{\partial z}\right|_{z=z_0}$ or F' is the force gradient at the distance z_0. We can use this assumption because oscillation amplitude is in the order of 10^0 nm which is relatively small compared to the tip sample distance (10^1 nm). We add relation 2.36 to equation 2.22 and we obtain equation of motion for the cantilever oscillations effected by the additional force

$$m\ddot{z} = k_{\mathrm{C}}[u\cos(\omega t) - z] - \gamma\dot{z} + F_0 + F_{\mathrm{A},0} + F'z. \tag{2.37}$$

Let us introduce a new variable from the same reason as in equation 2.23 so

$$c = z + \frac{(F_0 + F_{\mathrm{A},0})}{k_{\mathrm{C}}} \tag{2.38}$$

and we can rewrite the equation 2.37 as

$$\ddot{c} + \frac{\omega_0}{Q}\dot{c} + \left(\omega_0^2 - \frac{F'_{\mathrm{A}}}{m}\right)c = \omega_0^2 u\cos(\omega t). \tag{2.39}$$

The same steps and assumptions may be used as in previous calculation. The real part of the complex amplitude of the cantilever effected the additional force F_{A} is

$$b_{\mathrm{F}} = \frac{u\omega_0^2}{\left(\omega_0^2 - \omega^2 - \frac{F'_{\mathrm{A}}}{m}\right)^2 + \frac{\omega_0^2\omega^2}{Q^2}} \tag{2.40}$$

and the phase shift $\zeta_{\mathrm{F}}(\omega)$ is

$$\zeta_{\mathrm{F}}(\omega) = \arctan\left[\frac{\omega_0\omega}{Q\left(\omega_0^2 - \omega^2 - \frac{F'_{\mathrm{A}}}{m}\right)^2}\right]. \tag{2.41}$$

The resonant frequency $\omega_{\mathrm{res,F}}$ of the system $\omega_{\mathrm{res,F}}$ is equal to

$$\omega_{\mathrm{res,F}} = \omega_0 \sqrt{1 - \frac{1}{2Q^2} - \frac{F'_{\mathrm{A}}}{m}}. \tag{2.42}$$

The frequency shift $\Delta\omega_{\mathrm{F}}$ can be computed as

$$\Delta\omega_{\mathrm{F}} = \omega_{\mathrm{res}} - \omega_{\mathrm{res,F}} = \omega_{\mathrm{res}} \left(1 - \sqrt{1 - \frac{F'}{m\omega_{\mathrm{res}}}} \right). \tag{2.43}$$

The schematic dependance of cantilever properties on affecting force is shown in Fig. 2.13.

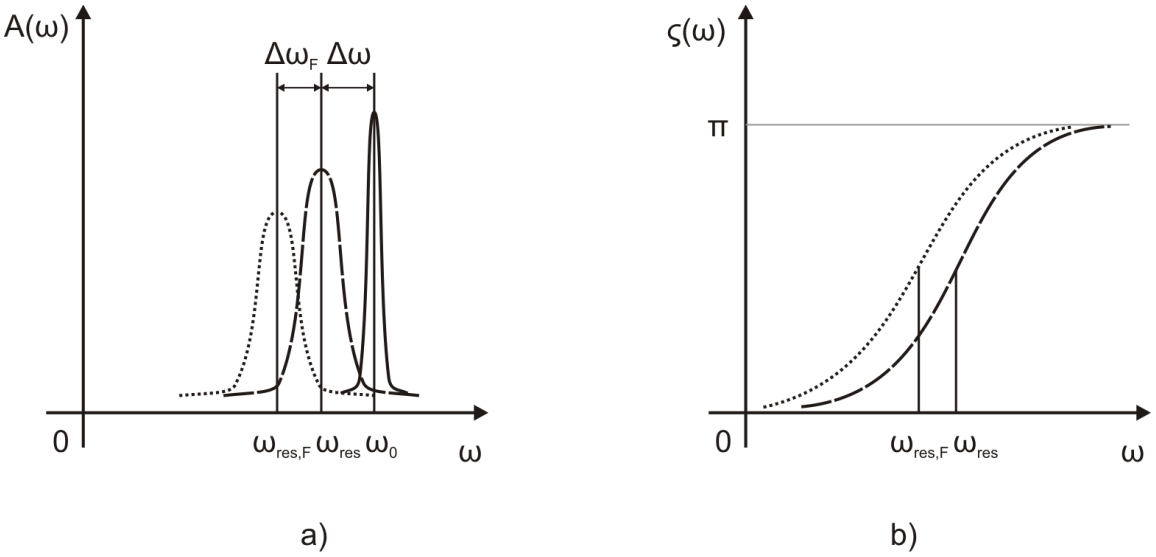

Fig. 2.13: Non-contact mode - the influence of an additional force on cantilever dynamic properties: a) resonant frequency, b) phase; (solid line - cantilever without a driving force, dashed line - cantilever with a driving force, dotted line - cantilever effected by the force between the sample and the tip).

2.6.3. Semi-contact mode

The semi-contact mode is based on the technique of the vibrating cantilever, which becomes into contact with the sample in lower part of its motion (see Fig. 2.14) [3]. This mode is known as tapping mode [2].

The cantilever is exposed to repulsive and attractive forces during its oscillations (see Fig. 2.14). Direct contact of the cantilever with the sample causes bigger changes in dynamic characteristics of the cantilever. It is big advantage of this mode so the feedback loop cannot be so stable and precise and its design is simpler than for non-contact mode. Next advantage is non-sensitivity to lateral forces [3]. Description of motion of the cantilever in this mode is more complex than in the contact mode because the force changes from attractive to repulsive and back during one oscillation cycle. The cantilever oscillates with the amplitude A above the sample at the equilibrium distance h (see

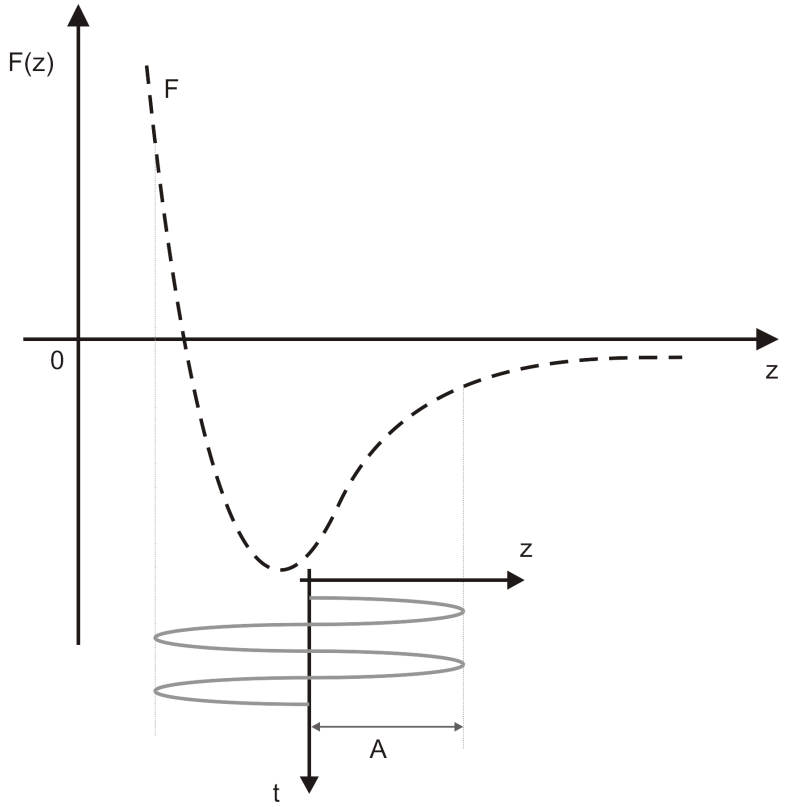

Fig. 2.14: Semi-contact mode - oscillations of the tip and the force affecting the cantilever.

Fig. 2.15). The amplitude A has to be bigger than the distance h so that the cantilever can be tapping the surface of the sample. The cantilever motion can be describe as [3]

$$m\ddot{z} + \frac{\omega_0}{Q} + \omega^2(z - z_0 - ucos(\omega t)) = \frac{\omega^2}{k}F(z), \tag{2.44}$$

where $F(z)$ is the force acting on the cantilever (see Fig 2.14). The solution of equation 2.44 is more complicated than in non-contact mode because equation 2.44 is non-linear. We will use a different way how to estimate the changes of the cantilever dynamic characteristics. The energy coming to the system, E_{C}, has to be equal to the energy which is dissipated, E_{D}, [3] in system at equilibrium

$$E_{\mathrm{C}} = E_{\mathrm{D}}. \tag{2.45}$$

The energy E_{C} coming to the system from the piezoelement can be written as [3]

$$E_{\mathrm{C}} = \int_t^{t+\frac{2\pi}{\omega}} ku\cos(\omega t)\frac{\mathrm{dz}}{\mathrm{dt}}\mathrm{dt}, \tag{2.46}$$

where ω is the frequency of piezoelement oscillations, k is the cantilever spring constant, $u\cos(\omega t)$ is the deflection of the cantilever and $\frac{\mathrm{dz}}{\mathrm{dt}}$ is the speed of the cantilever. The energy dissipated by the system is equal to the sum of energies dissipated because of the damping caused by the medium between the sample and the cantilever $E_{\mathrm{D,dam}}$ and due to the contact with the surface of the sample $E_{\mathrm{D,sam}}$

$$E_{\mathrm{D}} = E_{\mathrm{D,dam}} + E_{\mathrm{D,sam}}. \tag{2.47}$$

These energies can be expressed as

$$E_{\mathrm{D,dam}} = \int_t^{t+\frac{2\pi}{\omega}} \frac{m\omega_0}{Q}\left(\frac{\mathrm{dz}}{\mathrm{dt}}\right)^2 \mathrm{dt} \tag{2.48}$$

and

$$E_{\mathrm{D,sam}} = \int_t^{t+\frac{2\pi}{\omega}} F(z)\frac{\mathrm{dz}}{\mathrm{dt}}\mathrm{dt}. \tag{2.49}$$

Assuming oscillations as $z = A\cos(\omega t + \zeta)$ we can get the phase shift as [3]

$$\zeta = \arcsin\left(\frac{\omega A}{u\omega} + \frac{QE_{\mathrm{D,sam}}}{\pi kuA}\right). \tag{2.50}$$

It is clear from equation 2.50 that the phase shift is determined by the energy dissipated by the sample during the contact with the cantilever.

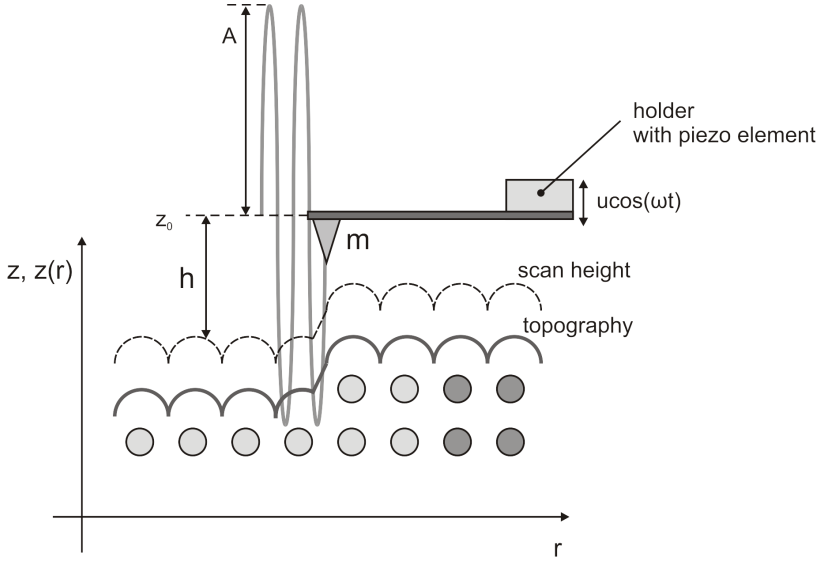

Fig. 2.15: Semi-contact mode - a schematic setup.

2.7. Kelvin Probe Atomic Force Microscopy

Kelvin probe atomic force microscopy (KP - AFM, in other literature also: Scanning Kelvin probe microscopy [68] or Surface potential detection [47]) is a special technique of Electrostatic Force Microscopy [3, 48]. KP - AFM is used to measure the work function of metal [71, 72], to study electron transport processes in quantum structures [73] or in thin layers [31, 74], testing dipole-dipole interactions [75], etc.

KP - AFM measures the contact potential difference (CPD) on a nanometer scale [44-46, 67, 68].

The CPD depends on many parameters: the difference between work functions of the cantilever and the sample [69-72], concentrations of dopants in semiconductors, changes in sample temperature, sample impurities [69, 70], etc. The measurement of the CPD can be used to obtain previous parameters [44].

2.7.1. The principle of KP - AFM

The principle part of KP - AFM is the planar sample and the rectangular cantilever with the conic tip at the end. It is obvious 3D problem to be solved. But the basic principle of the KP - AFM can be explained by a parallel plane capacitor.

The principle of the CPD measurement is in Fig. 2.16. When the cantilever scans over the sample the difference between the work functions of the cantilever and the sample causes additional electric force affecting the cantilever. When U_{dc}=CPD is applied between the sample and the cantilever, the force becomes zero.

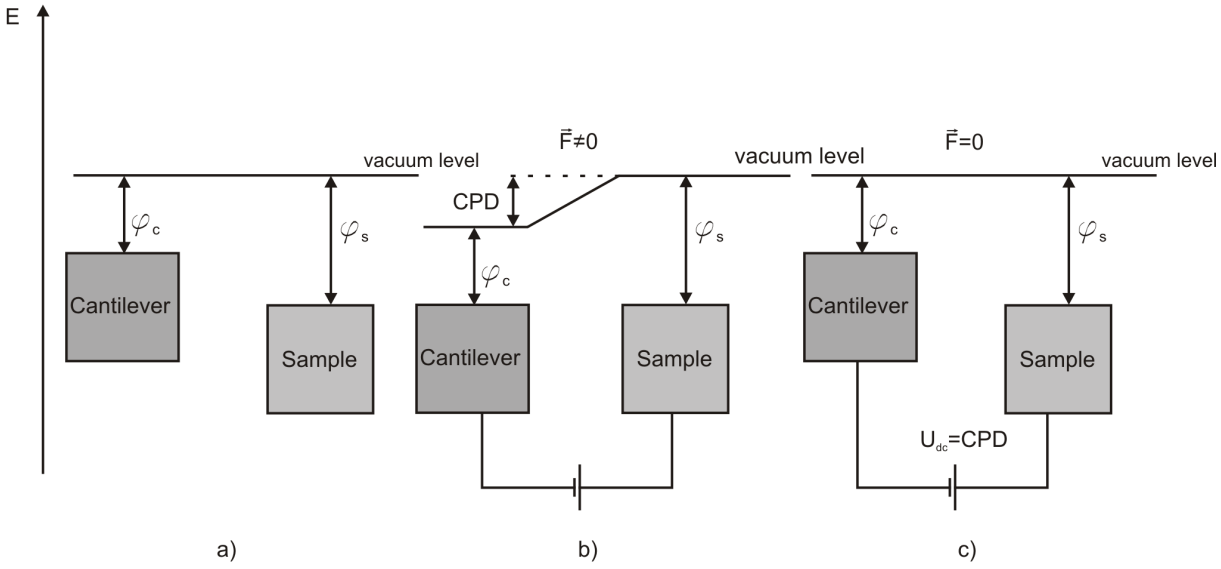

Fig. 2.16: KP - AFM measurement of the CPD - energy level scheme: a) non-conductive connection between the sample and the cantilever, b) conductive connection between the sample and the cantilever, c) conductive connection between the sample and the cantilever with applied voltage U_{dc} =CPD between them.

The bias voltage U_{app} is applied between the cantilever and the holder of the sample. It consists of an alternating voltage $U_{\mathrm{ac}}\sin(\omega t)$ and direct voltage U_{dc} (see Fig. 2.17). So we can write:

$$U_{\mathrm{app}} = U_{\mathrm{dc}} + U_{\mathrm{ac}}\sin(\omega t). \tag{2.51}$$

The total voltage affecting the cantilever is the sum of all voltages applied between the

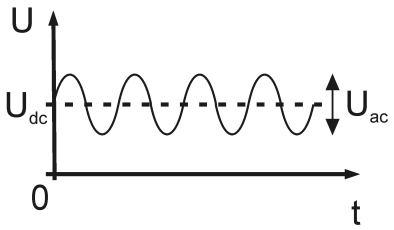

Fig. 2.17: The bias voltage applied on the cantilever

cantilever and the sample. So the total voltage is:

$$U = U_{\mathrm{app}} + U_{\mathrm{as}} + U_{\mathrm{s}}, \tag{2.52}$$

where U_{as} is an additional voltage on the sample and U_{s} is difference between the work functions of the cantilever φ_{c} and the sample φ_{s}, defined as:

$$U_{\mathrm{s}} = \frac{1}{e}\big(\varphi_{\mathrm{c}} - \varphi_{\mathrm{s}}\big). \tag{2.53}$$

A specific additional bias U_{as} is applied between the cantilever and the sample so that the electric field in between vanishes. This determined by measuring the force caused by the applied bias [44].

The sum of all direct bias voltages between the sample and the cantilever U_{d} is:

$$U_{\mathrm{d}} = U_{\mathrm{dc}} + U_{\mathrm{as}} + U_{\mathrm{s}}. \tag{2.54}$$

Now we determine the relation between the force affecting the cantilever and the total voltage between the cantilever and the sample. The approximation based on a plane capacitor will be used. The electrostatics energy of this capacitor is:

$$E = \frac{1}{2}CU^2, \tag{2.55}$$

where C is the capacity of the capacitor consisted of the sample and the cantilever. The force can be determined as:

$$\vec{F} = -\nabla E = -\nabla\left(\frac{1}{2}CU^2\right), \tag{2.56}$$

since only z position of the cantilever changes due to the interaction force equation 2.56 can be rewritten as:

$$F = -\frac{\partial}{\partial z}\left(\frac{1}{2}CU^2\right). \tag{2.57}$$

The dependance of the electrostatic force on the capacitor voltage is shown in Fig. 2.18. As the total voltage U is independent on the distance between the cantilever and the

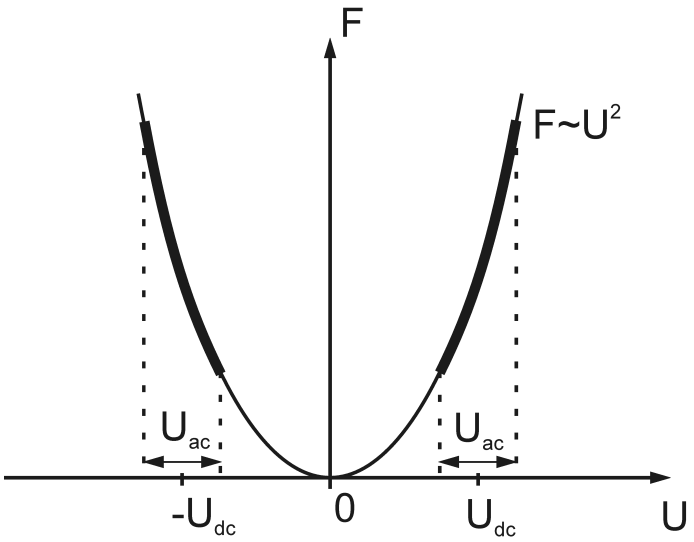

Fig. 2.18: Dependance of the electrostatic force on the bias.

sample, we can write 2.57 as:

$$F = -\frac{1}{2}\frac{\partial C}{\partial z}U^2. \tag{2.58}$$

Now we substitute realation 2.52 in equation 2.58:

$$F = -\frac{1}{2}\frac{\partial C}{\partial z}\Big[U_{\mathrm{d}}^2 + \frac{1}{2}U_{\mathrm{ac}}^2 + 2U_{\mathrm{d}}U_{\mathrm{ac}}\sin(\omega t) - \frac{1}{2}U_{\mathrm{ac}}^2\cos(2\omega t)\Big], \tag{2.59}$$

The equation 2.59 can be divided into three parts as:

$$F = -\frac{1}{2}\frac{\partial C}{\partial z}\Big[\underbrace{U_{\mathrm{d}}^2 + \frac{1}{2}U_{\mathrm{ac}}^2}_{constant\ \mathrm{term}} + \underbrace{2U_{\mathrm{d}}U_{\mathrm{ac}}\sin(\omega t)}_{\omega\ \mathrm{term}} - \underbrace{\frac{1}{2}U_{\mathrm{ac}}^2\cos(2\omega t)}_{2\omega\ \mathrm{term}}\Big]. \tag{2.60}$$

The oscillating electric force initiated at frequency ω acts as a sinusoidal driving force. This force influences the motion of the cantilever in a very narrow band near the frequency ω. So the constant and 2ω term can be omitted in equation 2.60. Hence ,the equation for the force affecting the cantilever can be written as:

$$F = -\frac{\partial C}{\partial z}[U_{\mathrm{d}}U_{\mathrm{ac}}\sin(\omega t)]. \tag{2.61}$$

The feed back loop is working to keep the total force gradient equal to zero. It means the total force F has to be constant ($F = const$):

$$F = -\frac{\partial C}{\partial z}\,[U_{\mathrm{d}}U_{\mathrm{ac}}\sin(\omega t)] = const. \tag{2.62}$$

To meet this condition the total voltage U_{d} should be kept zero. The U_{d} is defined in equation 2.54, so:

$$U_{\mathrm{dc}} + U_{\mathrm{as}} + U_{\mathrm{s}} = 0. \tag{2.63}$$

The feedback loop adjusts U_{dc} to keep $U_{\mathrm{d}} = 0$. The difference in U_{dc} in each point determines the CPD (see Fig. 2.16).

2.7.2. The setup

The setup of KP - AFM depends on the way of data acquisition. There are two ways how to obtain data:

a) two - pass system (see Fig. 2.20) [47]

b) simultaneous system (see Fig. 2.22) [46]

Two - pass system

The scheme is in Fig. 2.20. The dashed line in the figure indicates the part for topographical imaging, and the solid line indicates the part added for CPD measurements.

This system of the data acquisition is based on two passes of the cantilever over one scan line. It utilizes the amplitude modulation of the feedback loop [47].

- **The first pass**: The topography is obtained and saved. The tapping mode is used for this acquisition (see Fig. 2.19 a and Fig. 2.23b).

- **The second pass**: The cantilever is relocated to the lift scan height h_{TP}. It follows the saved topography (see Fig.2.19 b). The voltage $U_{\mathrm{ac}}\sin(\omega t)$ with the offset U_{dc} is applied between the cantilever and the holder. The frequency ω_{el} is below resonant frequency of the cantilever ω_0 [48]. The servo controller adjusts the bias U_{dc} to minimize the electrostatic force gradient. The difference in U_{dc} determines the CPD (see Fig. 2.23 c).

This measurement acquires the real CPD data, which are minimally influenced by the shape of the topography.

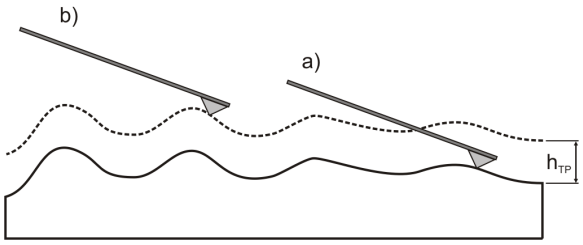

Fig. 2.19: The schematic diagram of the acquisition data for the two - pass system: a) topography measurement, b) CPD measurement.

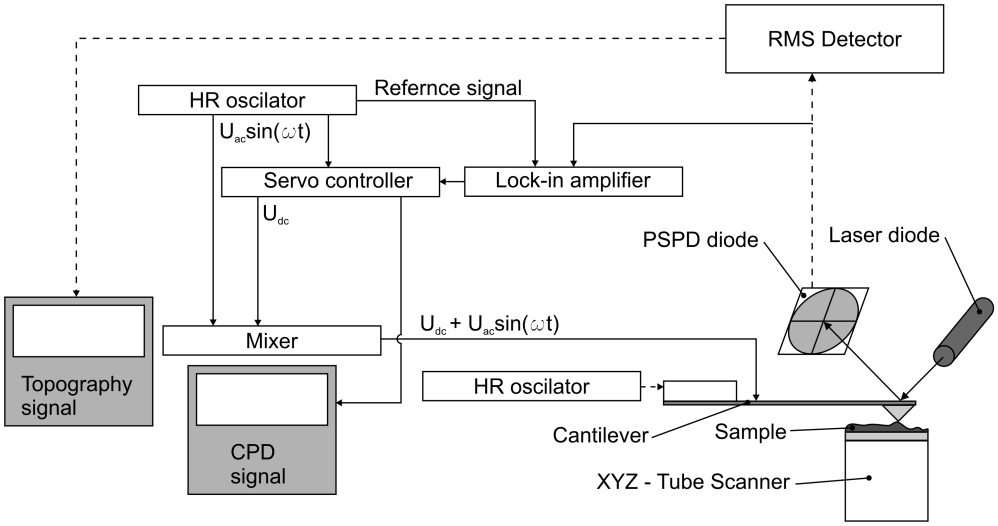

Fig. 2.20: The block diagram of the setup for the two - pass system.

Simultaneous system

The basic schema is in Fig. 2.22. The dashed line in the figure indicates the part for topographical imaging, and the solid line indicates the part added for CPD measurements. This system utilizes the frequency modulation of the feedback loop [46].

The main difference between the two - pass and the simultaneous system is the simultaneous acquisition of the topographical and CPD data. The non-contact mode is used for the topographical data acquisition. The cantilever scans over the sample in height h_{NC} (see Fig. 2.21).

The effective resonant frequency of the cantilever changes with the change of the gradient of atomic force and the electrostatic force (for more see [3, 48]). This system uses two feedback loops:

- **Topographical feedback loop**: Signal from the PSPD goes through a preamplifier, phase shifter, attenuator and a frequency modulation demodulator (FMD). The FMD which is a phase locked loop detects the frequency of the cantilever. An error amplifier determines the phase shift. The feedback manages the z-piezo to keep the constant shift of resonant frequency (see Fig. 2.23 b).

- **CPD back loop**: Voltage $U_{\mathrm{ac}} \sin(\omega_{\mathrm{el}} t)$ (from the error amplifier 2) with the offset U_{dc} (from high resolution oscillator) is applied on the cantilever. The frequency ω_{el} is below resonant frequency of the cantilever ω_0 [48]. The change of the effective resonant frequency ω will appear as a change of the output signal from the FMD and is detected by the lock-in amplifier. The electrostatic force gradient is minimal, when this output is zero. The difference in U_{dc} determines CPD (see Fig. 2.23 c).

This way of data acquisition avoids the thermal noise.

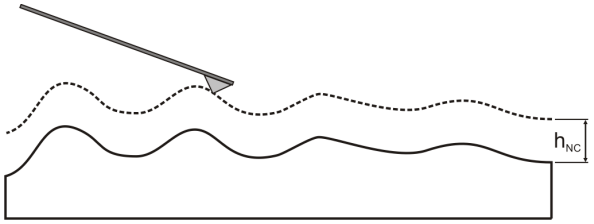

Fig. 2.21: The schematic diagram of the acquisition data for the simultaneous system.

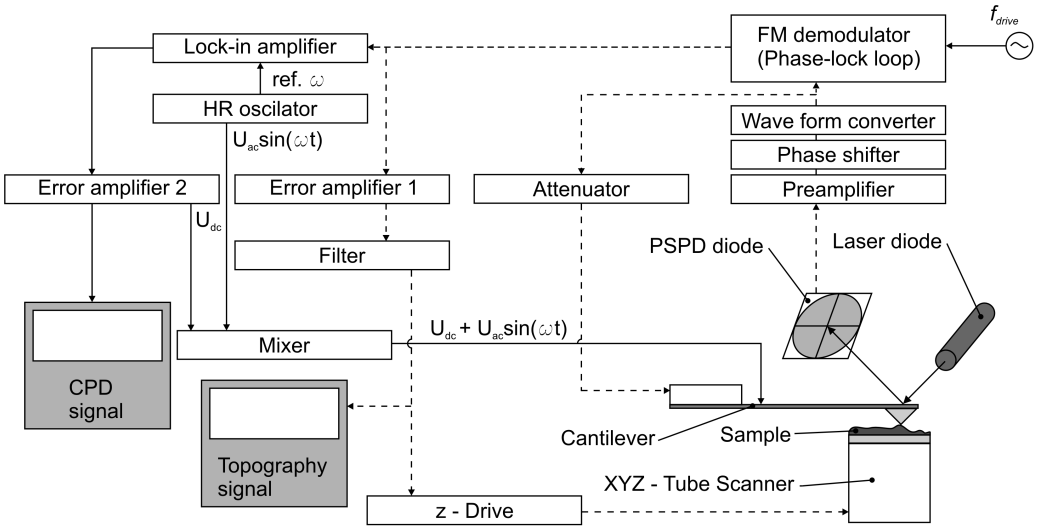

Fig. 2.22: The block diagram of the setup for the simultaneous system.

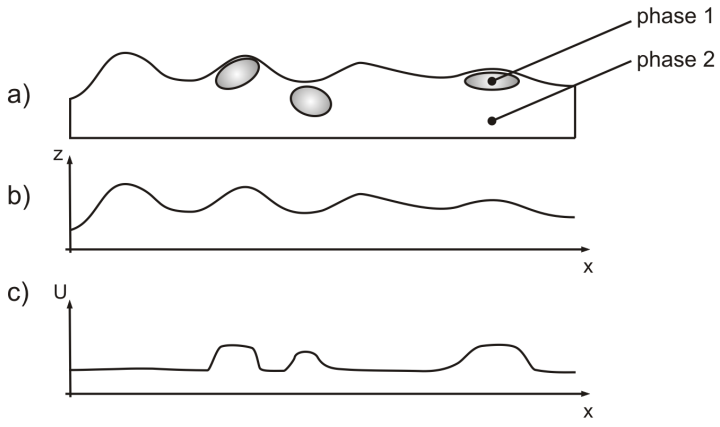

Fig. 2.23: Data obtained by KP - AFM: a) original topography of the sample, b) topography, c) CPD (supposing that the work function of the phase 1 is lower than the second one and lower than the work function of the cantilever).

Chapter 3

Scanning Electron Microscopy

3.1. Introduction

Scanning electron microscope (SEM) is a device using a focused beam of electrons to investigate a specimen at micro- and nanometric scale.

In 1920 it was discovered that electrons in the vacuum behave like a wave with smaller wavelength than light. These properties enable us to reach better resolution. Magnetic or electrostatic field can be used to act on electrons as lenses [50]. Ernst Ruska and Max Knoll designed the first prototype of an electron microscope in 1931. Two years later in 1933 the first image acquired with EM was presented by Max Knoll. Manfred von Ardenne obtained the first image with submicrometer resolution in 1938 [51]. The first commercial product was a transmission electron microscope produced by Siemens in 1938.

The Second world war stopped the work in this field in Europe and caused the research on electron microscopy was shifted in the USA. A big research and development took place especially in Czechoslovakia, Great Britain, France, Germany and Japanese after the war. In 60s' and 70s' of the 20th century many pioneer works were done on the theory of charged particle optics, interaction of electron beam with the specimen, detectors, etc. The first scanning electron microscope was available in 1965 [51].

Nowadays SEM is used for investigation in many various fields such as materials and surface science, food industry, mineralogy, biology, medicine, etc.

Today SEM is able to achieve resolution up to 1 nm [49, 57]. A special type of SEM can work in low vacuum which is used for biological, medicine and non-conductive specimen measurements. The residual atmosphere avoids a charging and a dewattering of the specimen.

There are several producers of SEM in the world: FEI Company^{TM} (USA, Netherlands, Czech Republic), Tescan, s.r.o. (Czech Republic), Carl Zeiss NTS GmbH (Germany), JEOL Ltd. (Japan), Nion Company (USA), FOCUS GmbH (Germany) and Hitachi (Japan).

3.2. Construction

The SEM microscope design can vary but the main building blocks of the construction are the same for the whole SEM setup 3.1 as follows:

- **Electron source:** It generates electrons and focuses them to a primary beam.

- **Electrostatic or magnetostatic lenses:** They are used to demagnify the image of the electron source and image it on the specimen (projective lenses, objective lens).
- **Apertures:** They are located along the optical axis of SEM and change the diameter of the primary beam.
- **Deflection coils:** They are used to scan the primary beam the specimen.
- **Chamber** It is evacuated to a vacuum level depending on the required SEM technique (from 10^2 to 10^{-8} Pa).
- **Detectors:** Interaction of primary beam electrons with the specimen generate signals such as: secondary electrons (SE), back-scattered electrons (BSE), cathodoluminscence (CL), X-rays. Detectors register these signals and convert them to electronic information.
- **Amplifier:** It increases a signal from detectors.
- **Scan generator:** It controls the deflection coils.
- **Acceleration voltage and lens current supplies:** They provide voltages and currents for lenses and the electron source.
- **Personal computer:** It controls the scan generator and processes signals from detectors.

3.3. Electron in static electromagnetic field

Electronin the electric or magnetic field is affected by the Lorentz force

$$\vec{F}_{\mathrm{Lor}} = -e(\vec{E} + \vec{v} \times \vec{B}), \tag{3.1}$$

where e is the elementary charge, $\vec{v}$ is the speed of an electron, $\vec{E}$ is the electric intensity, $\vec{B}$ is the magnetic flux density.

The equation of motion can be expressed as [53]

$$\frac{\mathrm{d}}{\mathrm{d}t}\left(\gamma m\vec{v}\right) = e(\vec{E} + \vec{v} \times \vec{B}), \tag{3.2}$$

where m is the mass of the electron, c is the speed of the light, e is the charge of an electron, γ is defined as

$$\gamma = \frac{1}{\sqrt{1 - \frac{v^2}{c^2}}}. \tag{3.3}$$

It is necessary to use the relativistic modification of the Newton equation of motion due to the small mass of the electron and the high voltage used in SEM in the order of 10-100 keV. The dependance of the electron mass on its speed is in Tab. 3.1.

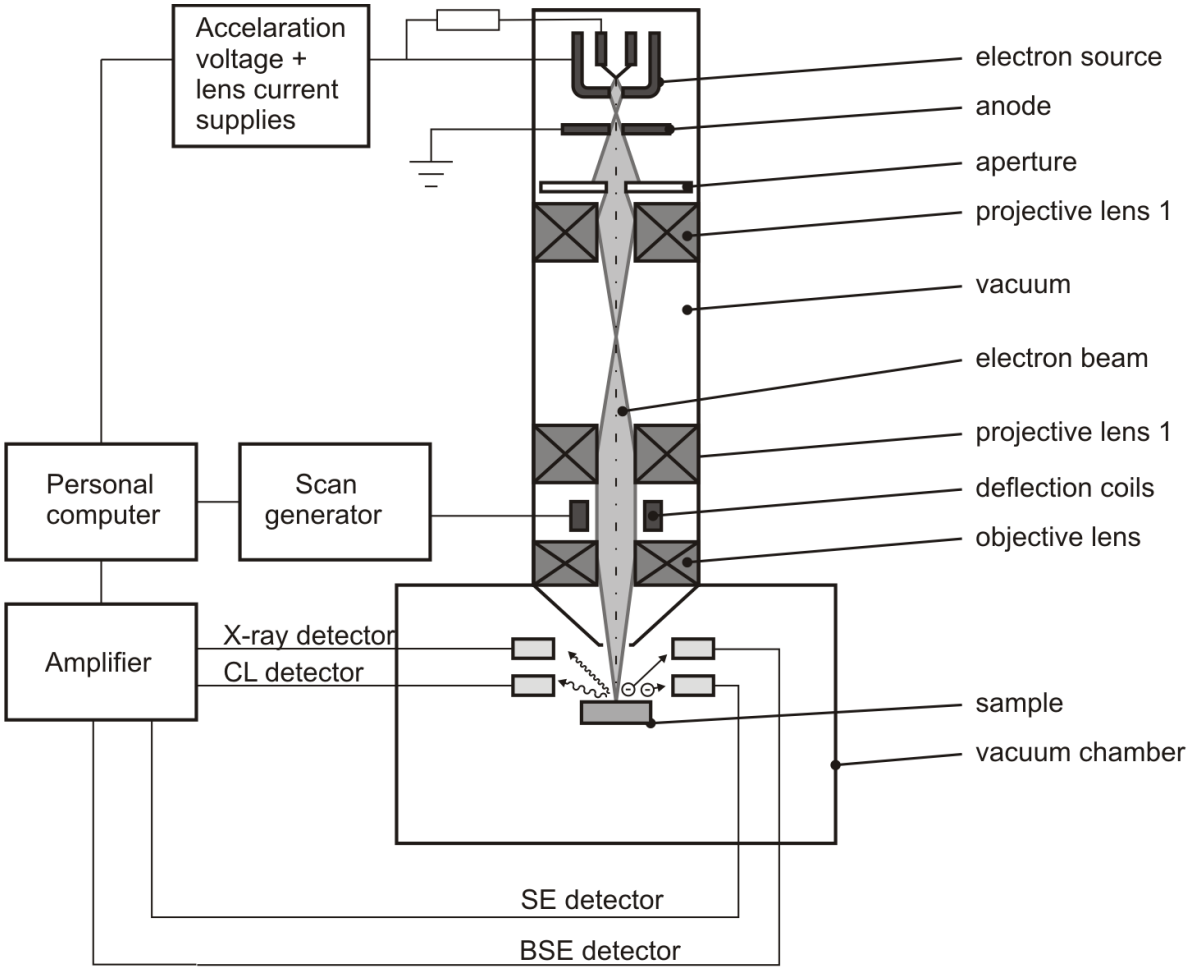

Fig. 3.1: Construction of SEM microscope.

φ [eV]	λ [m]	$\frac{v}{c}$	$\frac{m}{m_0}$
10^0	$1.22651{\cdot}10^{-9}$	0.00198	1.00000
10^1	$3.87853{\cdot}10^{-10}$	0.00626	1.00002
10^3	$1.22055{\cdot}10^{-11}$	0.19497	1.01957
10^6	$8.72001{\cdot}10^{-13}$	0.94107	2.95672
10^8	$1.23371{\cdot}10^{-14}$	0.99999	196.67194

Tab. 3.1: Parameters of an electron as a function of its energy (φ is the energy, λ is the wavelength, v is the speed, c the speed of the light, m is the mass and m_0 is the rest mass of the electron)

Instead of solving the equation of motion, which is complicated, the trajectory equation $x = x(z)$ and $y = y(z)$ is computed. This equation is derived from equation 3.2 [53, 54] and it is expressed as

$$\frac{\mathrm{d}}{\mathrm{dz}}\left(w'\sqrt{\frac{\Phi^*}{1+w'\overline{w}'}}\right) = -\frac{\gamma}{2}\sqrt{\frac{1+w'\overline{w}'}{\Phi^*}}E_w - \mathrm{i}\eta(B_w - w'B_z), \tag{3.4}$$

where Φ^* is a so-called relativistic corrected potential, which is defined as

$$\Phi^* = \Phi\left(1 + \frac{e}{2mc^2}\Phi\right), \tag{3.5}$$

where Φ is the accelerating bias, the w, E_w and B_w are the complex variables defined as

$$w(z) = x(z) + \mathrm{i}y(z), \tag{3.6}$$

$$E_w(z) = E_x(z) + \mathrm{i}E_y(z), \tag{3.7}$$

$$B_w(z) = B_x(z) + \mathrm{i}B_y(z) \tag{3.8}$$

where i is the imaginary unit. The symbol $\overline{w}$ denotes the complex conjugated variable and the symbol w' represents the derivative with respect to z

$$w' = \frac{\mathrm{d}w}{\mathrm{d}z} \tag{3.9}$$

and η is defined as

$$\eta = \sqrt{\frac{e}{2m}}. \tag{3.10}$$

The primary electron beam is located close to the optical axis of the system and so equation 3.4 can be rewritten into the so-called paraxial equation [54]:

$$w'' + \left(\frac{\gamma\phi'}{2\phi^*} - \frac{\mathrm{i}\eta}{\phi^{*\frac{1}{2}}}B\right)w' + \left(\frac{\gamma\phi''}{4\phi^*} + \frac{f_1^2}{8\phi^{*2}} - \frac{\mathrm{i}\eta}{2\phi^{\frac{1}{2}}}B'\right)w + \left(\frac{\gamma f_1^2}{8\phi^{*2}} + \right.$$
$$\left. + \frac{\gamma f_2}{\phi^*} + \frac{2\eta}{\phi^{*\frac{1}{2}}}d_2\right)\overline{w} = -\frac{\gamma U_1 F_1}{2\phi^*} + \frac{\eta}{\phi^{*\frac{1}{2}}}I_1 D_1 - \frac{\gamma f_1}{2\phi^*} + \frac{\eta}{\phi^{*\frac{1}{2}}}d_1, \tag{3.11}$$

where $\phi = \phi(z)$ is the electrostatic potential, $B = B(z)$ is the magnetic flux density, $f_1 = f_1(z)$ is the electrostatic dipole field, $d_1 = d_1(z)$ is the magnetostatic dipole field, $F_1 = F_1(z)$ is the electrostatic deflection field, $D_1 = D_1(z)$ is the magnetostatic deflection field, $f_2 = f_2(z)$ and $d_2 = d_2(z)$ are the quadrupole field. All fields are axial.

Since the primary beam is located near the optical axis of the system and its size is adjusted by apertures optical aberrations of the microscope can be neglected up to the the objective lens. The abberations of the objective lens has a crucial influence on the final size of the spot.

The calculation of the whole electron trajectory and optical aberrations are complicated and so nowadays softwares are used to compute them.

3.4. Electron guns

Electron guns are used to create electron beams with adjustable energy and current. Nowadays there are two main types of electron guns: thermionic emission gun and field emission gun.

Several parameters are defined to describe the quality of the electron gun:

- **Brightness β:** It is defined as the beam current density j per a solid angle α [51]:

$$\beta = \frac{j}{\pi\alpha^2}. \tag{3.12}$$

Brightness is constant through the whole optical system [53]

$$\beta = \frac{4I_{\mathrm{G}}}{\pi^2 d_{\mathrm{G}}^2 \alpha_{\mathrm{G}}^2} = \frac{4I_0}{\pi^2 d_0^2 \alpha_0^2}, \tag{3.13}$$

where I_{G} is the current at the beam spot on the specimen, I_0 is the current at the crossover of the electron gun, d_{G} is the diameter of the beam on the specimen, d_0 is the diameter of the beam at the crossover, α_{G} is the objective aperture angle of the beam and α_0 is the aperture angle at the gun crossover. No apertures between the electron gun and the objective lens and no interaction of electrons between each other in the beam are considered in equation 3.13.

- **Energy spread ΔE:** All electrons do not have the same energy. It can be caused by fluctuation of extracting voltage, different speed of electrons emitted from the cathode or by Boersch phenomenon under high current densities at the crossover (Coulomb interactions of electrons) [55].

- **Work pressure P_{w}:** The vacuum is necessary to avoid oxidation of the cathode and collisions of electrons with other particles because they causes an energy spread and deteriorate optical properties of the beam.

- **Emission current I_{e}:** It is a current emitted by the cathode.

- **Work temperature T_{w}:** Higher temperature of the active part increases the emission current and decreases the life time of the electron gun.

- **Lifetime t_{L}:** The lifetime of the electron gun is limited at most by the lifetime of the active area of the cathode. It depends on the material and the design of the active area.

3.4.1. Thermionic emission gun

This gun consists of the cathode made of a tungsten filament and extraction electrodes. A typical design is shown in Fig. 3.2.

Heating up the cathode increases the thermal energy of its electrons. When this energy is higher than the work function of the cathode, then electrons escape. The voltage applied on the Wehnelt cylinder causes that only electrons emitted from a small area of the cathode (typically $100\times150\,\mu\mathrm{m}^2$) can escape from the cathode. The anode is commonly grounded or positive voltage is applied to it to accelerate electrons.

The emission current density j_{e} is given according to the Richardson law [51]

$$j_{\mathrm{e,term}} = ATe^{-\frac{\Phi_{\mathrm{m}}}{k_{\mathrm{B}}T}}, \tag{3.14}$$

where A is the material constant, T is the temperature of the cathode material, Φ_{m} is the work function of the cathode material and k_{B} is the Boltzmann constant.

To increase the brightness β of the electron gun another material like lanthanum hexaboride LaB_6 is used instead of tungsten. Parameters of tungsten and lanthanum hexaboride cathode are written in Tab. 3.2 and the design of the cathode is shown in Fig. 3.3.

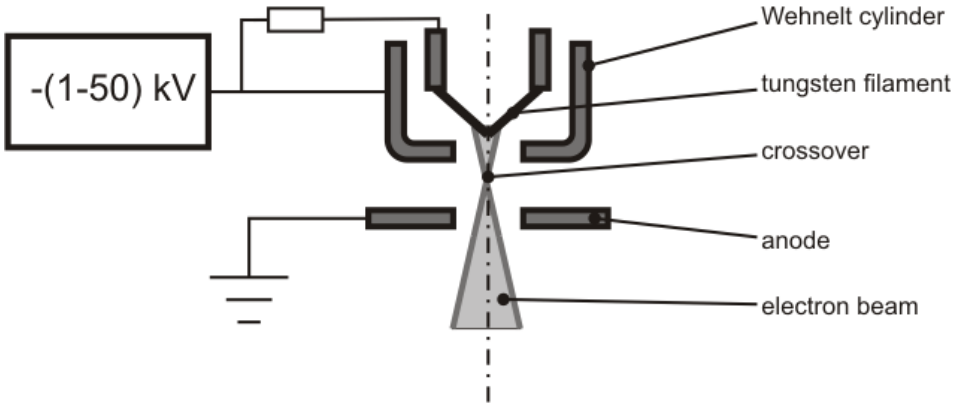

Fig. 3.2: Thermionic electron gun.

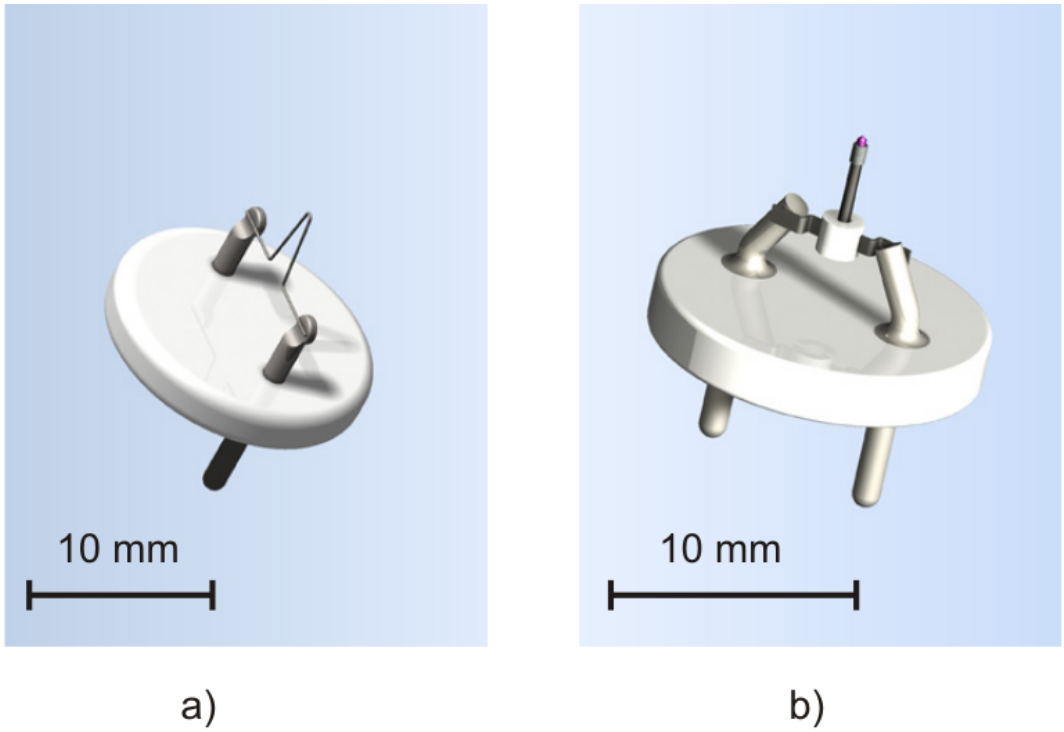

Fig. 3.3: Filament of an thermionic electron gun: a) tungsten, b) lanthanum hexaboride (taken from [56]).

3.4.2. Field emission gun

To obtain higher brightness and narrower energy spread the field emission gun (FEG) is used. A typical design is shown in Fig. 3.4. The field emission gun is based on the tunneling phenomenon. A sharp tungsten tip (apex radius around 50 nm) is located near a strong positive potential (1-50 kV) and electrons from the area close the tip apex can tunnel out of the tip and create the primary beam.

The emitted current density j_e is expressed according to the Fowler-Nordheim formula [54]

$$j_{\mathrm{e,feg}} = \frac{c_1}{\Phi_{\mathrm{m}}} E^2 e^{-\frac{c_2 \Phi_{\mathrm{m}}^{\frac{3}{2}}}{|E|}}, \tag{3.15}$$

where c_1 and c_2 are the material constants, E is the electric field and Φ_{m} is the work function of the material.

Parameters of the field emission gun in comparison with thermionic guns are in Tab. 3.2.

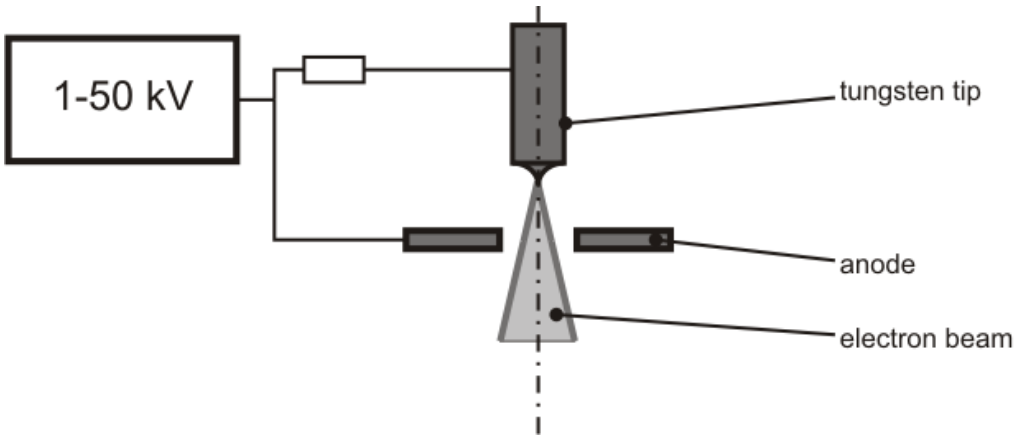

Fig. 3.4: Field emission gun.

Parameter	Thermionic W	LaB_6	FEG
Brigtness β [$Acm^{-2}sr^{-1}$]	10^5	10^6	$10^7 - 10^8$
Energy spread ΔE	1-3	0.5-2	0.2-0.4
Work pressure P_{w} [Pa]	10^{-3}	10^{-4}	$10^{-8} - 10^{-9}$
Emitted current I_{e} [μA]	100	1-50	10
Work temperature T_{w} [K]	2700-3150	1800-2100	300
Life time t_{L} [h]	115-1	7900-17	>8000

Tab. 3.2: Parameters of electron guns [51, 53]

3.5. Charged particle optics

Electrostatic or magnetostatic lenses are used in the SEM to demagnify and to image the electron source at the specimen .

3.5.1. Electrostatic lenses

An electrostatic lens can consist of one or more rotationally symmetric electrodes with the symmetry axis identical with the optical axis. A two electrodes design is shown in Fig. 3.5.

The trajectory equation of this lens can be obtained from the equation 3.11 when only the terms including ϕ' and ϕ'' are considered [54]

$$w'' + \frac{\gamma\phi'}{2\phi^*} w' + \frac{\gamma\phi''}{4\phi^*} w = 0. \tag{3.16}$$

Electrostatic lenses are generally installed in electron guns and are suitable to work with slow electrons (energy around 1-100 eV) in low energy SEM. These lenses are mostly used to accelerate or decelerate electrons.

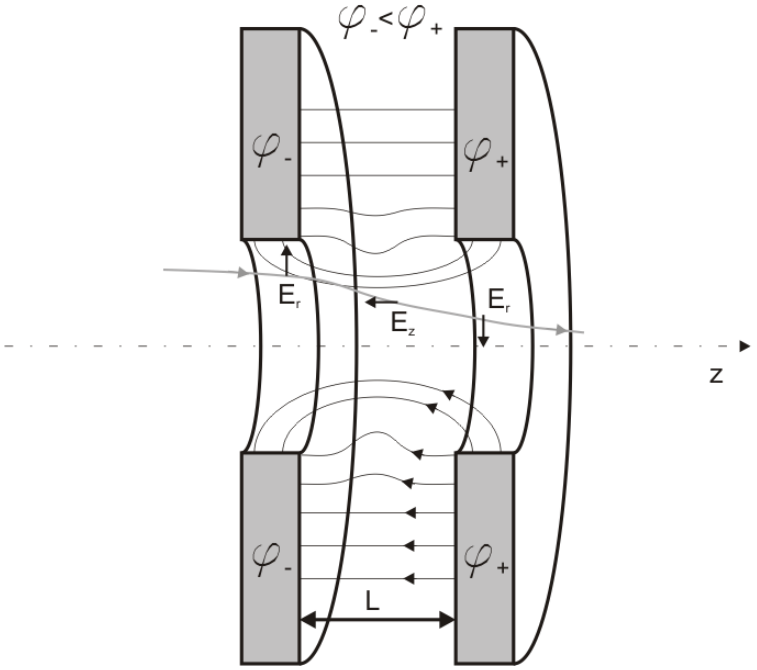

Fig. 3.5: Electrostatic lens - the principle of focusation.

3.5.2. Magnetostatic lenses

The magnetic lens has a quite different design than the electrostatic one. A magnetic field is generated by a solenoid and a magnetic flux is guided by pole pieces. A general design is shown in Fig. 3.6.

The trajectory equation of the magnetic lens can be expressed from equation 3.11 as [54]

$$w'' - \mathrm{i}kBw' + \frac{1}{2}kB'w = 0, \tag{3.17}$$

where k is defined as

$$k = \frac{\eta}{\phi^{*\frac{1}{2}}}. \tag{3.18}$$

We rewrite $w(z)$ to the polar coordinates

$$w(z) = r(z)e^{(\mathrm{i}\theta(z))} \tag{3.19}$$

and substitute it into equation 3.6. We obtain two equations

$$r'' + \frac{k^2B^2}{4}r = 0, \tag{3.20}$$

and

$$\theta' = \frac{k}{2}B. \tag{3.21}$$

The magnetic lenses rotate an image by the angle θ

$$\theta = \frac{k}{2} \int_{z_{\text{object}}}^{z_{\text{image}}} B(z) \mathrm{d}z, \tag{3.22}$$

where z_{object} and z_{image} are the distances of the object and the image from the centre of the lens, respectively.

Magnetic lenses are used as projective and objective lenses. They have smaller optical aberrations than electrostatic ones generally.

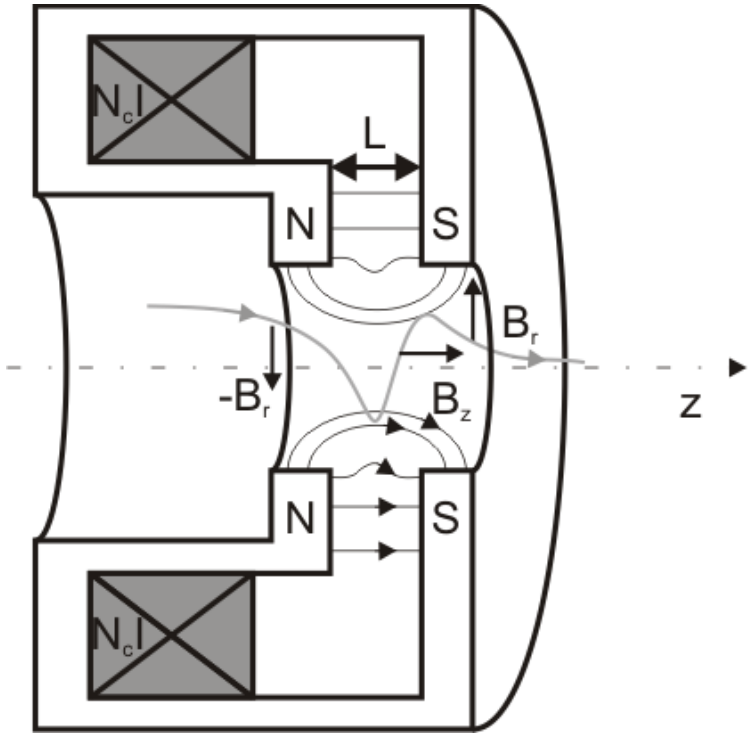

Fig. 3.6: Magnetic lens - principle of focusation (rectangulars with diagonals denote a coil with N_c turns and the current I).

3.5.3. Imperfections of lenses and resolution

In the analogy to light optics, electrostatic and magnetostatic lenses have optical imperfections as well. They are caused mainly by imperfections of rotation symmetry of lenses, inhomogeneities in material in the case of magnetic lenses and by an energy spread of particles.

Three main effects increasing the final spot size at the plane of the specimen are [51, 53, 55]:

- **Spherical aberration:** The electrostatic or magnetostatic field decreases from border of an electrode or pole pieces to the optical axis. It causes that electrons flown far from optical axis intersect it before the Gaussian focal plane (see Fig. 3.7 a). The image of the point source is not a point but a spot with the diameter d_{S} (in the waist of electron beam) [53, 55]

  $$d_{\text{S}} = 0.5 C_{\text{S}} \alpha^3, \tag{3.23}$$

  where C_{S} is the coefficient of the spherical aberration and α is the aperture angle of the beam.

- **Chromatic aberration:** The electron beam is not exactly monochromatic and the dispersion takes place (see Fig. 3.7 b). The spot diameter caused by the energy spread ΔE of electrons is (in the waist of the electron beam) [53, 55]

$$d_{\mathrm{C}} = C_{\mathrm{C}} \alpha \frac{\Delta E}{E}, \tag{3.24}$$

  where C_{C} is the coefficient of the chromatical aberration, E and ΔE are the energy and the energy spread of the electron beam, respectively.

- **Diffraction:** Electrons show up a wave properties. So the diffraction of the beam on the final aperture has to be taken into account too. The point source is imaged as a spot with the diameter d_{D} [53, 54]

$$d_{\mathrm{D}} = \frac{0.61\lambda}{\alpha}, \tag{3.25}$$

  where λ is the wavelength of the electron.

The crossover of an electron gun with the diameter d_0 is imaged by lenses to the spot at the specimen with the diameter d_{G}. Because the contributions caused by aberrations and diffraction are small, the linear summation of the contributions can be used. The final diameter d_{P} of the spot is [51, 55]

$$d_{\mathrm{P}} = \sqrt{d_{\mathrm{G}}^2 + d_{\mathrm{S}}^2 + d_{\mathrm{C}}^2 + d_{\mathrm{D}}^2}, \tag{3.26}$$

where d_{G} is determined from equation 3.13.

The dependance of the spot diameter d_{P} at the specimen on the aperture angle α is shown in Fig. 3.8. To find an optimal aperture angle α_{opt} for which the diameter d_{G} is minimal the equation

$$\left.\frac{\partial d_{\mathrm{P}}}{\partial \alpha}\right|_{\alpha=\alpha_{\mathrm{opt}}} = 0 \tag{3.27}$$

has to be solved.

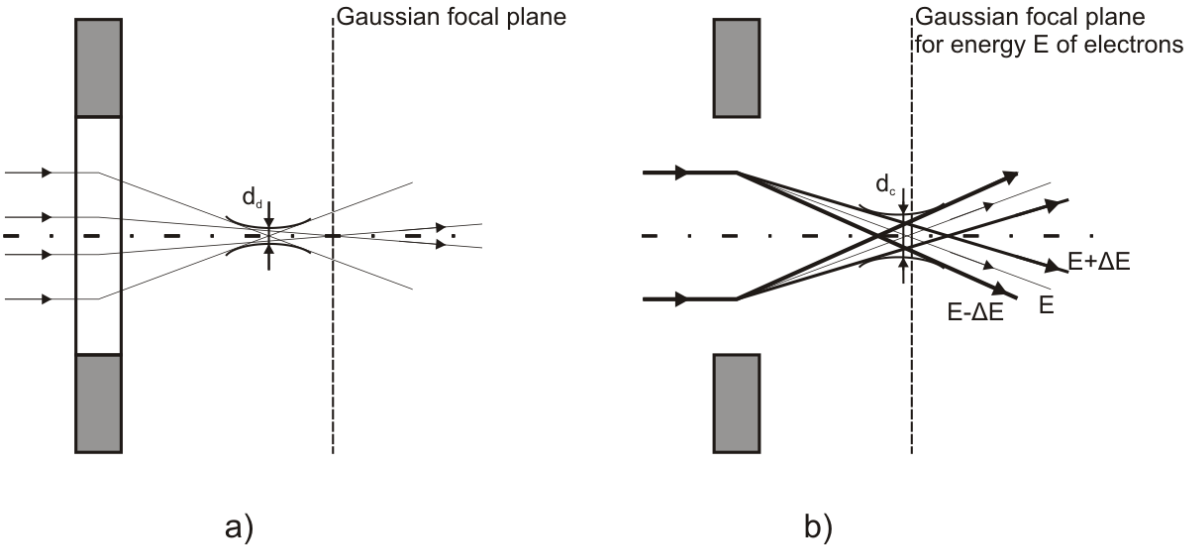

Fig. 3.7: Imperfections of lenses: a) spherical aberration, b) chromatic aberration.

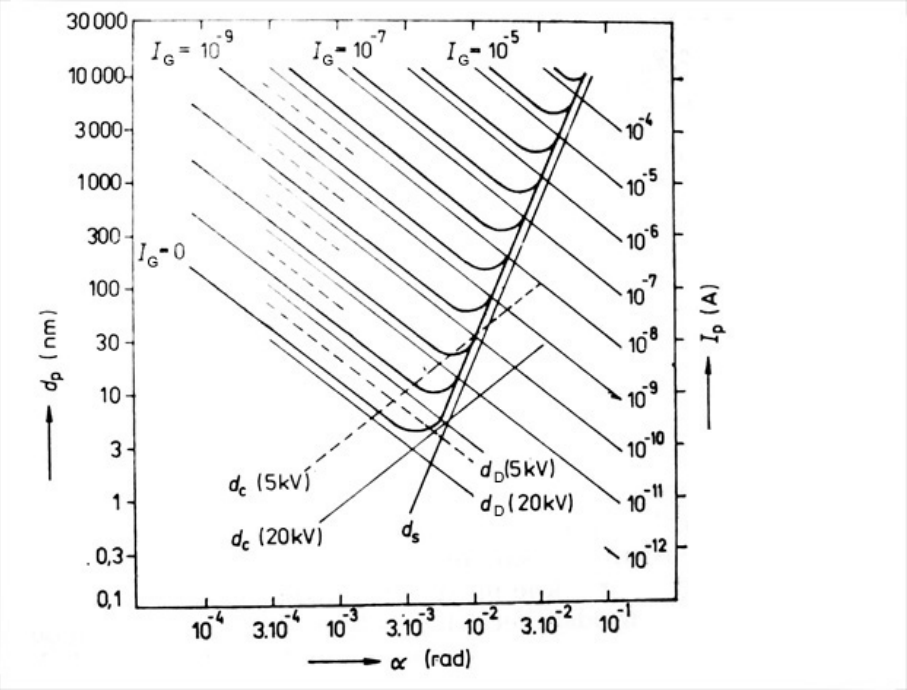

Fig. 3.8: Spot diameter d_P as a function of the current of the primary beam I_G, final aperture α and influences of lens imperfections (d_S, d_C, d_D - the diameter caused by the spherical, chromatic aberration and by diffraction, respecitvely, taken from [55]).

3.6. Electron beam interaction with a specimen

When the primary beam of electrons impinges the specimen its electrons start to interact with specimen atoms and free electrons. These interactions cause the scattering of electrons. There are two types of scattering [51]:

- **Elastic scattering:** The impinging electrons are affected by a field generated by atoms of the specimen. It causes only a change of the electron original direction and particulary no kinetic energy losses appear.
- **Inelastic scattering:** Interactions of primary beam electrons with electrons in the bands and inner shells of atoms change the original direction and kinetic energy of electrons.

Interactions of primary beam electrons with a specimen generate the following main signals being used for microscopy and analysis of specimens [51, 53]:

- **Secondary electrons:** They come from the upper layers of the sample. They originate in maximal depth D_{SE} being 5 nm for metals to 75 nm for insulators (see Fig. 3.9). They are generated by inelastic interactions and their kinetic energy ranges from 2 eV to 50 eV with a peak around 2 eV - 5 eV (see Fig. 3.10).
- **Back scattered electrons:** They are primary electrons which are reflected back from the sample and loose kinetic energy during interactions with the specimen. Their energy ranges from 50 eV to the energy of the primary beam electrons E_0 (see Fig. 3.10) and they give us information from the higher depth D_{BSE} of the sample than secondary electrons (see Fig. 3.9).

- **Auger electrons:** They can be generated when an electron from an inner shell is removed. Auger electrons enables us to determine the elemental composition of the specimen because their energy is characteristic for each elements. This energy is higher than the energy of secondary electrons typically (see Fig. 3.10). They can escape only from outermost layers D_{AE} 1 nm, and hence, they give us very good vertical and lateral resolution (see Fig. 3.9).
- **X-ray:** When the primary beam electron interacts with electron of an inner shell of an atom it can generate characteristic X-rays. The depth of X-ray generation $D_{\mathrm{X-ray}}$ is shown in Fig. 3.9.
- **Cathodoluminiscence:** When an electrons from a valence band miss photons can be emitted when this valence band is filled up by electrons again.

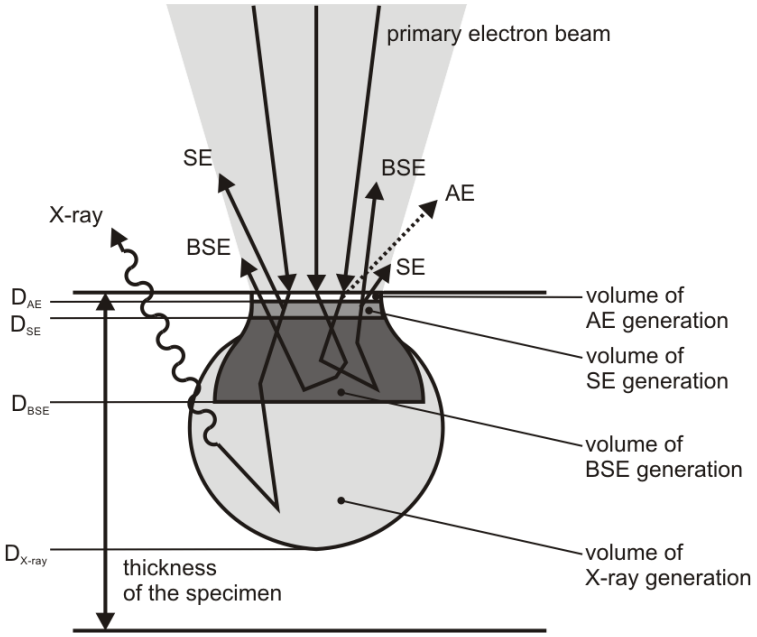

Fig. 3.9: Volumes of signals generation.

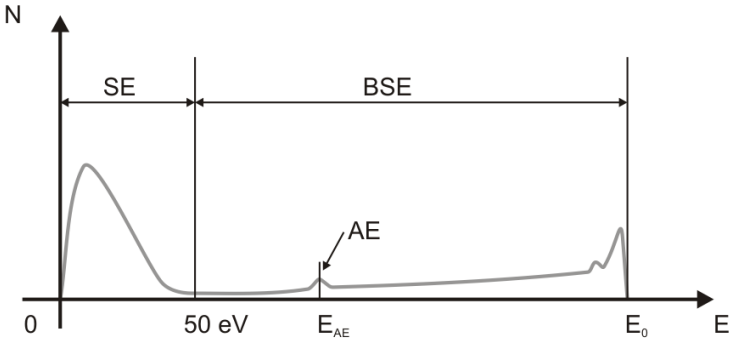

Fig. 3.10: Schematic energy distribution of electrons emitted from a specimen (SE - secondary electrons, BSE - backscattered electrons, AE - Auger electrons, E_0 - energy of the primary beam) [51].

3.7. Detectors used for SEM

Various types of signals are created when an electron beam interacts with a specimen. The following detectors are used :

- **Everhart-Thornley detector:** It is used mainly to detect the secondary electrons. The schematic image of this detector is shown in Fig. 3.11. Secondary electrons are attracted by the positive voltage on the collector. Electrons impinging on the scintillator crystal emit photons the number of which number is proportional to the number of electrons. Photons are guided by a light pipe to a photocathode where they are converted to electrons. This signal is increased by an electron multiplier by 10^6 times.

  This detector can be also used to detect backscattered electrons but its efficiency is very low in this case, therefore, another type of the detector is used [51, 55].

- **Detector of backscattered electrons:** To record these electrons usually semiconductor detector is used. When electron impinges on the silicon crystal the pair of an electron and a hole is created. The mean number of pairs n is equal

$$n = \frac{E_{\mathrm{BSE}}}{E_{\mathrm{eh}}}, \tag{3.28}$$

  where E_{BSE} is the energy of the backscattered electron and E_{eh} is the mean energy of the electron hole pair (which is 3.6 eV in silicon). An electric field is applied to separate holes and electrons. They are collected on electrodes and their number is proportional to backscattered electron energy E_{BSE} [51, 55].

  This detector is placed as close as possible (3 mm typically) to the specimen to increase the collecting angle of backscattered electrons [51].

- **Detectors of Auger electrons:** To distinguish Auger electrons in the energy range from 50 eV to several keV with a high energy resolution cylindrical mirror analyzer, Staib analyzer, hemispherical deflector analyzer are used [51, 53].

- **X-ray and cathodolumiscence detectors:** Detection of the light or X-ray is based on the photoeffect. The photon "kicks out" an electron or an pair of an electron and a hole is created. Electrons and holes are collected by the electrodes (for more detail explanation see [51] Chapter 8).

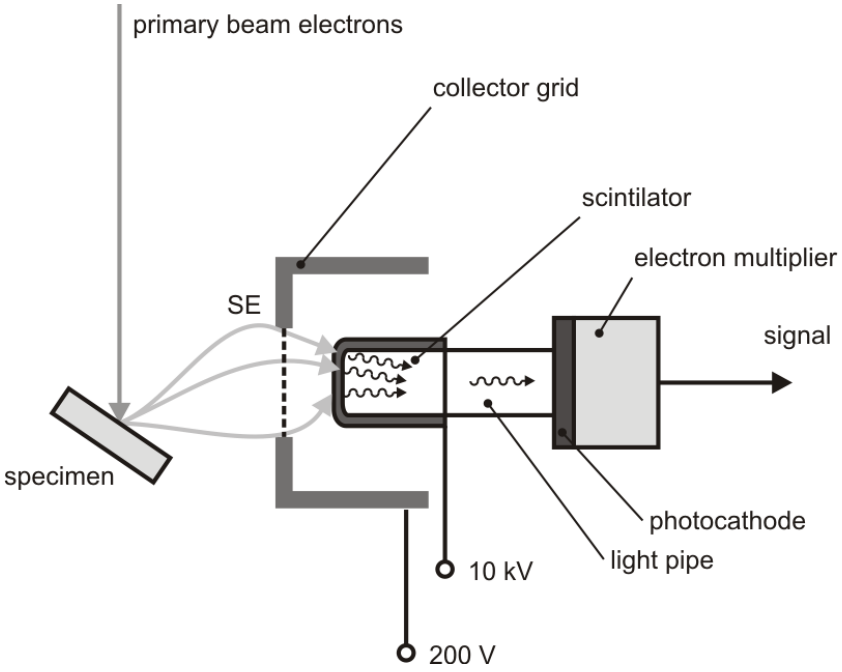

Fig. 3.11: Everhart-Thornley detector [51].

Chapter 4

Design of the UHV combined AFM/SEM system

4.1. Introduction

Combination of AFM and SEM brings new possibilities in microscopy and analysis of surfaces.

The main advantage of this combined system is a high resolution and a wide scanning range (see Fig. 4.1). Another one is possibility to obtain information from many different detectors at the same time. For example, it is possible to scan a sample by AFM, SEM and make Auger electron spectroscopy at the same time.

The combination of AFM and SEM is attractive but, on the other hand brings many additional problems. The main problem is to design the AFM/SEM setup enabling both units to work together. A few design proposals have been done [25] and at this moment also one commercial device is available [26]. Nevertheless, these systems have many limitations the size of the sample, incapability form more than two analytic techniques simultaneously, etc.

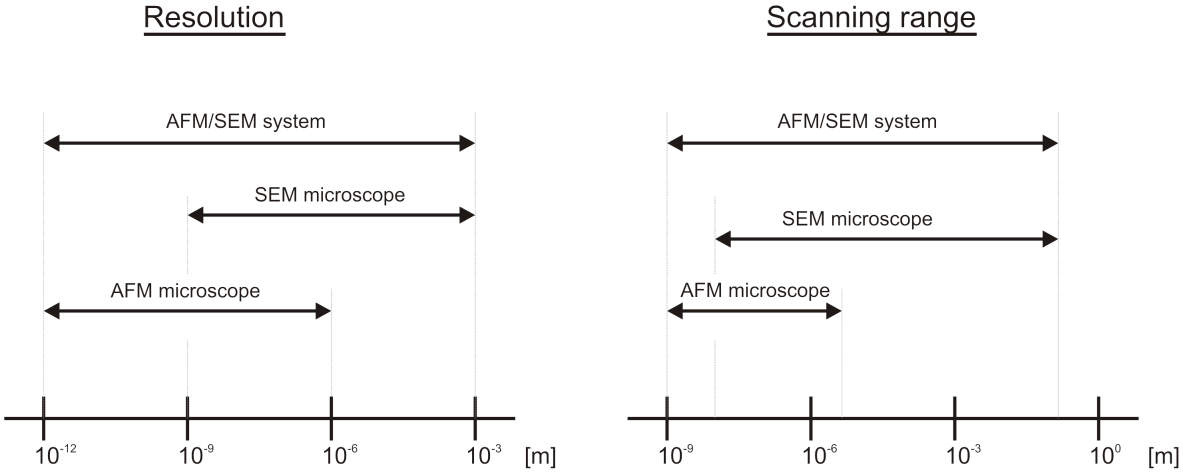

Fig. 4.1: Resolution and scanning range of AFM, SEM and the AFM/SEM system.

The goal of this work is to design a new AFM/SEM combined system with minimum limitations and having a reasonablle capability to work together with other an-

alytic techniques such as Back Scattered Electron microscopy (BSE), Scanning Auger Microscopy (SAM), Energy Dissipative X-Rays spectroscopy (EDX), etc.

The system design was based on an AFM microscope proposed by Vít Křenek [7] and SEM Mira produced by Tescan, s.r.o. [57].

It was found that the AFM microscope does not have a functionable *x,y,z* sample transport and mirror motion system [61]. Therefore, it was necessary to design new systems or to modify the old ones.

All design works were done in the environment of Catia V5 R15.

4.2. Former and new design of the AFM microscope

In 1997 Filip Lopour designed the first AFM microscope in the Institute of physical engineering (IPE) at Brno University of Technology within his diploma project [8]. which was considered to work under ultra high vacuum (UHV) conditions.

The next AFM microscope made in IPE was proposed by Vít Křenek in 2003 [7]. It was designed to co-operate with SEM. This device has an inovative design (see Fig. 4.2) in comparison with other AFM microscopes.

In this microscope the deflection of a cantilever is detected by an optical beam system. The cantilever is fixed to a holder which is mounted on the top plate of the microscope. Scanning is done by a piezoscanner to which the sample holder is fixed. The transport of the sample through longer distances (more than 5 μm) is provided by the *x,y,z* motion system (green-colored parts in Fig. 4.2).

The *x,y,z* motion system consists of two subsystems. The first subsystem is the *x,y* transport system based on the slip-stick motion. The second subsystem is the transport system in *z* axis using an inchworm. Scanning is provided by a piezoscanner which is a part of the inchworm herewith.

The positioning system of the mirrors is unique. The mirrors are setup at a fixed angle and focusing the laser beam on the cantilever is provided by a change of the position of a laser subsystem (pink colored parts in Fig. 4.2). The adjustment of the PSPD is done in the same way.

The manipulations of the previous design is based on slip-stick principle [7]. In this design the gravity is the only force which affects the piezoelement and defines the friction force between the slip-stick parts [7]. However, this force is constant and cannot be readjusted.

The assembly and testing of this AFM microscope was a subject of diploma project of Stanislav Antoš. He found that the piezomotion system did not work in the AFM microscope. To resolve a source of this problem a change of the friction constant between the slip-stick parts was proposed. A glass desk instead of the steel plate was tested. A motion was observed but it was not reproducible. The speed was in the range from $0.03\,\mathrm{mm{\cdot}s^{-1}}$ to $0.06\,\mathrm{mm{\cdot}s^{-1}}$ but it varied from test to test. The motion was not linear and the wagon tended to rotate. To improve the reproducibility of the motion a diamond like carbon (DLC) layer was deposited to increase the hardness of the contact surface and to avoid a mutual wear of the parts. However, it was found that the influence of this layer on the motion was insignificant [61].

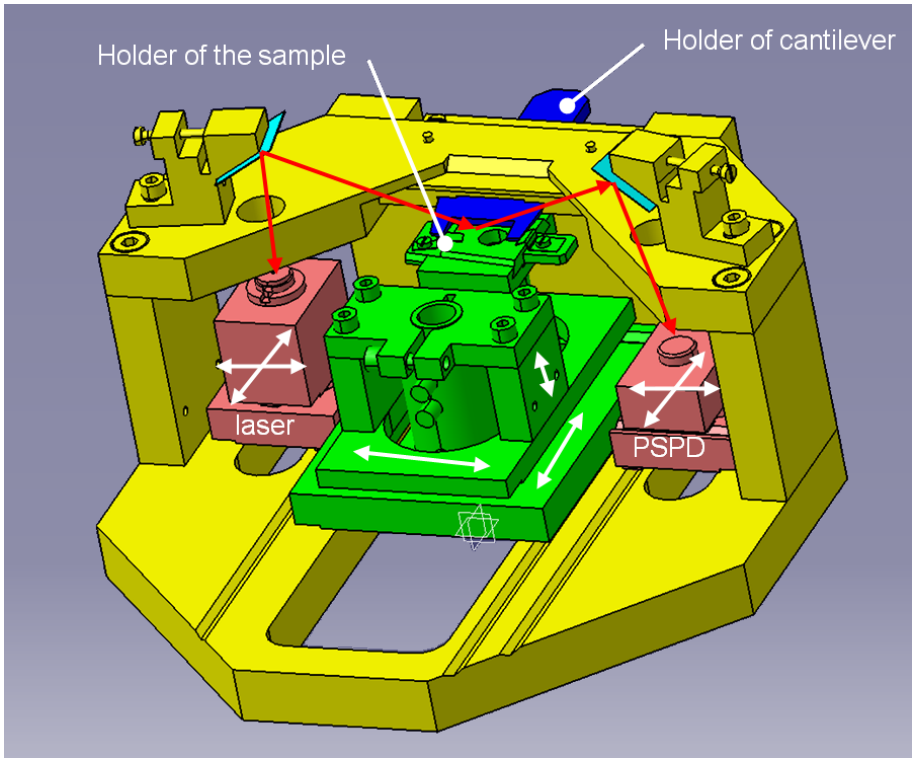

Fig. 4.2: AFM microscope designed by Vít Křenek.

4.2.1. Principle of the slip-stick piezosystem

The slip-stick piezomotion is very often used for nanopositioning [58, 59,62]. Its principle is demonstrated in Fig. 4.3 [7, 61]. The slip-stick piezosystem consists of three main parts: a wagon, a piezoceramic plate and a base. The motion step can be divided into three actions:

a) Initial state of the slip-stick piezosystem (see Fig. 4.3 a).

b) The bias is applied between two electrodes of the piezoceramic plates gradually. It causes an extension Δx_1 of the piezoceramic plate in x axis (see Fig. 4.3 b).

c) The bias is switched off as fast as possible. It causes a contraction of the piezoceramics plate to the original state and a slip of the wagon for the distance Δx_2 (see Fig. 4.3 c).

The whole motion consists of many steps. The speed can be adjusted by frequency of pulses or by an extension of the piezoceramic plate during one step. The resolution of this motion system is given by the applied bias and it is in the order of nms [58].

Although the extension of the piezoceramic plate Δx_1 should be theoretically the same as the distance of motion of the wagon Δx_2 experiments showed that the wagon motion is smaller than the extension of the piezoceramic plate $\Delta x_1 > \Delta x_2$. It can be explained by an imperfect slip of the wagon in the action c.

The frequency of applied pulses should influence only the speed of the wagon. However, it was found that the motion of the wagon works only in a certain frequency range of applied steps ($\approx 10^2$ Hz). The experiments show that the frequency range can depend on resonant frequency of the whole system, a shape of pulses, the friction force between the wagon and the piezoceramic plate.

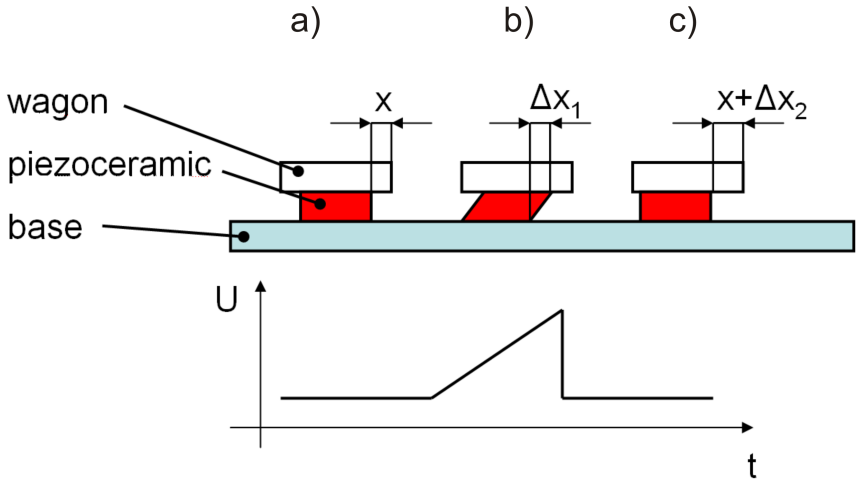

Fig. 4.3: Principle of a slip-stick piezomotion: a) initial state , b) application of the bias and piezoceramic plate extension, c) switch off of the bias and a slip of the wagon.

4.2.2. Testing the piezomotion system

To find a frequency range of the wagon motion a controlling program was designed. Its scheme is shown in Fig. 4.4.

The principle of this system is based on the detection of a voltage bias change on the photodiode. A light emitted diode is used as the light source. The wagon is set in the middle of the photodiode to detect both directions of motion. The motion of the wagon causes a change of the measured voltage bias on the photodiode. The system consists of the following parts (see Fig. 4.4):

- **Timer** defines the time dwelling on each frequency.
- **Table of the pulse shape** determines the shape of an applied bias pulse.
- **Frequency changer** defines the lowest and highest frequency of a testing frequency range and the frequency step.
- **Digital output mixer** converts the pulse shape with the frequency to digital data.
- **D/A converter** transforms the digital data to analogue values.
- **High voltage (HV) amplifier** increases the signal from the D/A converter to a required value (in our case 200 V).
- **Wagon** shades the photodiode during the motion.
- **Light emitted diode** is used for the illumination.
- **Photodiode** measures the amount of incident radiation.
- **A/D converter** changes analogue values to digital data.
- **Digital input** acquires data from A/D converter and sends it to the table of bias vs. frequency.
- **Table of bias vs. frequency** consists of the dependance of the photodiode voltage bias on the frequency of the applied pulse.

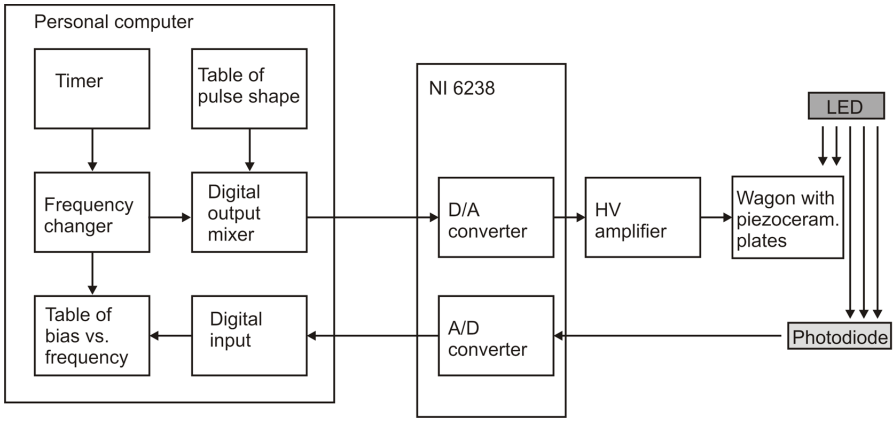

Fig. 4.4: Scheme of the program for finding a frequency range of the slip-stick motion system.

This idea was programmed in the environment of C++ by Jiří Pavelec.

The measurement for one wagon of the AFM microscope is shown in Fig. 4.5. The motion was observed only in forward direction. If backward pulse was applied, no movement was recorded. To verify a possible tilt of the system or some inhomogeneity of the contact surface the whole AFM microscope was rotated by 180°. The motion appeared in the same direction as in the previous case. Wagon did not move in the opposite direction again. It can be explained by tilt of the AFM microscope. It could cause that a small component of gravity parallel with AFM base helped to move the wagon around resonant frequency of the system. The tilt of the AFM microscope was around 3°.

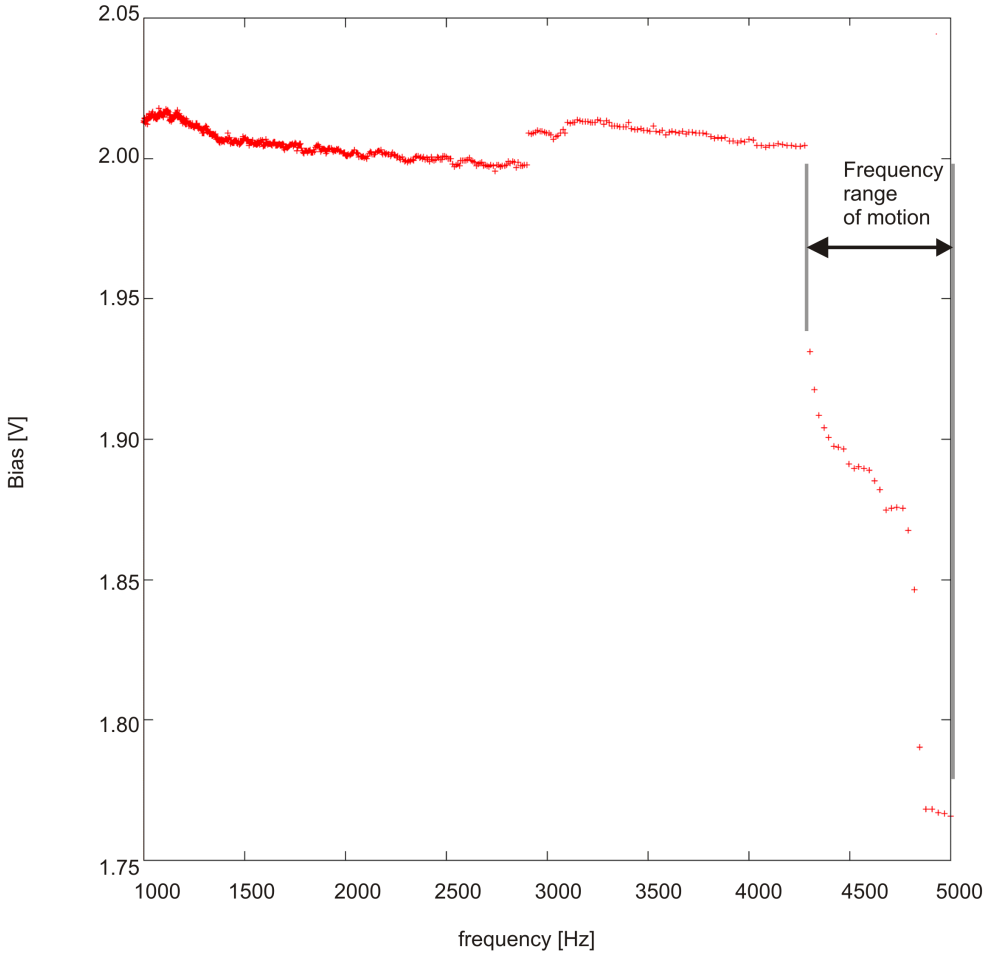

Fig. 4.5: Dependence of the photodiode voltage bias on the frequency of pulses (the frequency dwelling time 20 s).

4.2.3. Modification of the motion system of the sample holder

From the reasons mentioned in the previous text it was necessary to design a new motion system of the sample holder.

It was chosen to use the system based on the principle proposed by Kleindiek [58]. A similar device was designed in the IPE by Petr Kalina in 2006 [59]. Its components were fabricated, but not complectly assembled. Finishing and testing this device enabled us to find all consequences of this design.

Kalina´s motion system is shown in Fig. 4.6. It is based on the slip-stick principle which is based on a sapphire halfrod and V-groove. The motion of halfrods is provided by stuck piezoelements. A setup of the sapphire halfrod is managed by two finalizing bolts (see Fig. **??**). It enables us to rectify production inaccuracy. The leaf spring was exploited to provide a finer adjustment of the system via its soft bending. The leaf sping P is designed to hold seting constant.

For testing of the system only the z-wagon was used. The results were as follows:

- **First testing:** The system was assembled without any exact accuracy. It was tested only with z-wagon (25 g). It worked in both required directions reproductively and the speed was estimated 0.25 mm·s^{-1} approximately. The motion range was higher than 10 mm.

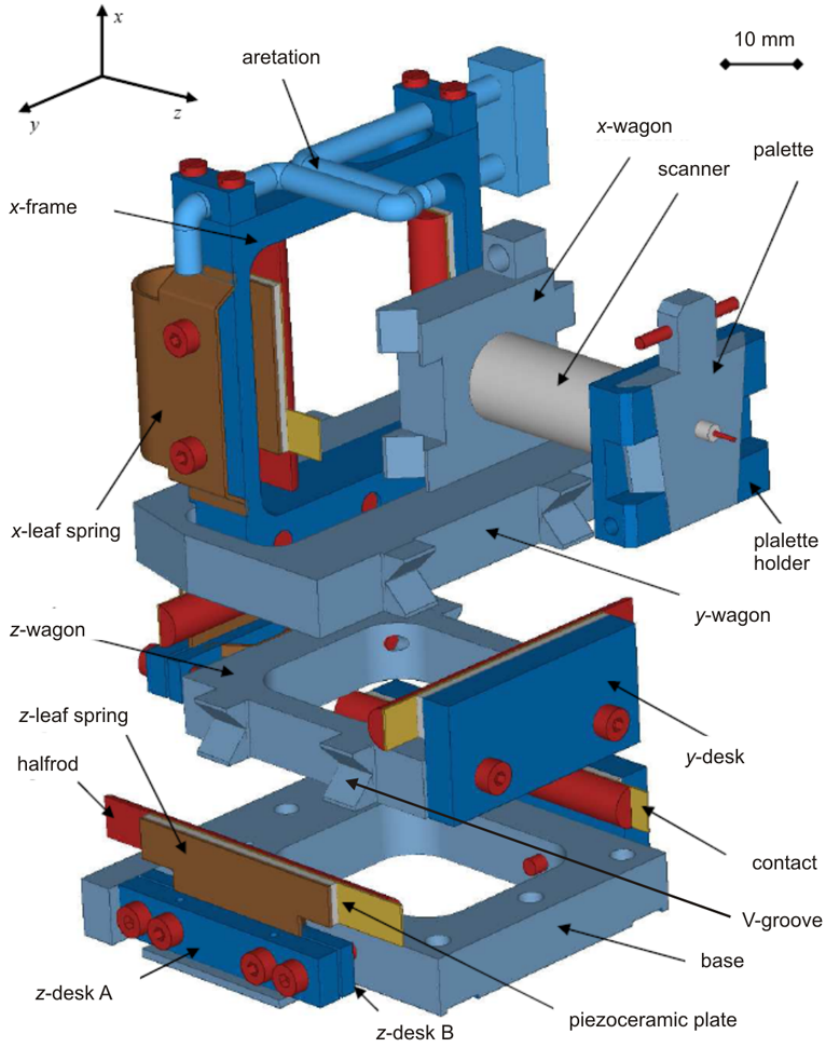

Fig. 4.6: Kalina´s motion system (taken from [59]).

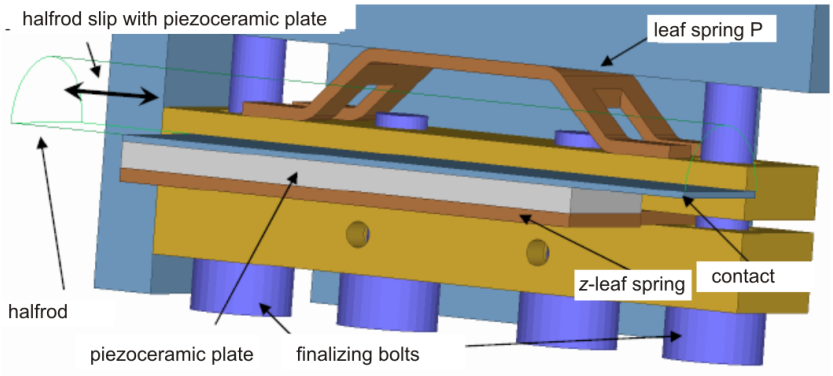

Fig. 4.7: Kalina´s motion system - details of halfrod and V-groove (taken from [59]).

- **Second testing:** It was done one week after the first testing. It worked with a lower speed around 0.08 - 0.1 mm·s^{-1}. The full load (y-wagon and x-wagon and x-frame, ..., 103 g) was applied. It needed a new mechanical setup. The speed was around 0.05 - 0.07 mm·s^{-1}). The motion range was higher than 10 mm.

- **Third testing:** It did not work two weeks after the second testing. A new mechanical adjustment was done. It moved in the forward direction correctly but for backward it was necessary to use a negative forward pulse. The black lines appeared on the contact areas between the halfrods and V-grooves. The speed was around 0.05 - 0.07 mm·s^{-1}. The motion range was higher than 10 mm.

- **Fourth testing:** To resolve problems of the backward motion a new setup had to be found. Many different setups from the soft to rigid connection of halfrods with the z-wagon were tested. After these tests the speed was 0.05 mm·s^{-1}. The motion range decreased to 3 mm. A different starting position was tested but the wagon always stopped after 3 mm.

The setup of the system in each following testing step become more and more complicated. It can be explained by these reasons:

a) Sapphire halfrods cannot be fixed exactly parallel to each other. It can be adjusted by bolts in x, y plane, but there is no way how to correct this defect in the parallel x, z or y, z planes (see Fig. 4.8).

b) Due to impropriate design the setting of the system by bolts is very sensitive. A small change of the bolt position causes the big change of the force between the wagon and the halfrods.

c) All leaf springs are made of beryllium brass. This material becomes softer under plastic deformation. The leaf spring P is under high stress causing plastic deformation. It changes the spring force in each time when one makes a new adjustment of the system.

d) The roughness of the contact surface of wagons is R_a=0.4 [59]. It seems to be a higher value around R_a=1.6.

The second problem was a decrease of the speed during each testing. Probably, it coincides with black line which appeared at the contact areas of the sapphire halfrod and wagon V-groove. It can be caused an iron oxide created during the wagon motion. The friction ratio between iron oxide and sapphire is different from the initial state. The exact value of this parameter has not been found in literature.

The last problem was the stopping of the wagon. The reason for this behaviour has not been resolved yet. It is possible that the leaf spring become deformed permanently too. It might caused a slight bending of halfrods. This belly shape creates inhomogeneous force distribution and various contact area between halfrods and the wagon (see Fig. 4.9).

Results of all testings are summarized in Tab. 4.1.

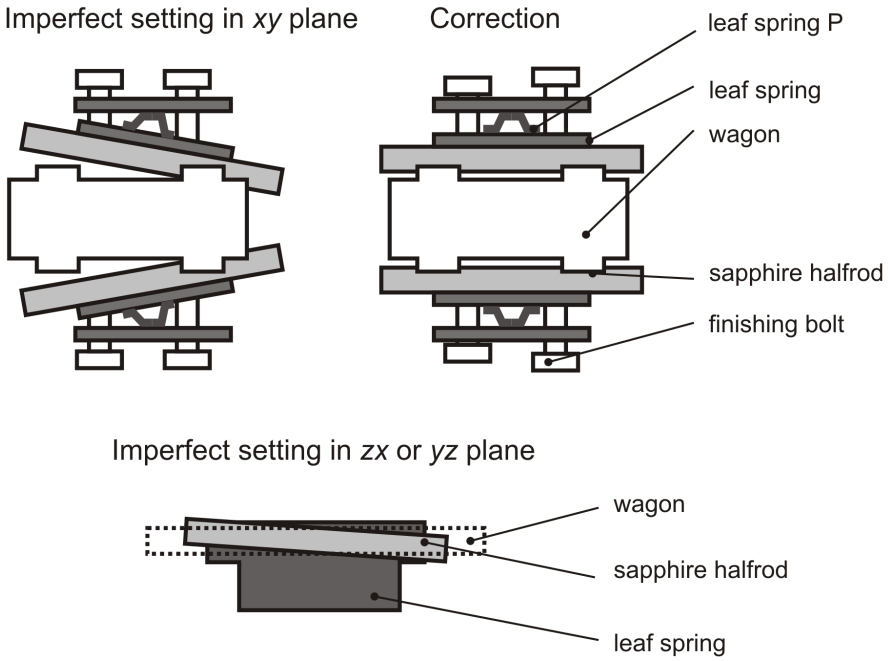

Fig. 4.8: Imperfections in halfrods alignment and its correction in x,y plane.

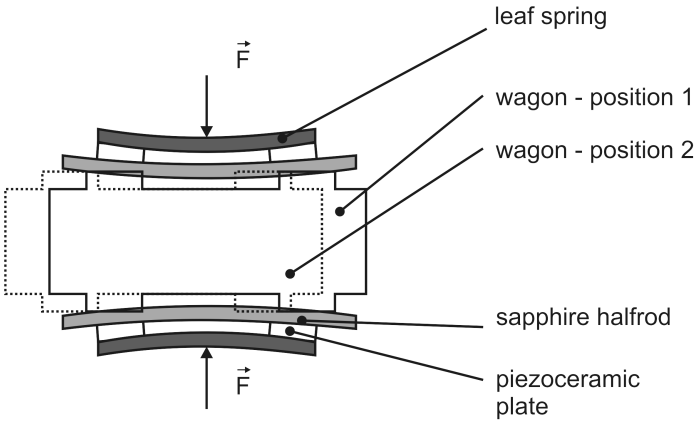

Fig. 4.9: Change of the contact area caused by deformation of the leaf spring.

Test	Speed [mm·s^{-1}]	Motion range [mm]	Load	Notice
1	0.25	>10	wagon z	easy setup
2	0.08 - 0.1	>10	full load	changed setup
3	0.05 - 0.07	>10	full load	black line on the contacts
4	0.05	<3	full load	jamming

Tab. 4.1: Summarization of Kalina´s motion system testing

Despite these problems the motion system works in principle. As bias driving pulse was used U_{f} (b=1) for the forward direction (see Fig. 4.10 b) and U_{b} (b=1) for backward direction (see Fig. 4.10 b). The shape of these pulses[1] can be expressed as

$$U_{\mathrm{f}}(t) = \begin{cases} \frac{e^{bt}-1}{\max(e^{bt})} & t \in \langle 0, 0.9\rangle, \\ 1 & t \in (0.9, 1\rangle, \end{cases} \tag{4.1}$$

[1]Pulses are normalized in both axes to one.

$$U_{\mathrm{b}}(t) = 1 - \frac{e^{bt} - 1}{\max(e^{bt})} \qquad t \in \langle 0, 1 \rangle, \tag{4.2}$$

where b is the coefficient of the pulse shape. It was found that the system worked with

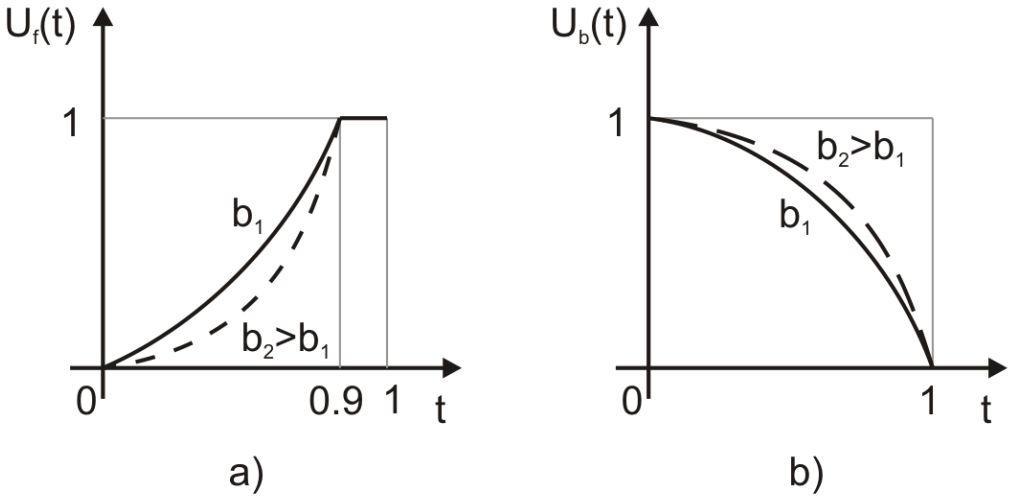

Fig. 4.10: Shape of a pulse: a) forward pulse U_{f} and b) backward pulse U_{b}.

a higher speed for the pulses with a higher value of b for the exponential function. An other shape of the pulse was investigated as well. The polynomial shape was tested with a general expression as

$$U_{\mathrm{pol,f}}(t) = \frac{t^c}{\max(t^c)} \qquad t \in \langle 0, 1 \rangle, \tag{4.3}$$

$$U_{\mathrm{pol,b}}(t) = 1 - \frac{t^c}{\max(t^c)} \qquad t \in \langle 0, 1 \rangle, \tag{4.4}$$

where c is the real constant.

The higher value of c causes higher speed of the motion again. This problem was investigated together with Jan Neuman, Zdeněk Nováček and Jiří Pavelec. It is described in detail in the bachelor thesis of Jiří Pavelec [63].

A new x, y, z motion system is based on the slip-stick principle too and it was inspired by Kleindiek´s motion system [58]. The setup is shown in Fig. 4.11. Piezoceramic plates are stuck between sapphire halfrods and the x-wagon or the y-wagon. Each wagon is connected to the V-groove which provides guiding and centering of the wagon. The angle of the V-groove is 90^o. The slip takes place between the V-groove and the sapphire halfrod. The force caused by the spring can be adjusted by two bolts to find the best setting of the system. Two bolts are proposed to compensate a fabrication inaccuracies or imparallelness of the halfrods. The scanner is integrated into the inner rod of the inchworm. The motion range of this system is 20 mm in *x,y* axes and 15 mm in z axis. The minimum step of the motion in each axis is in the order of nanometers.

The changes which are proposed to simplify a proper adjustment in Kalina´s system as follows:

a) A material with more suitable mechanical properties will be chosen for the leaf springs.

b) The leaf springs undergo an elastic deformation only.

c) Application of bolts with fine threads to make an easier adjustment of the acting force.

d) The surface of the V-grooves will be polished to the roughness R_a=0.1 or smaller and covered of a hard layer of DLC or TiN or modified by nitridation. It decreases the area of sticking contact between the V-groove and the halfrod.

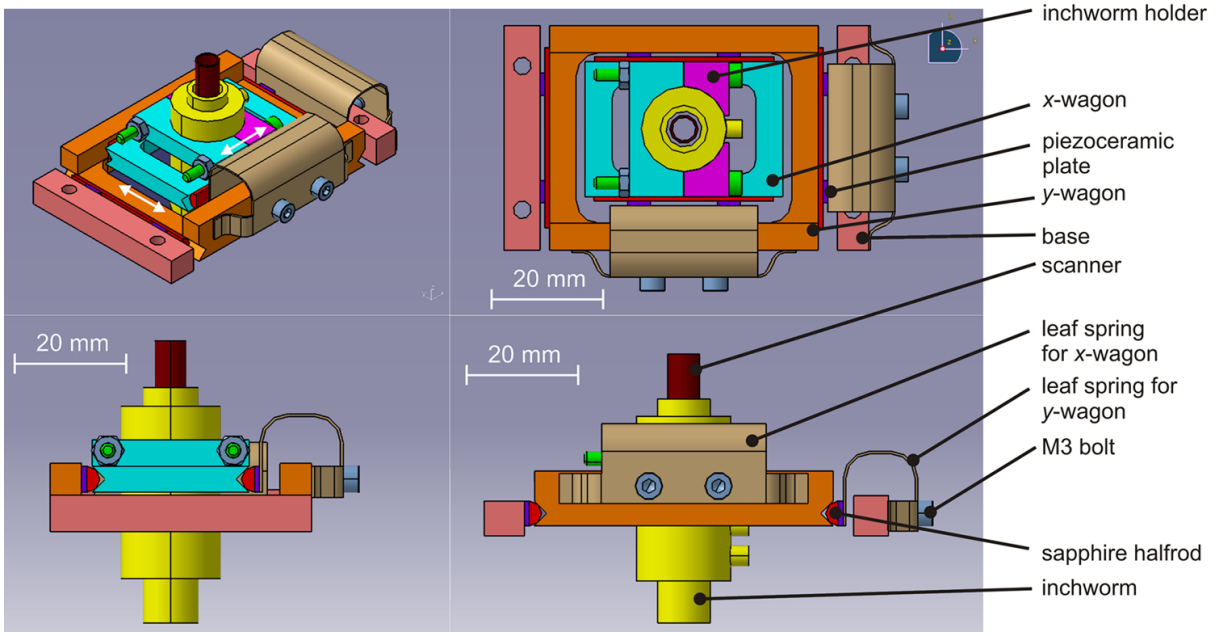

Fig. 4.11: Setup of a new x,y,z motion system.

The models and drawings of the x,y,z motion system are on CD enclosed in the diploma thesis.

This system has not been fabricated and tested yet.

4.2.4. Design of the rotational system of mirrors

No commercial system on mirror rotations met all requirements on stability, non-magnetism, beam deflection range (>2 °) and angle resolution (<4·10^{-6} °) has not been found yet.

Design I

A rotational system of mirrors utilizing the slip-stick principle has been designed.

The system setup is shown in Fig. 4.12. A x,y-disk with the V-groove is placed between three sapphire halfrods. This design guarantees the self-centering of the x,y-disk at any position. One of the sapphire halfrods is fixed on a leaf spring. The force setting is done by screws acting on this spring. Rotation in x,z is based on the same principle. The range of the rotation is not restricted and can rotate by 360° in both direction and an angle resolution is better than 1·10^{-6} °.

This system of the mirror motion is unique and it has not been published yet.

Design II

The idea of the second solution was proposed in an optical department of IPE (M. Liška). The schematic drawing is in Fig. 4.13. It uses a spherical mirror to convert a linear motion

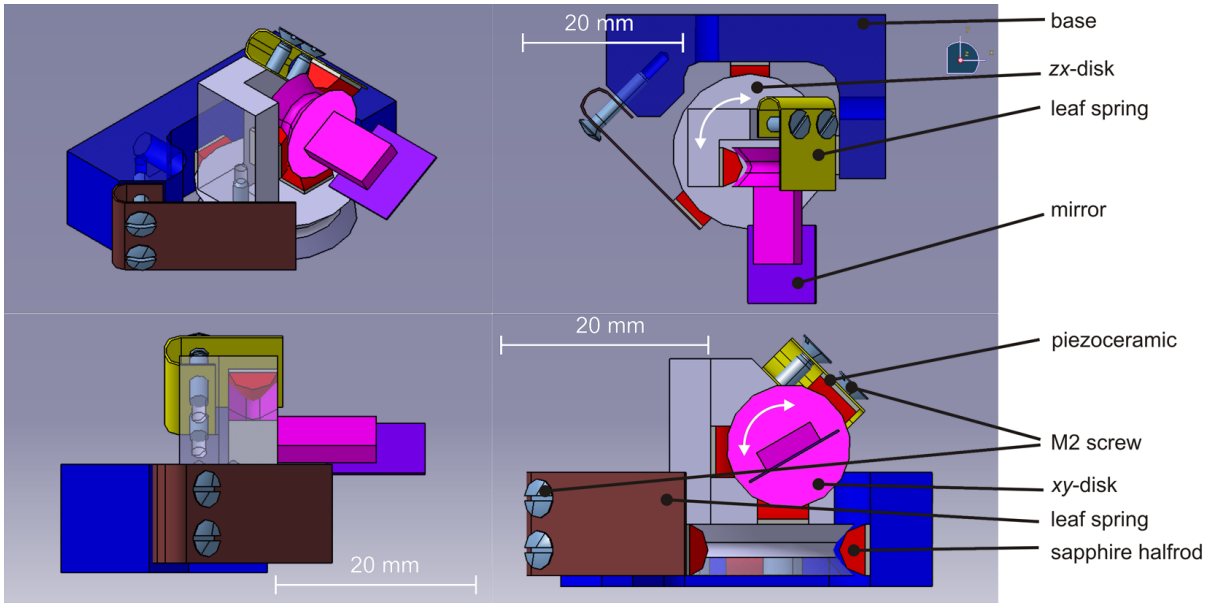

Fig. 4.12: Setup of a new mirror motion system.

to an angle deflection. The linear motion can be provided by a piezoscanner or another system.

Angle deflection φ in one axis can be calculated for a small angle ($\varphi < 5\,^{\circ}$) as

$$\varphi \doteq 2\frac{\Delta x}{r - \frac{\Delta x^2}{2r}}, \tag{4.5}$$

where Δx is the deflection in x axis and r is the radius of the mirror.

To meet our requirements for a beam deflection of at least $2\,^{\circ}$ the radius $r = 5,15\,\mathrm{mm}$ is demanded (Δx is supposed $90\,\mu\mathrm{m}$).

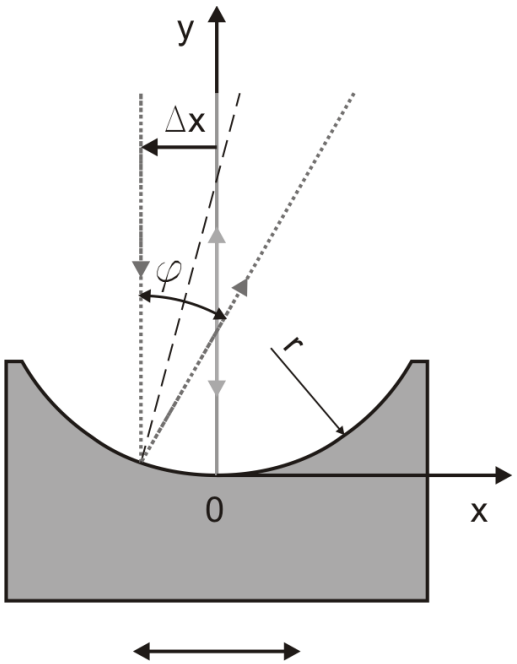

Fig. 4.13: Deflection system based on a spherical mirror.

4.2.5. Modification of the cantilever holder

To simplify an adjustment of the laser beam towards the cantilever reflection part and to decrease the angle range of the mirror motion system a new cantilever holder was required.

The final design of this component is shown in Fig. 4.14. The reproducible attachment to the same position of any cantilever is provided by a groove. As the size of the cantilever base is usually the same it defines the possible region of the cantilever reflective surface to $1 \times 1 \times 1\,\mathrm{mm}^3$ in the global microscope coordinates and to the rotation by $0.1^o \times 0.1^o$ of the mirror system. The leaf spring is used to fixed the cantilever in the right position.

A protection fork is designed to avoid an incidental collision of the cantilever with other parts of the AFM microscope.

An angle between the cantilever and its base is proposed to be 15^o to isolate the reflection from the cantilever and the sample[2].

This cantilever holder is designed for the contact mode and optical beam detection of the cantilever deflection. Small modification can be done to adjust it for piezorezistive or piezocapacitance detection system.

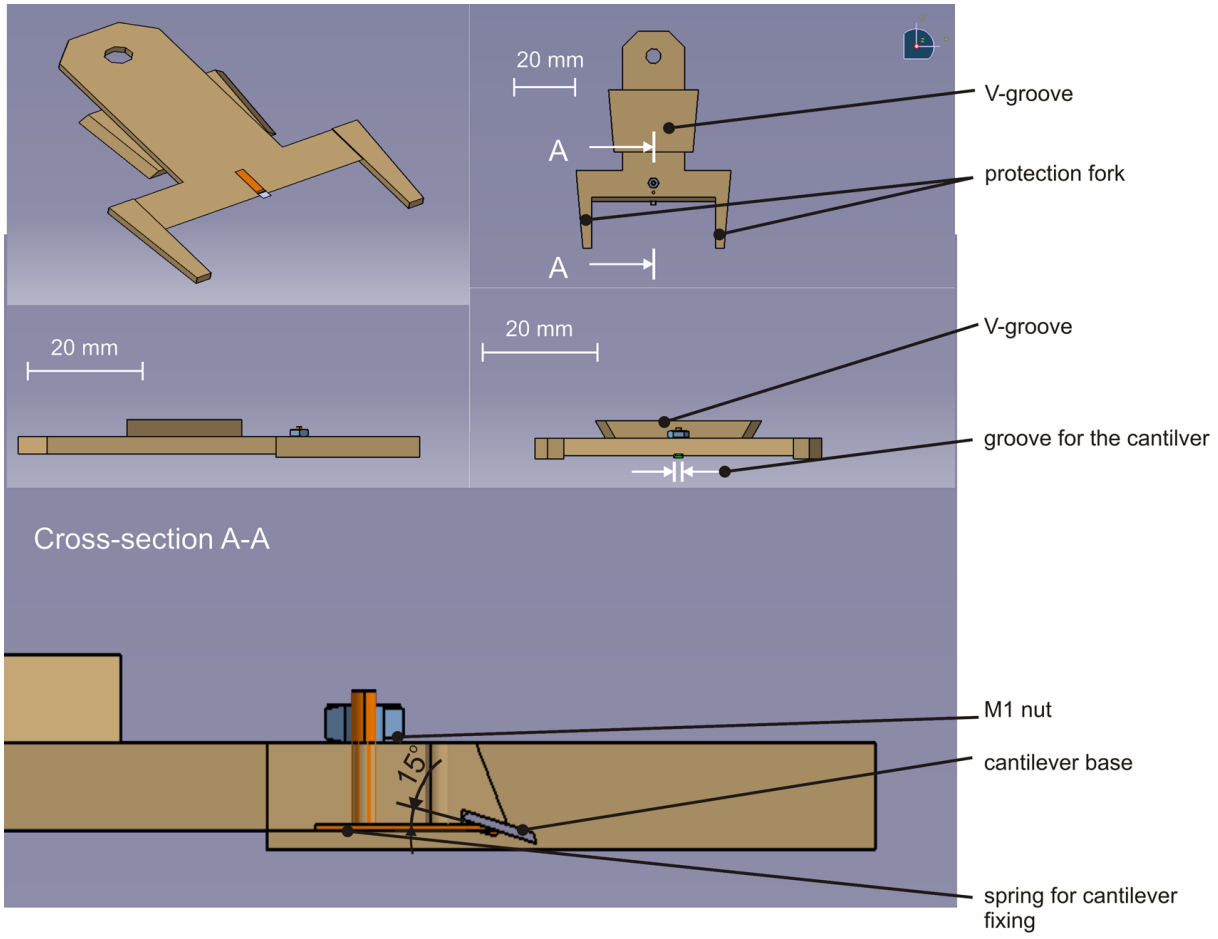

Fig. 4.14: Design of new cantilever holder.

[2]Tracking of the beam was done in program SIMOPS written by R. Kalousek (IPE)

4.2.6. Final design of the AFM microscope

The final modified design of AFM microscope is shown in Fig. 4.15 (for comparison see Fig. 4.2).

Other its modifications are as follows (see Fig. 4.15):

- Modification of back side of the AFM microscope to use one vacuum tweezer to install both the sample and cantilever from same the side.
- Modification of the top and bottom plate of the AFM microscope. The changes mentioned above led to a new design of top their design.

The models of all modified components are on the CD attached to the diploma thesis.

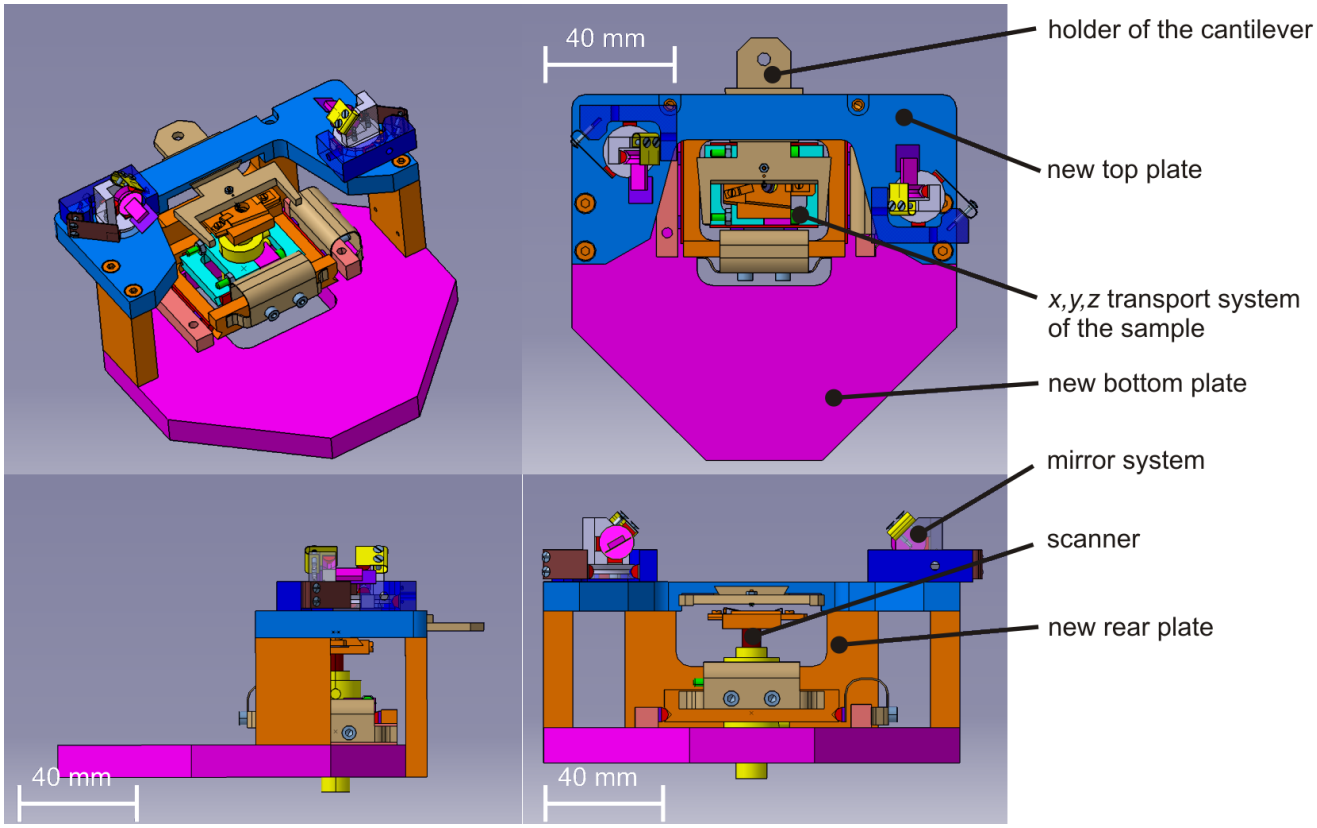

Fig. 4.15: Design of the modified AFM microscope.

4.2.7. Sticking with UHV compatible glue

Sticking with a UHV compatible glue is not difficult, nevertheless it is important to build some experience to achieve required results without overflow of the glue across the side parts of elements.

The sticking surface of each glued part has to be clear but does not need be perfectly smooth. We used a two-component UHV compatible conductive glue A-H27D from Lew-Vac (for details see [60]). It is mixed in ratio 10:1. This mixture is a slightly viscous liquid without any blobs.

Technique of sticking is as follows:

- The glue is applied on the sticking side of one part (see Fig. 4.16 a).
- This part wearing the glue is put on the sticking side of the second part and then it is pressed slightly to create a thin layer of the glue between both sticking elements (see Fig. 4.16 b).
- Both parts are taken apart and the glue is removed from one part by 2-isopropanol. Excessing glue on the second part is removed in the same way as in the previous case (see Fig. 4.16 c).
- Both parts are put together and heated up to 120 °C and annealed at the same temperature for 3 hours.

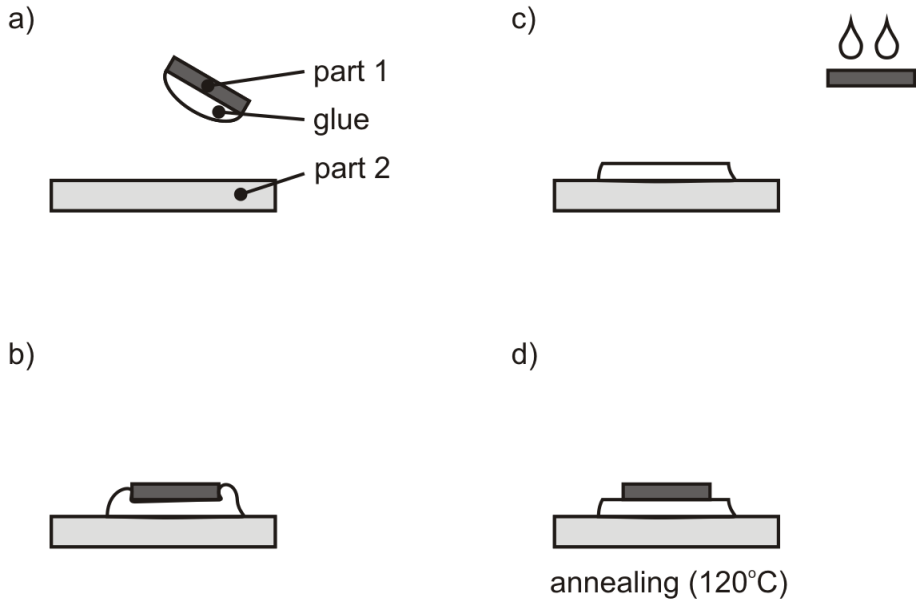

Fig. 4.16: Technique of sticking two parts with a UHV compatible glue: a) application of the glue on the sticking side, b) putting both parts into contact and creation of a thin layer of the glue, c) removing one part and cleaning by 2-isopropanol, d) putting together again and annealing.

It is important to mention that two parts stuck together by this technique is impossible to separate from each other nondestructively. It was tested to use the ultrasonic dissolving in acetone or in 2-isopropanol for one week without any success. But if the glue is not annealed correctly, it is possible to dissolve it.

4.3. Design of the UHV chamber of the combined AFM/SEM system

A new unique ultra high vacuum (UHV) chamber had to be designed to meet all requirements for the special combined AFM/SEM system equipped with microscopic and analytical techniques as AFM, SEM, SAM and EDX.

This UHV system has been called Sháněl-Šikola-Spousta Miscellaneous Atomic Resolution Research Apparatus (SSS - MARRA).

4.3.1. Setup

The chamber design consists of a tube and top monolith. It provides better mechanical properties with respect of SEM microscope stability. Non-magnetic stainless steel (17 246) compatible with UHV conditions was chosen for fabrication of the chamber. The whole system is shown in Fig. 4.17 and detail of the sample region and positions of detectors are depicted in Fig. 4.19 and Fig. 4.18 respectively.

As a SEM microscope the product of the Tescan, s.r.o. company (Mira) was used. It is mounted on the top of the chamber and oriented perpendicularly to the plane of the sample. Vacuum sealing between the SEM microscope and the chamber is provided according to the designed at Tescan, s.r.o. The work distance between SEM and the sample is 6.5 mm and higher. SEM can work with AFM simultaneously. To provide it, it was necessary to use special cantilever with a tip tilted towards the cantilever (see Fig. 4.20 and Fig. 4.21).

The AFM microscope designed by Vít Křenek [7] and modified the author of this diploma thesis was used. It is mounted on the x,y mircoscope positioning system. The z positioning is provided linear positioning system being driven from outside of the chamber through the bellows (see 4.3.3).

The chamber is evacuated by a system of vacuum pumps. This system consists of rotary, turbomolecular and ion vacuum pump. The rotary and turbomolecular pumps are connected to the flange A through a vacuum valve. They are used for evacuating of the load-lock chamber (see Fig. 4.17). The ion pump is connected to the flange B (see Fig. 4.17).

Sample and cantilever loading is done through a flange A (see Fig. 4.17). The cantilever and sample storage system have not been designed yet.

A secondary electron (SE) detector[3] is in direct sight the sample. It increases the amount of detected secondary electrons (see Fig. 4.17). A non-UHV detector version is shown. UHV modification of the SE detector has not been done yet.

An energy dissipation X-Ray (EDX) detector is mounted at an angle of 45° and in this way no other devices screen off X-ray from the sample to this detector (see Fig. 4.17).

A back scattered electron (BSE) detector is positioned in the way to optimize the intensity of the signal (see Fig. 4.17). BSE detector cannot work with AFM simultaneously because it screens off the laser beam. This problem can be solved by using piezorezistive or piezocapacity self-sensing cantilevers.

Installing the scanning Auger electron microscope (SAM) was the most complicated. Its position represents a compromise between the requirement on maximal signal, which depends on the distance between entrance lenses of SAM and the sample and the tilt

[3]It is detector used by Tescan, s.r.o.

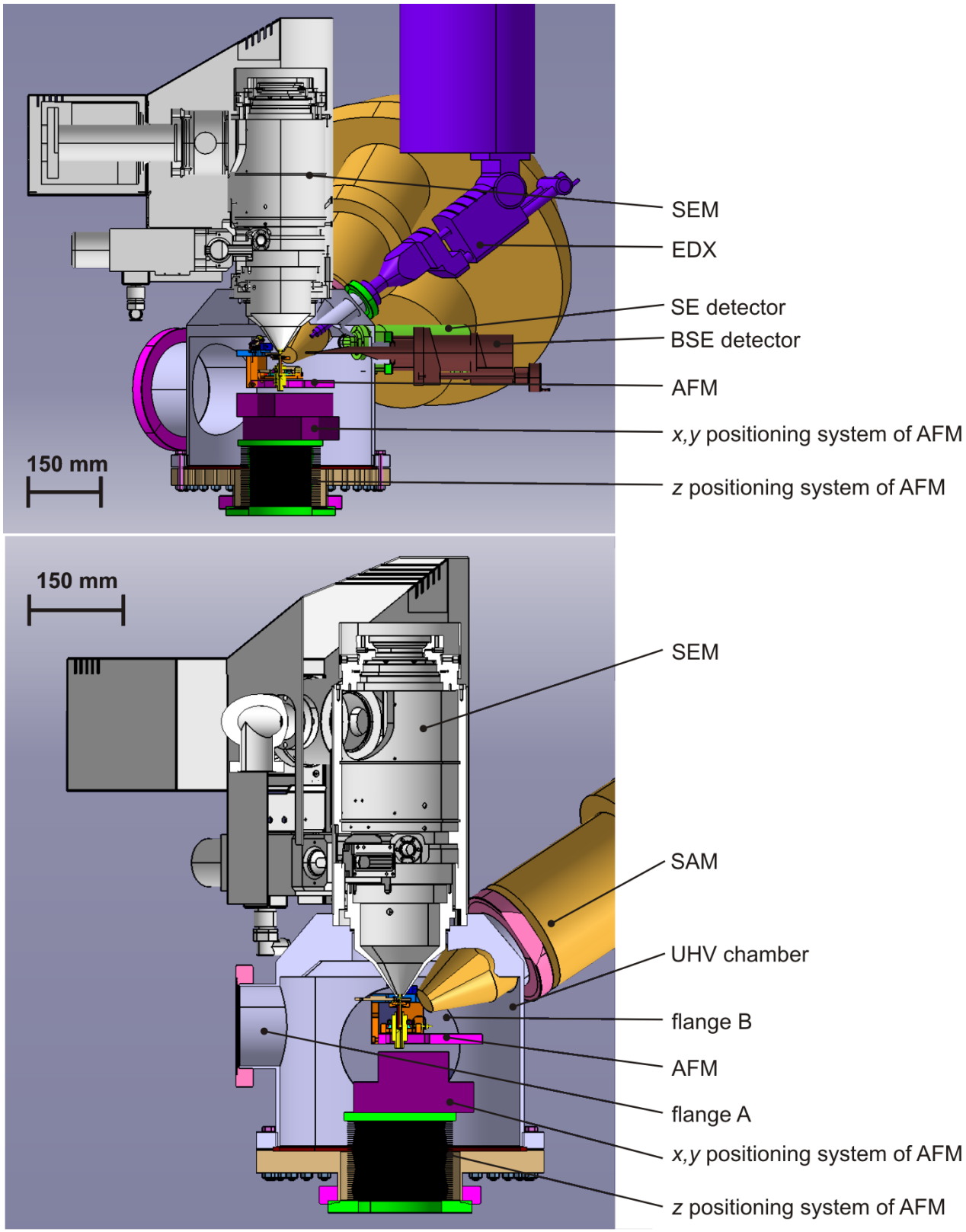

Fig. 4.17: Views of the AFM/SEM system SSS - MARRA.

of SAM towards the sample. Finally, the angle 31° and work distance 30 mm from the SAM objective and 26.5 mm from the SEM objective was chosen . In an ideal case it

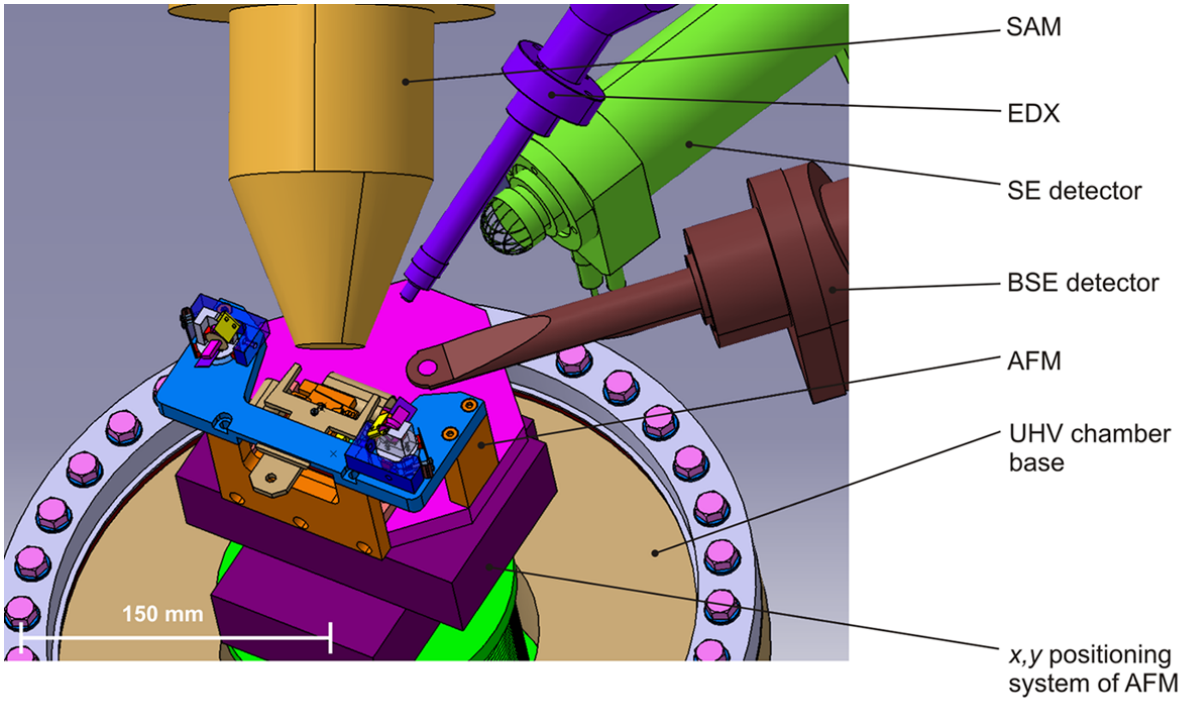

Fig. 4.18: A detail of detector positions of the AFM/SEM system SSS - MARRA.

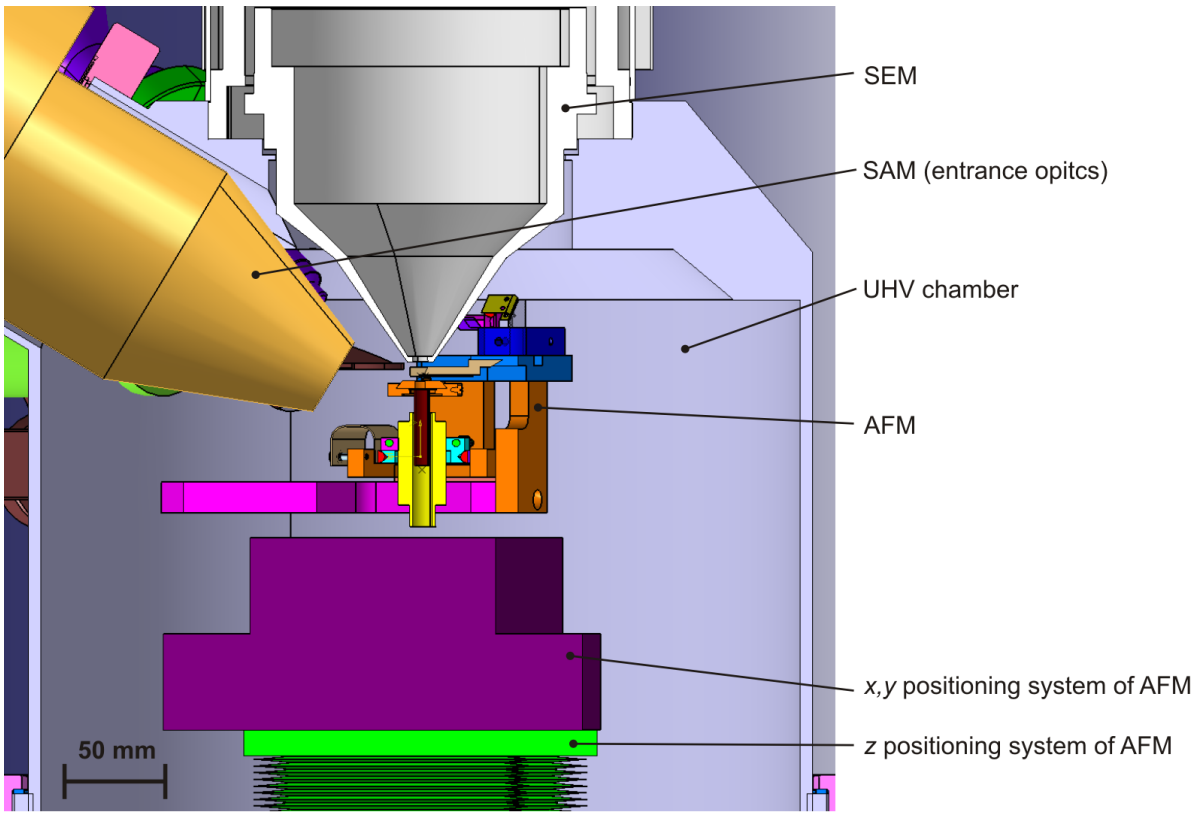

Fig. 4.19: A detail of the sample area of the AFM/SEM system SSS - MARRA.

provides the SAM measurements with resolution around 20 nm for energy of the electron beam in the range of 5-10 keV. This design was proposed for two possible SAM detectors: Phoibos 150 (Specs) and Sphera (Omicron).

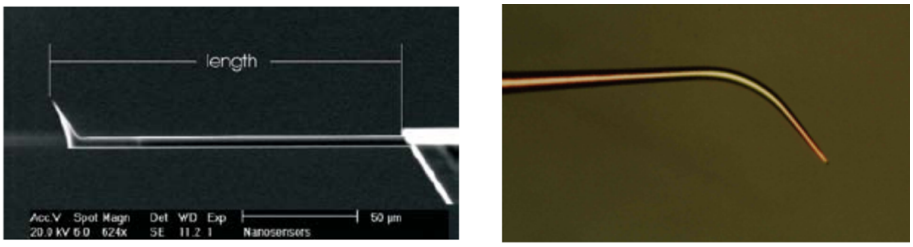

Fig. 4.20: Cantilever with a tilted tip a) [64], b) [65].

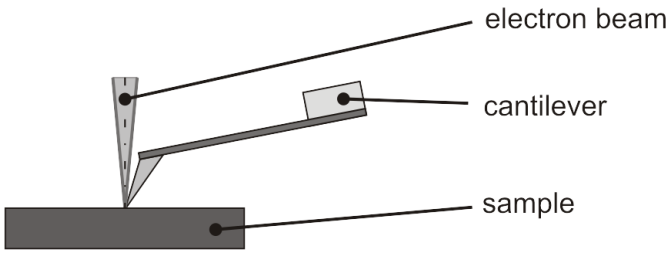

Fig. 4.21: Setup of the cantilever and electron beam in the simultaneous mode of AFM/SEM.

The main SSS-MARRA system parameters are summarized in Tab. 4.2 and the modes of this system are shown in Tab. 4.3.

The models of SSS-MARRA components are on the CD attached to the diploma thesis.

Parameters of SSS-MARRA	value
Material	17 042
Chamber inner diameter	300 mm
Chamber outer diameter	310 mm
Chamber height	293.5 mm
Work distance SEM/SE	5-50 mm
Work distance SEM/AES	26.5 mm
Slope of SAM to the sample	31°
Work distance SEM/BSE	5-50 mm
Work distance SEM/EDX	5-50 mm

Tab. 4.2: Parameters of SSS - MARRA

Mode	AFM	SE	BSE	SAM	EDX
AFM	x	x		x	x
SE	x	x			x
BSE			x		
SAM	x			x	x
EDX	x	x		x	x

Tab. 4.3: Working modes of SSS - MARRA.

4.3.2. Slope setup

An alternative design of SSS - MARRA was proposed. It was based on the tilt of the SEM microscope to 45°. The main advantages of this design was a better space assembly of all devices. On the other hand, the problem of focusing the electron beam at the sample arose. The setup is shown in Fig. 4.22.

This system in not optimal as the tilting the SEM microscope for working position is not recommended by the producer. The exact alignment of lenses is extremly difficult in comparison with the vertical system. Hence, the next work on this design was stopped.

The models of slope setup are on the CD attached to the diploma thesis.

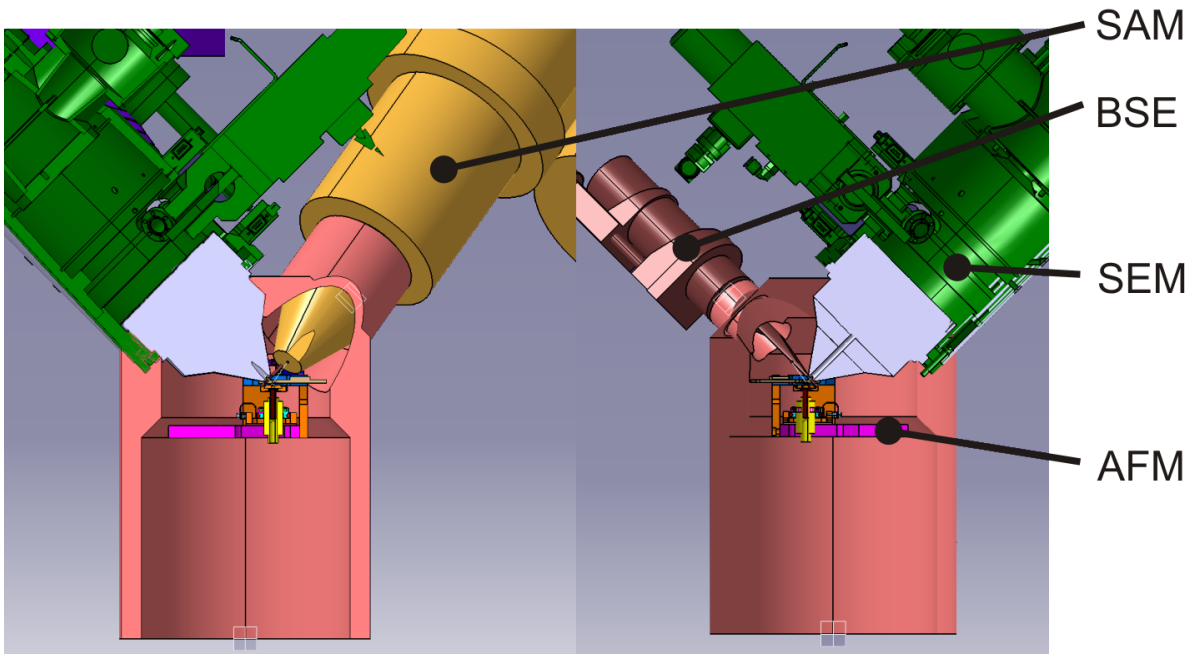

Fig. 4.22: Slope design of SSS - MARRA apparatus.

4.3.3. Requirements on the motion system of the AFM microscope

Initially, SSS-MARRA was designed to enable a simultaneous work of various detectors and techniques. But for optimal operation of the system it is necessary to provide separate application of the techniques.

From this reason it was needful to provide the positioning of the sample when SEM works alone. It was proposed to move the AFM microscope in x,y,z axes. It can be used for coarse positioning in SEM and for changing the sample or the cantilever when the AFM microscope is dropped down to the loading position.

Requirements posed on this coarse positioning are as follows:

- x,y,z - motion bigger than 40 mm,
- precision in microns,
- minimal load > 3 kg,
- speed higher than 1 mm·s^{-1},

- bakeable to 120 °C,
- UHV compatibility (pressure bellow than 10^{-7} Pa).

A commercial motion system which passed all previous requirements has not been found yet. Only one motion system almost meets all needs: AI-HR4-10000E-XY produced by AlioIndustries [62]. Its only limitation are storage and work temperature which lies in the range from -20 °C to 70 °C. It is not enough for baking an UHV system because reaching the required pressures can take two or three weeks instead of 2 - 3 days when being baked at 120 °C.

A new positioning x,y system has to be designed. It has been under development now.

The solution of z axes motion is based on a linear stage suited by bellows. An exact type of the linear stage has not been chosen yet.

4.3.4. Sealing of the UHV chamber

Sealing of the system is based on copper rings via conflat system except the sealing of SEM. It has to be designed in another way to avoid deterioration of magnetic material properties of the SEM objective. This solution is under development with Tescan, s.r.o.

4.3.5. Damping system of the AFM/SEM setup

The requirement on the best resolution of the microscopic techniques put requirements for the perfect damping system. The design of SSS-MARRA was proposed with respect to as big rigidity of the system as possible to avoid mutual vibration between each parts of this system.

The whole system will be placed on a special table with an active electromagnetic and pneumatic damping system.

Chapter 5

Organic solar cells

5.1. Introduction

Organic semiconductor devices are promising candidates for a photovoltaic applications [27]. Necessity of alternative sources of energy and their mechanical properties make them very interesting point of investigation. During the last two decades their properites have been investigated in many studies [28-33,74].

In this project we have mainly focused on charge transport processes in organic devices. For this purpose the organic solar cell has been used as a model device. The blend of MDMO-PPV (poly[2-methoxy-5-(3´,7´-dimethyloctyloxy)-1,4-phenylenevinylene]) and PCBM (methano-fullerene[6,6]-phenyl C_{61}-byturic acid methyl ester) has been used as the active layer. A spacer layer (Al_2O_3 or Ti_2O) between the active layer and the bottom electrode has been used for this study. The first aim of this project is the explanation the shift in the contact potential difference (CPD) of the electron acceptor and donor phase in the same direction in the polymer/fullerene blends organic solar cells after and during illumination [74]. The second aim is to explain the origin of the "second bump" in the photocurrent in the polymer/fullerene blends organic solar cells [29,33].

This part of diploma thesis was done at University of Technology in Eindhoven during Erasmus/Socrates studying exchange program in 2007 in group of prof. R. A. .J. Janssen.

5.2. Polymer/fullerene blends organic solar cells

5.2.1. Introduction

A solar cell (SC) is a device which is used for converting light energy into electric energy. The first observation of photovoltaic effect was done by French physicist Alexandre-Edmond Becquerel in 1839 [28]. Tang used the first heterojunction photovoltaic organic devices in 1979. Sariciftci made the first polymer/C_{60} heterojunction in 1994. Yu used the first polymer/polymer heterojunction in 1995 [28,35].

Nowadays SCs have many applications as power sources: solar plants, satellites, calculators, water pumps, etc. [35].

Organic SCs are mechanical and chromatical flexible. Their production is more ecological than inorganic SCs. The processing cost and requirement are low. These properties make from them a very good candidate for many applications [36,37].

5.2.2. Differences between organic and inorganic SCs

Nowadays most of the inorganic SCs are based on (crystalline) silicon.

In a 3D silicon lattice the interaction between low unoccupied molecular orbitals (LUMO) and high occupied molecular orbitals (HOMO) is very strong and leads to formation of valence and conduction bands [28].

In the organic SCs the LUMO and HOMO of compounds do not interact so strongly. Valence and conduction band are not created. The charges are transporting by hopping into localized states. The dielectric constant and mobility of free charges is lower than in inorganic SCs. Binding energy of the exciton is more lower than energy of the thermal movement $E_\mathrm{b} \ll kT$, exciton diffusion length is only around 10 nm and so charge separation is more difficult [28]. The bulk heterojunction is used to decreased the distance from point of an exction creation to the interface between compounds of an active layer (AL).

5.2.3. The principle

The basic principle of organic and inorganic SCs is same. Photons are absorbed in an active layer (AL) and create excitons. Electric field is necessary for charge dissociation compared to an silicon inorganic solar cells where $E_\mathrm{b} < kT$ and no field is needed for dissociation). The free charges are collected with the electrodes.

In this work the SC based on the MDMO - PPV/PCBM AL is used (see Fig. 5.1). The AL is sandwiched between two electrodes (see Fig. 5.2). The first electrode is semi-transparent. Indium - thin oxide (ITO) was used in this project, but other high-work function metals can be used [28]. The second electrode is a low work function metal. Aluminium was used during all experiments. PEDOT:PSS is deposited on the ITO and LiF is deposited on aluminium to improved the properties of the SC.

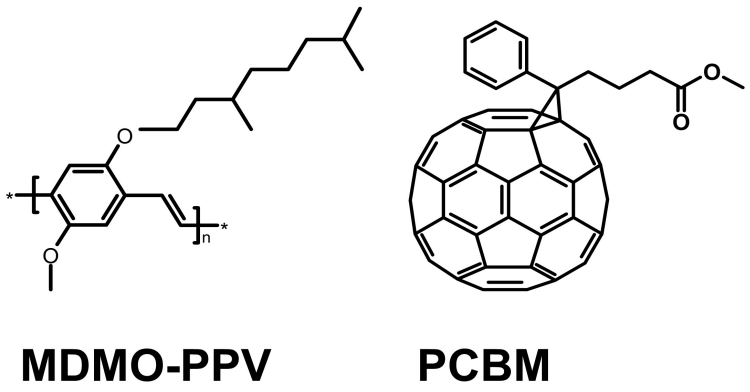

Fig. 5.1: The formula of MDMO - PPV and PCBM.

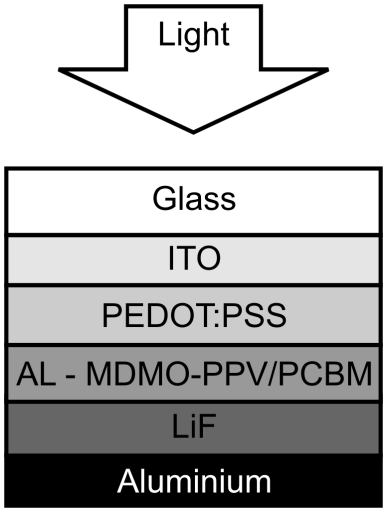

Fig. 5.2: The set up of SCs that is used in this project.

The principle of this SC is following:

- The light is absorbed in the AL and an exciton is created (see Fig. 5.3 b).
- The exciton has to be transported to the interface between the MDMO - PPV (electron donor) and the PCBM (electron acceptor,see Fig. 5.3 c) to separate into electron and hole (see Fig. 5.3 d).
- The built-in field causes that the electron is transported to the aluminium electrode and the hole to the ITO electrode (see Fig. 5.3 e) where they are collected (see Fig. 5.3 f).

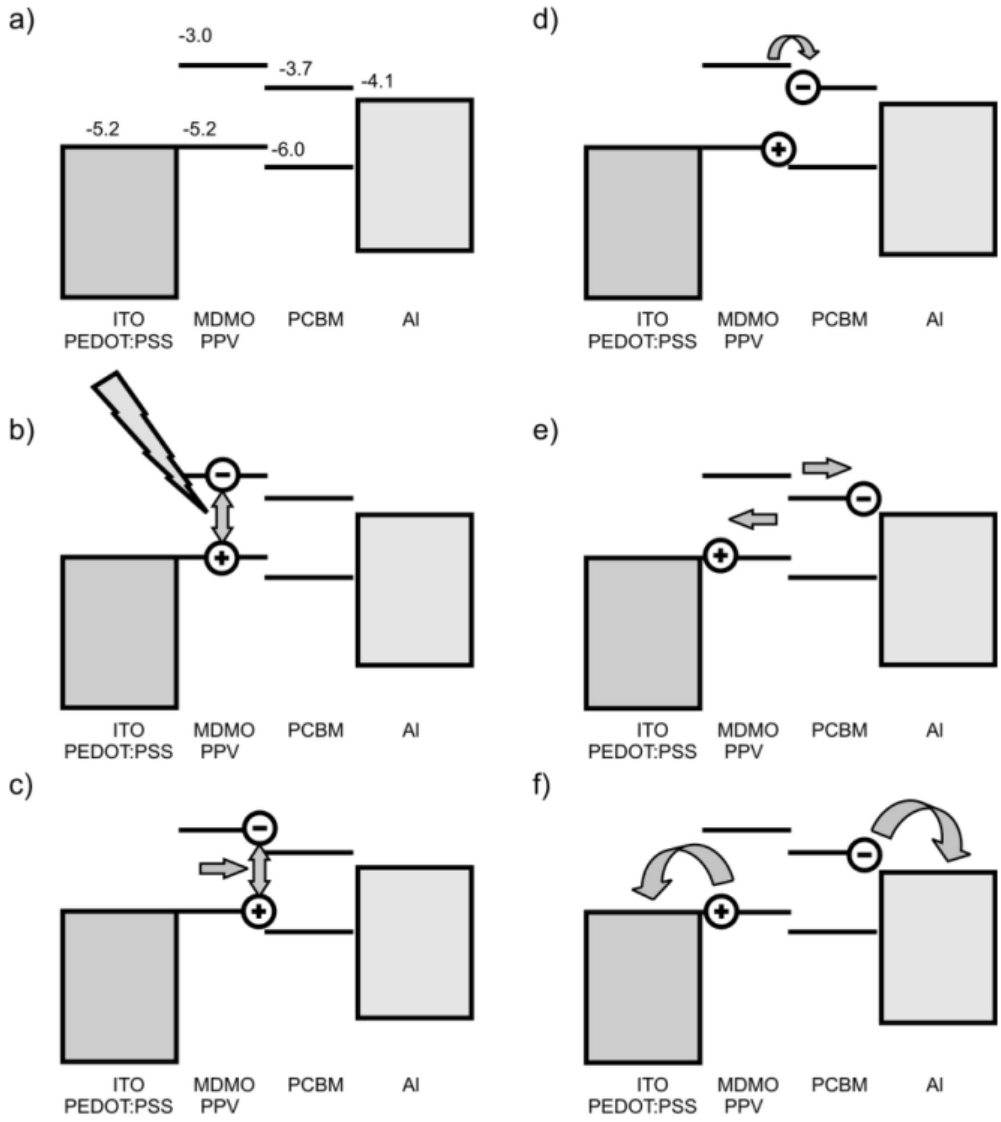

Fig. 5.3: The principle of MDMO - PPV/PCBM SCs: a) initial state, b) absorbtion of a photon and creation of an exciton c) transport of the exciton to the interface, d) charge separation, e) transport of charges to the electrodes, f) collection of charges on the electrodes.

5.2.4. Types of organic SCs

Nowadays several types of the active layer are used, for example: dye, conjugated polymer, blend polymer/fullerene [28].

The first organic SCs were prepared with a solar active compound between two electrodes (see Fig. 5.4 a)). In 1979 Tang used two different semiconductors. Their heterojunction increased the charge separation [38]. The design of the SC was bilayer (see Fig. 5.4 b)). The next increasing of charge separation was reached using a bulk heterojunction (see Fig. 5.4 c)) in 1994 [39].

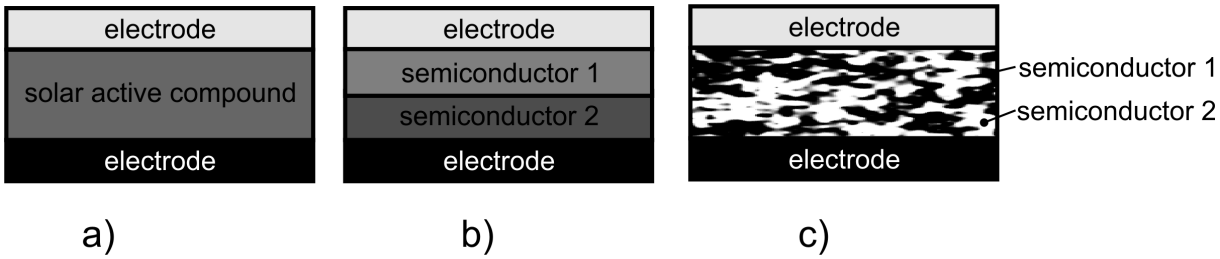

Fig. 5.4: Types of setups SC: a) single layer, b) bilayer, c) bulk active layer.

5.2.5. Characteristics of the SC

The SC is described by the following characteristics [28]:

- I_{D} is the current which is measured without illumination (see Fig. 5.5),
- I_{L} is the current which is measured during illumination (see Fig. 5.5),
- I_{PH} is the photocurrent, which is defined as (see Fig. 5.5):

$$I_{\mathrm{PH}} = I_{\mathrm{L}} - I_{\mathrm{D}}, \tag{5.1}$$

- I_{SC} is the short-circuit current, which runs through the cell without an external bias during illumination (see Fig. 5.5),
- I_{MAX} is the current when the power of SC is maximum (see Fig. 5.5):

$$I_{\mathrm{MAX}} \cdot V_{\mathrm{MAX}} = max, \tag{5.2}$$

- V_{OC} is the open circuit bias ($I_{\mathrm{L}} = 0$) (see Fig. 5.5),
- V_0 is the compensation bias, when photocurrent $I_{\mathrm{PH}} = 0$ (see Fig. 5.5),
- V_{MAX} is the bias voltage when the power of solar is maximum (see equation 5.2 and Fig. 5.5),
- **Fill factor** FF is defined as:

$$FF = \frac{I_{\mathrm{MAX}} \cdot V_{\mathrm{MAX}}}{I_{\mathrm{SC}} \cdot V_{\mathrm{OC}}}, \tag{5.3}$$

- **The quantum efficiency** QE is the number of generated electron per absorbed photon,
- **The power conversion efficiency** PCE is the power of SC divided by the power of the illuminated light P_{L}:

$$PCE = \frac{I_{\mathrm{MAX}} \cdot V_{\mathrm{MAX}}}{P_{\mathrm{L}}}. \tag{5.4}$$

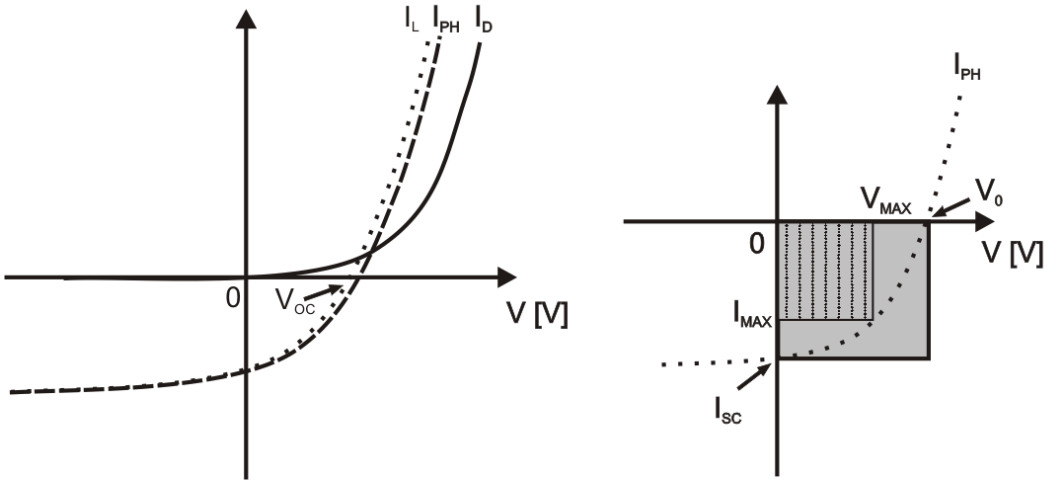

Fig. 5.5: The I-V characteristics of the SC.

5.2.6. Preparation

Preparation of SCs for our study is as follows:

1. **Preparation of the solution**: 3 mg/ml solution of MDMO - PPV in chlorobenzene mixed at least for 12 hours, at most for 48 hours at 50°C (protected against light with aluminium foil).

2. **Cleaning substrates**: mechanical cleaning with a soap solution, 20 min of ultrasonic cleaning in the soap solution, 30 min of washing process in water, 20 min ultrasonic cleaning in 2-propanol, drying with N_2, 30 min of UV-zone cleaning.

- **Finishing of the solution**: 12 mg PCBM mixed with the MDMO - PPV solution, (30 min at 50°C).

- **Preparation of the AL**: Spin-coating of PEDOT:PSS (1500 rpm for 60 s, 3500 rpm for 60 s, conductive polymer) and spin-coating of MDMO - PPV/PCBM solution (1500 rpm for 60 s).

- **Finishing the SC**: Deposition of LiF with thickness 1 nm and Al in 100 nm thick is done under vacuum (10^{-5} mbar). The first 20 nm of Al layer is deposited slowly to avoid a damage of the LiF.

5.2.7. Spacer layer

In order to block carrier transfer from the AL to the ITO electrode and avoid exciton dissociation on the ITO electrode, the spacer layer is used in this project.

The preparation of the sample does not differ too much from the preparation of the organic SCs described in the previous paragraph. Instead of PEDOT:PSS a spacer layer is deposited by plasma deposition under ultra high vacuum on the ITO, which was cleaned in the way described before. The final set up of the solar cell with a spacer layer (SL) is in Fig. 5.6. Al_2O_3 and TiO_2 are used as a SL in this work. The energy level scheme of SLs is in Fig. 5.7.

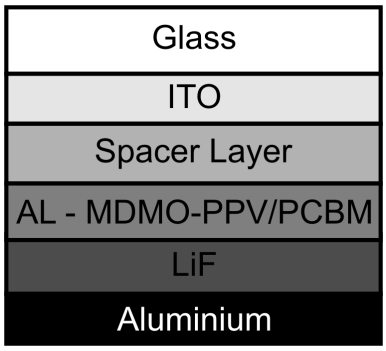

Fig. 5.6: The SC with a SL.

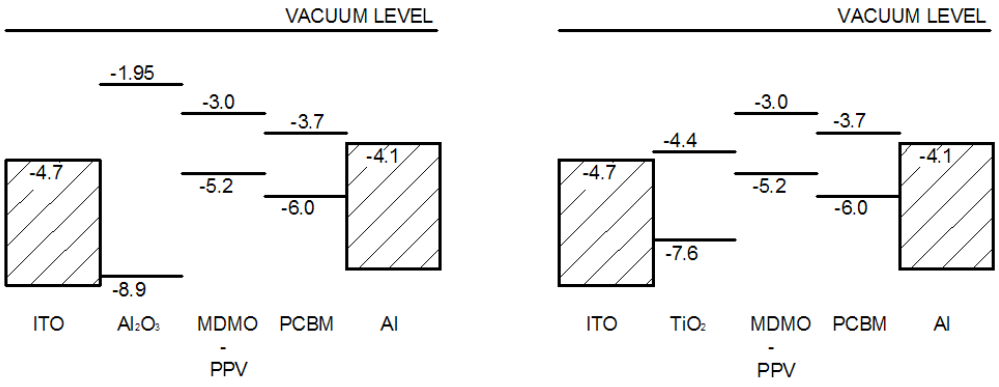

Fig. 5.7: Energy level diagram of the SC with Al_2O_3 [43] and TiO_2 [40] as a SL.

Chapter 6

I-V measurement of organic solar cells

6.1. Introduction

The properties of MDMO - PPV/PCBM blend were investigated in many studies [30, 32, 74]. The charge transport was numerically modeled in a good agreement with experimental data [29]. This model is based on the drift-diffusion approximation, Onsager theory, distribution function of donor-acceptor, etc. (for more see [29]). Another model for calculation of the photocurrent is used in this project. The model is much simpler. It is only based on the drift-diffusion approximation. It describes the photocurrent at low voltages very well (from -2 V to 0 V). However, the "second bump" which appears in the higher negative voltage (< -2 V), is not described with this model [33](see Fig. 6.1). The first [h]

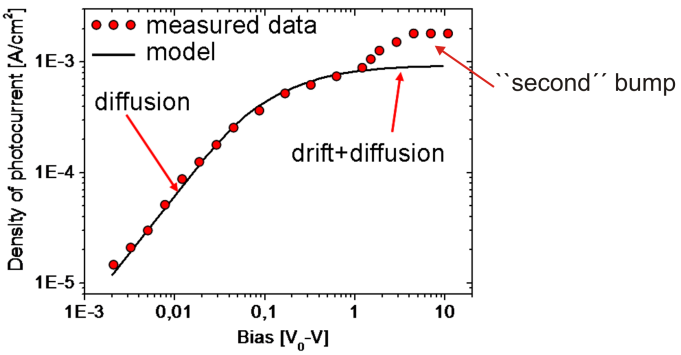

Fig. 6.1: The photocurrent of the organic SC and the calculation model [33].

aim of this project is to focus on the investigation of the origin of the "second bump" for the next improvement of the calculated model. The origin of this "second bump" is explained by the field dependance exciton dissociation [29] or it can be caused with exciton dissociation on the AL/ITO interface. For this investigation SL is used to block the charge injection into ITO electrode from AL.

Silicon monoxide was used as a SL for investigation of the charge transport in the PPV-ether. It was used as a tool for separation intrinsic and extrinsic source of optical charge-carrier generation [32].

6.2. Experiment

All samples were prepared in the way described in the subsection 5.2.6. The Keithley 2410 sourcemeter (0.012 % basic accuracy with 5-1/2 - digit resolution) was used for the measurement of current-voltage (I-V) characteristics, the white halogen lamp with the light filter (from 385 nm to 720 nm) was used for illumination. All measurements were performed in a nitrogen atmosphere (less than 1 ppm of H_2O and 1 ppm of O_2) to avoid oxidation of the AL. An area of ITO electrode was 0.071 cm^2

In the text the following marking is used:

- **DARK0**: is the current density J_D measured before any illumination,
- **DARK1**: is the current density J_D measured after the first illumination,
- **DARK2**: is the current density J_D measured after the second illumination
- **LIGHT1**: is the current density J_L measured under the first illumination,
- **LIGHT2**: is the current density J_L measured under the second illumination.

The first samples were prepared with 1 nm of SL. One sample was prepared without any SL and with the PEDOT:PSS for comparison. The I-V characteristic of SC without any SL is in Fig. 6.2. The high value of the J_D close to the J_L indicates to a present leakage current. These experiments were repeated and similar results were obtained. The photocurrent J_{PH} cannot be determined correctly from these data.

From this reason it was decided to scan the ITO with AFM to determine real topography. In Fig. 6.3 the topography of ITO is shown. The RMS roughness is around 10 - 15 nm. At the apex of spikes a very strong electric field is created at high negative voltage (< -2 V). This field can damage the AL. The second reason of the high leakage current can be short circuit between the bottom and upper electrode (see Fig. 6.4).

Samples with a thicker AL were prepared to avoid the high leakage current. The thicker layer was prepared by using a lower spin-coating speed. The dependence of thickness on the spin-coating rotation speed (rpm - revolutions per minute) is in Tab. 6.1. I-V characteristics with different thicknesses of AL are in Fig. 6.5 - 6.7. For next measurement the thickness of 175 nm has been chosen for which the leakage current and the noise were at the lowest values from those thicknesses without inhomogeneities in the AL caused the low speed of the spin-coating.

Spin-coating [rpm]	Averaged thickness [nm]
1500	75
700	110
400	175

Tab. 6.1: Dependance of the thickness of AL on the rpm of spin-coating

In the following experiments we prepared SCs with a thickness of 175 nm of AL.

Samples with the thickness 0.5 nm and 1.5 nm of the TiO_2 and without the SL were measured. Their I-V characteristics are in Fig. 6.8 - 6.10 and in Tab. 6.2. The photocurrent densities from SCs with 0.5 nm and 1.5 nm of TiO_2 SL and without any SL are in Fig. 6.11. The noise was observed at high negative voltages (< -3 V). The calculation of the photocurrent was done according to 33.

The I-V characteristics of the samples with Al_2O_3 SL are in Fig. 6.12 - 6.15 and in Tab. 6.2. It is obvious that I-V characteristics of these samples are not similar to I-V characteristics of the SC and that the high level of the noise is present. The SCs with Al_2O_3 thickness higher than 1.5 nm cannot be used for this study.

Because of the presence of high level noise at high negative voltages (< -2 V), being caused by the leakage current, it cannot determine the result photocurrent in the region of our interest. Using the thicker layer (175 nm) the noise level decreased due to the lower leakage current, but not sufficiently.

It was decided to polish the ITO to remove the sharp spikes. A classical rubber for pencil (Koh-i-noor with an elephant) was used for this polishing for 5 minutes (high pressure was applied). The sharp spikes were removed and the resultant RMS roughness was around 3 - 5 nm (see Fig. 6.16).

The samples were prepared without any SL to distinguish the influence of polishing the ITO on the noise at the high voltage (< -2 V). The SC with no PEDOT:PSS and 175 nm thick AL, with PEDOT:PSS and 175 nm thick AL were prepared for the comparison. The photocurrents of SCs with the polished ITO are shown in Fig. 6.17. The noise and the leakage current was minimal.

The next set of the experiments with the SL was performed on the samples with the polished ITO. The I-V characteristics of these samples are shown in Fig. 6.18 and Fig. 6.19 and in Tab. 6.2. The samples with 3 and 4 nm thick Al_2O_3 have not revealed the properties of SC. The photocurrents were determined from I-V characteristics of SCs with 1 nm of Al_2O_3 and without any SL are in Fig 6.20.

Samples with 1 nm thick Al_2O_3, AL (75 nm) and with the polished ITO were measured. The I-V characteristics are shown in Fig. 6.21 and in Tab. 6.2. The photocurrents are shown in Fig. 6.22. The high leakage current appears below -2 V (see Fig. 6.21) and occurs in the region of our interest. The leakage current is very low in the region from -2 V to $+2$ V and then it grows very fast to a stable value. This behaviour of Al_2O_3 is investigated in [41, 42].

6.3. Summary

The leakage current was present in our I-V bulk measurements. This problem was solved by using a thicker layer (175 nm) of the AL and polishing of the ITO.

SCs without any SL having very good reproducibility of SC characteristics were prepared. The "second bump" begins around 1 V (see Fig. 6.17,6.20,6.22).

The SC with TiO_2 SL was prepared only with the unpolished ITO. TiO_2 changes the SC characteristics slightly. The "second bump" is present. The next experiments could not performed due to end of TiO_2 deposition at the Technical University in Eidhoven.

Al_2O_3 SLs strongly influence the properties of SCs. The SC with Al_2O_3 SL thicker than 1 nm has no SC behaviour and works in ohmic regime. Another problem of Al_2O_3 films was changing the properties of Al_2O_3. The high leakage current is present under -2 V. A "second bump" was observed for a sample with 1 nm Al_2O_3 SL, but its origin is not clear (see Fig. 6.22).

The higher growing up of the photocurrent on the sample without any SL in Fig. 6.20 and Fig. 6.22 can be caused the reaching of break-down voltage of ITO.

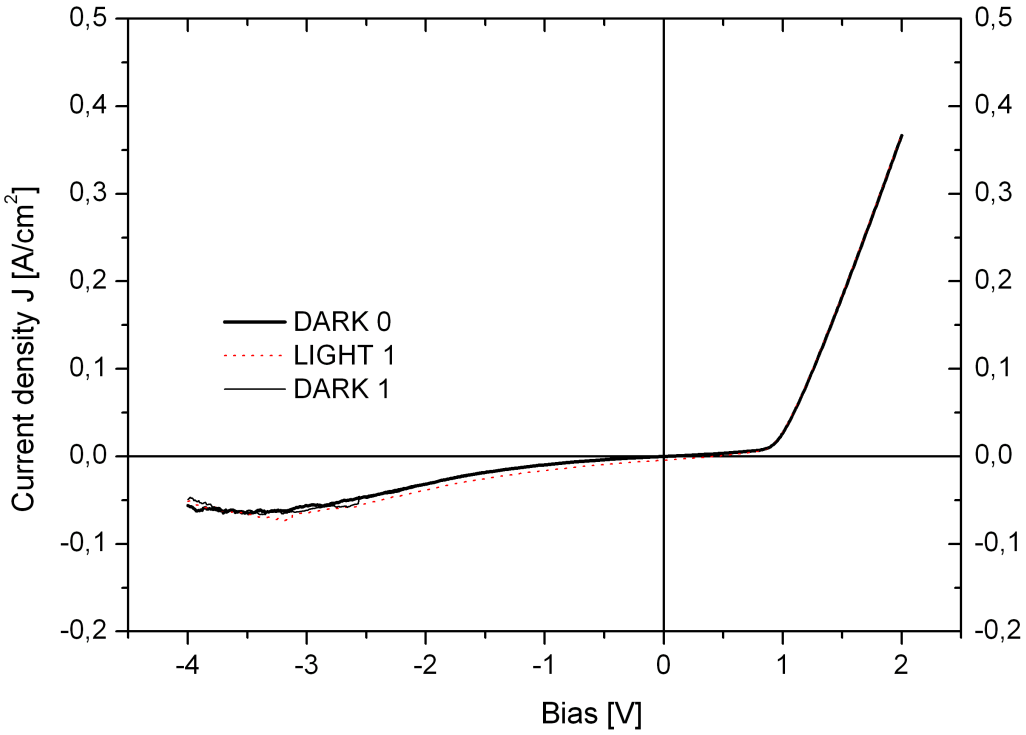

Fig. 6.2: I-V characteristics of the solar cell without any spacer layer - the leakage current (glass/ITO/AL(75 nm)/LiF/Al)

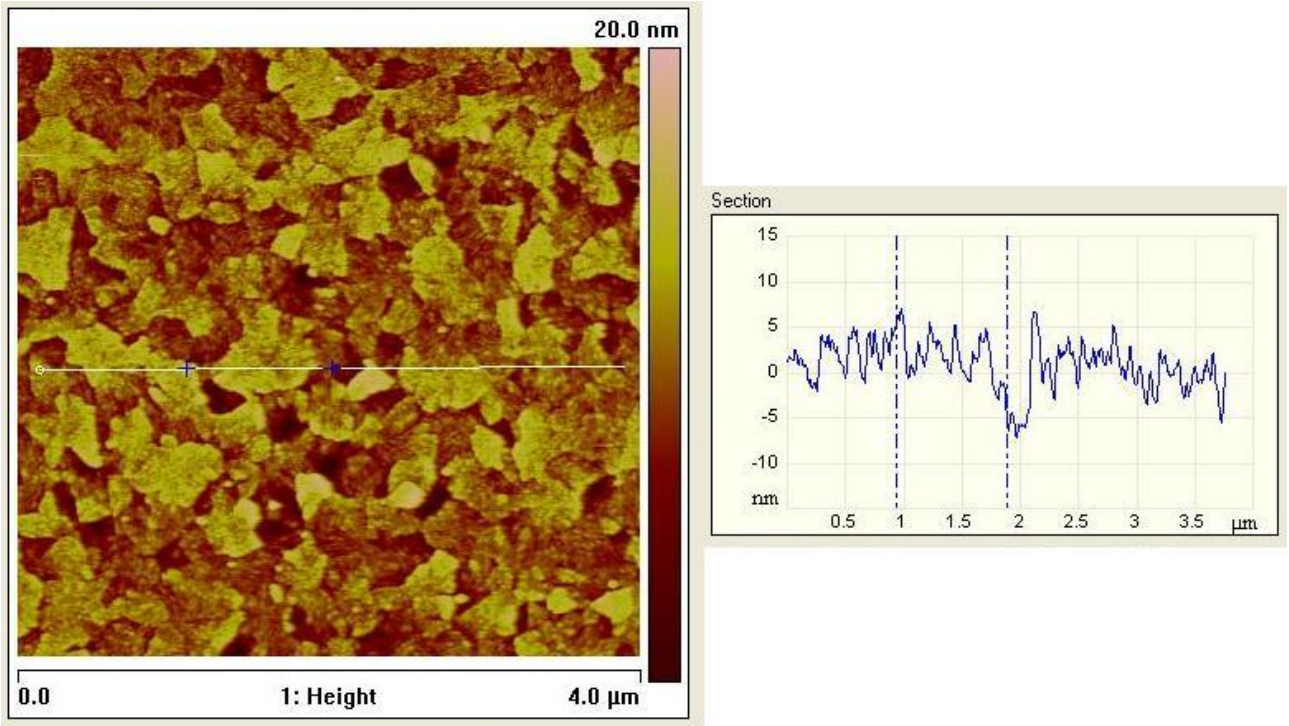

Fig. 6.3: AFM image ($4 \times 4\,\mu m^2$) left: topography, right: cross-section of the ITO

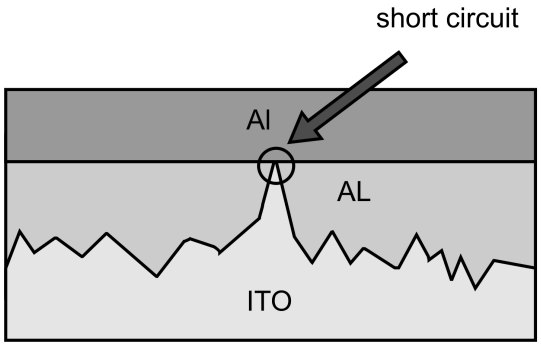

Fig. 6.4: Short circuit in the solar cell with a rough ITO electrode

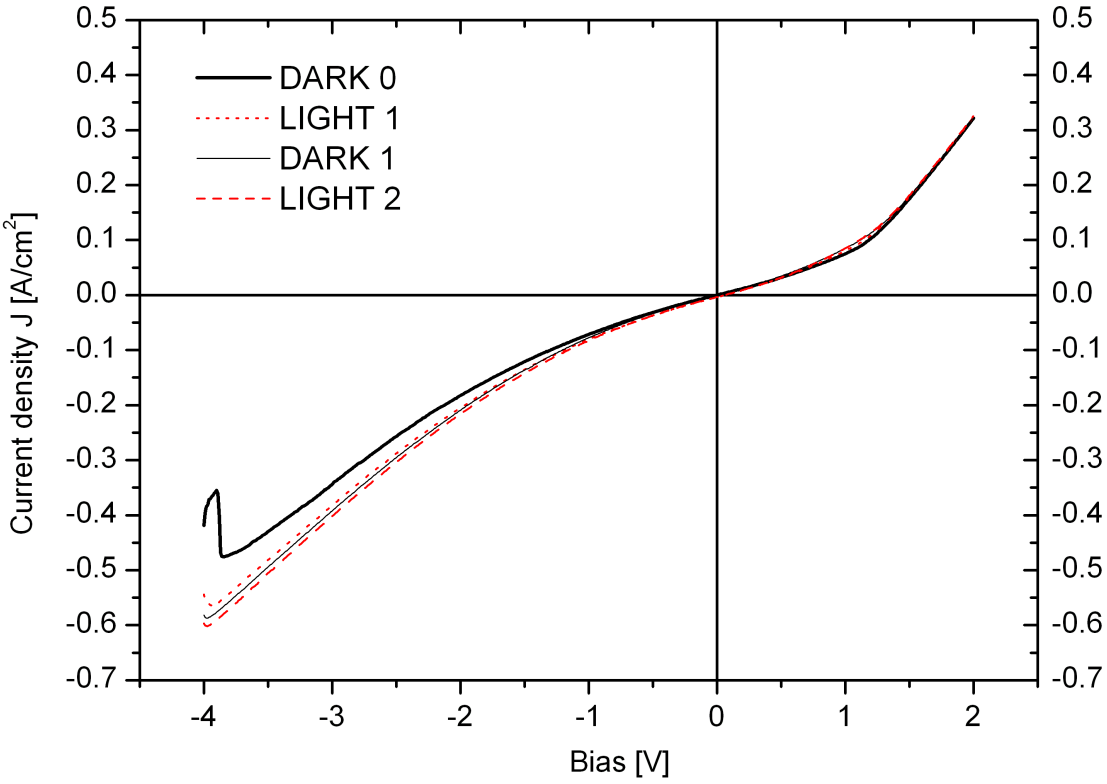

Fig. 6.5: I-V characteristics of the solar cell (glass/ITO/AL(75 nm)/LiF/Al).

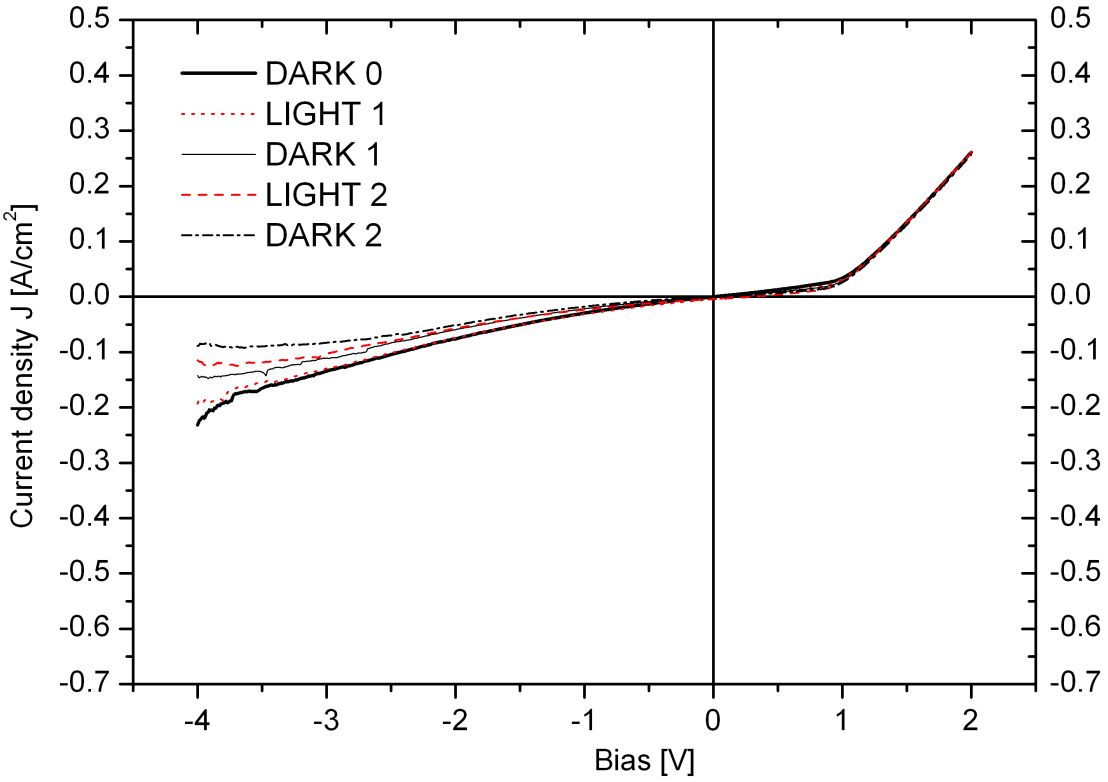

Fig. 6.6: I-V characteristics of the solar cell (glass/ITO/AL(110 nm)/LiF/Al).

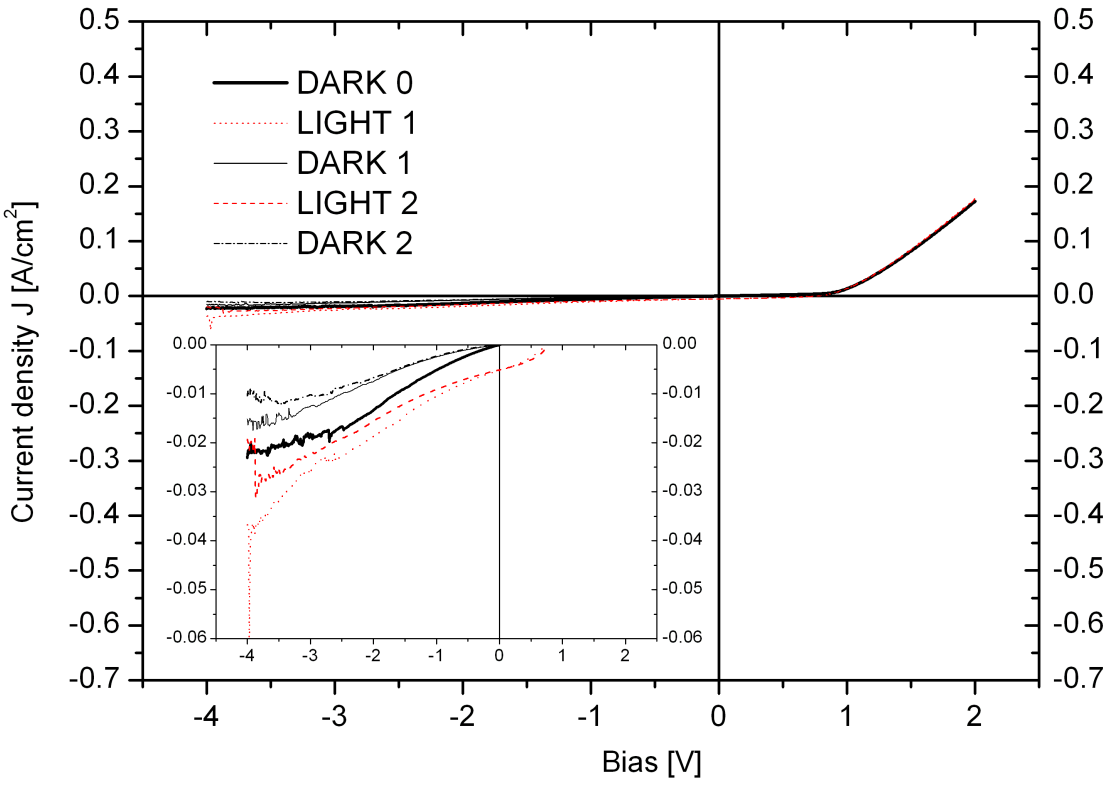

Fig. 6.7: I-V characteristics of the solar cell (glass/ITO/AL(175 nm)/LiF/Al). Inserted graph shows magnified part of main graph.

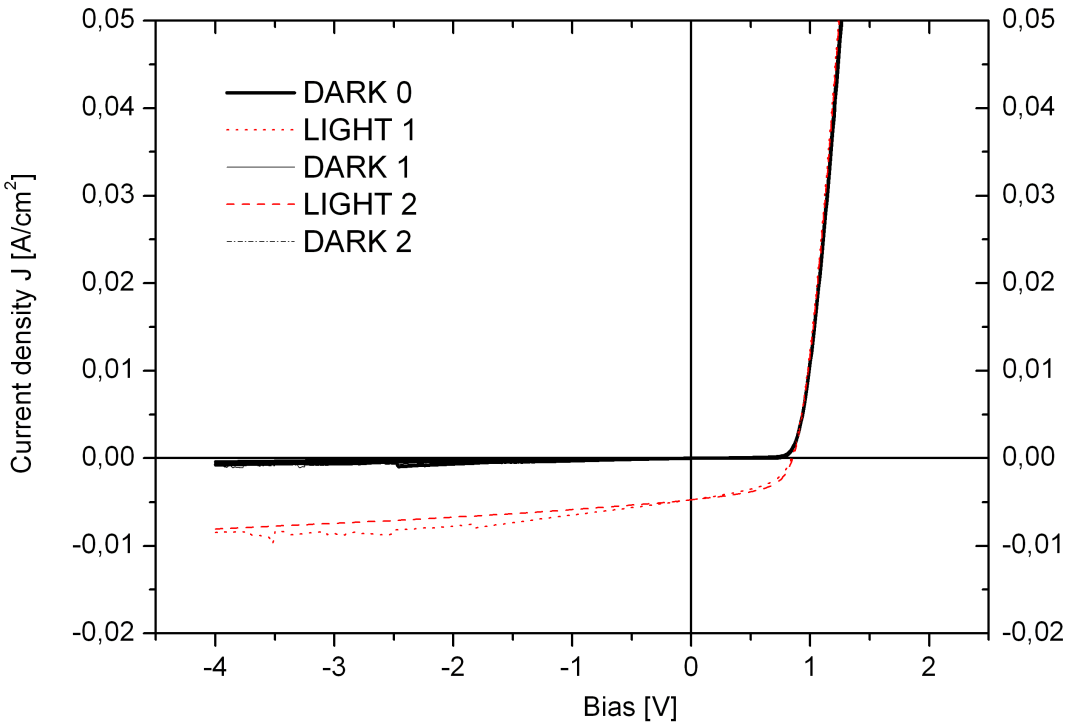

Fig. 6.8: I-V characteristics of the solar cell (glass/ITO/AL(175 nm)/LiF/Al).

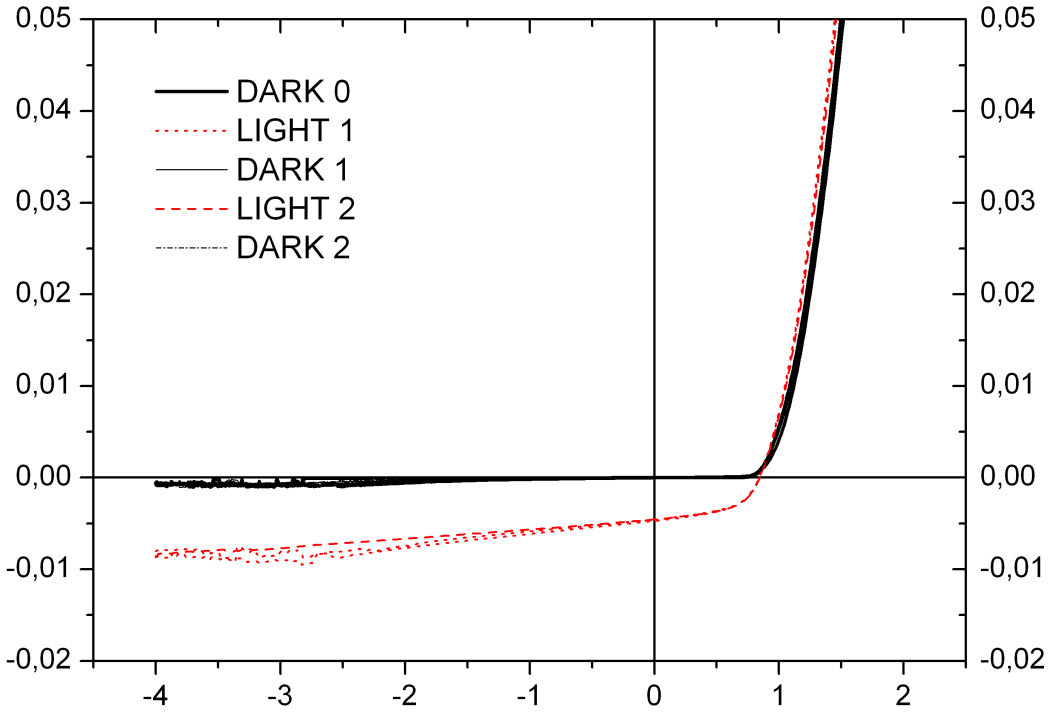

Fig. 6.9: I-V characteristics of the solar cell (glass/ITO/0.5 nm TiO_2/AL(175 nm)/LiF/Al).

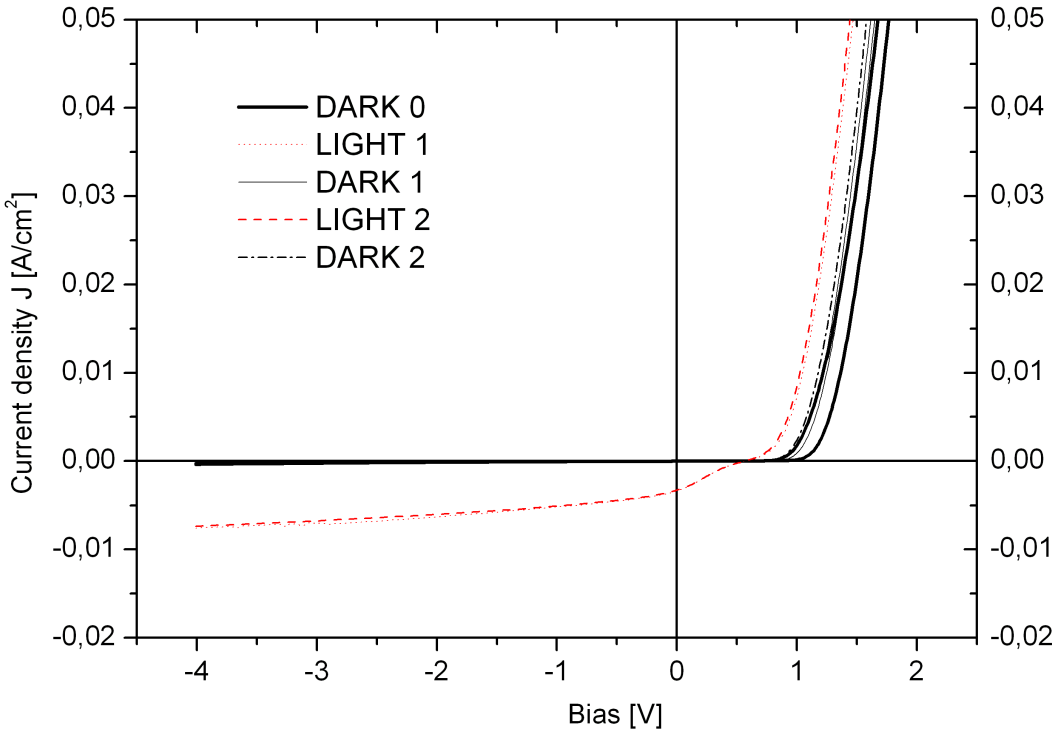

Fig. 6.10: I-V characteristics of the solar cell (glass/ITO/1.5 nm TiO_2/AL(175 nm)/LiF/Al).

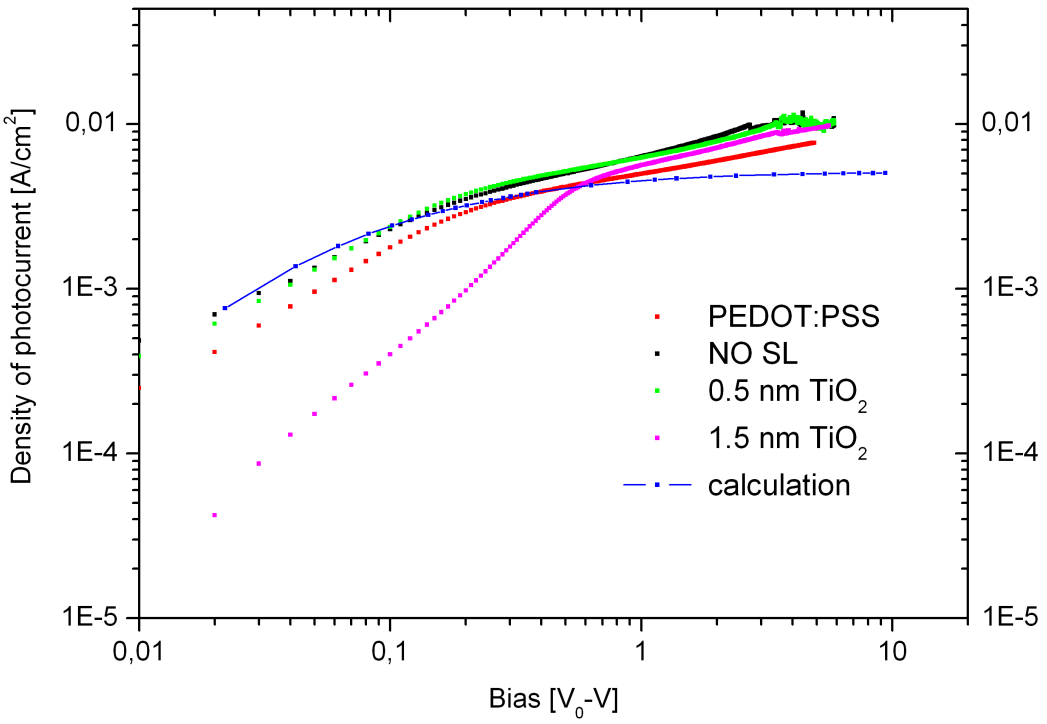

Fig. 6.11: Photocurrent densities of the solar cells (glass/ITO/ ... /AL(175 nm)/LiF/Al).

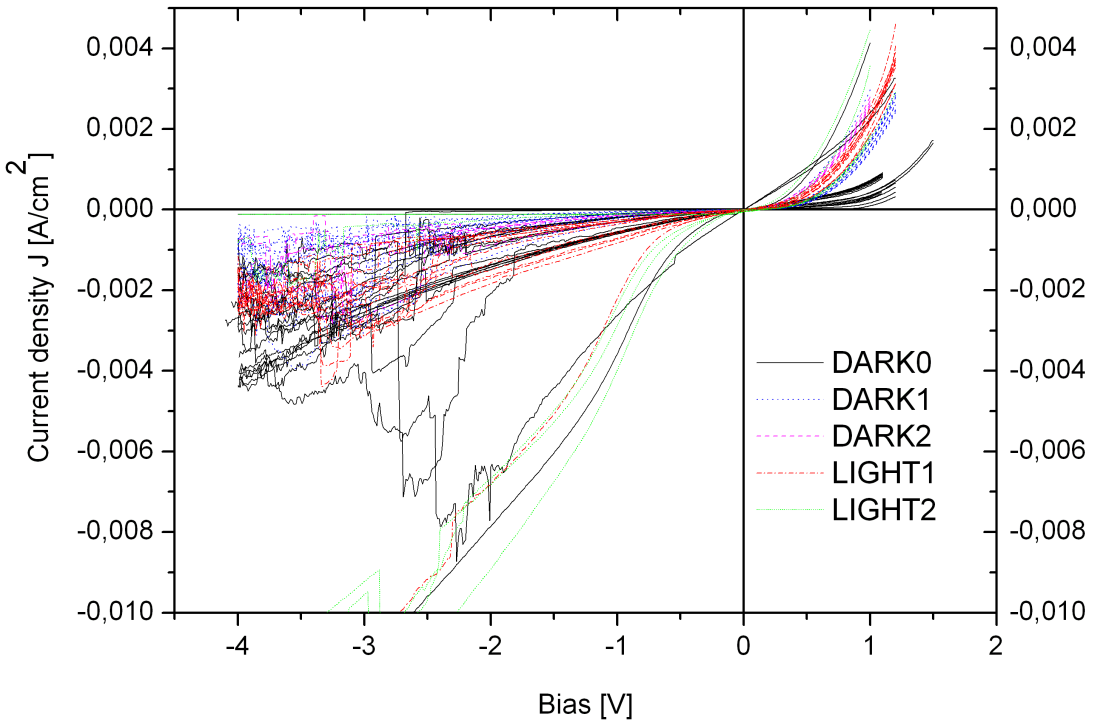

Fig. 6.12: I-V characteristics of the solar cell (glass/ITO/1.5 nm Al_2O_3/AL(175 nm)/LiF/Al).

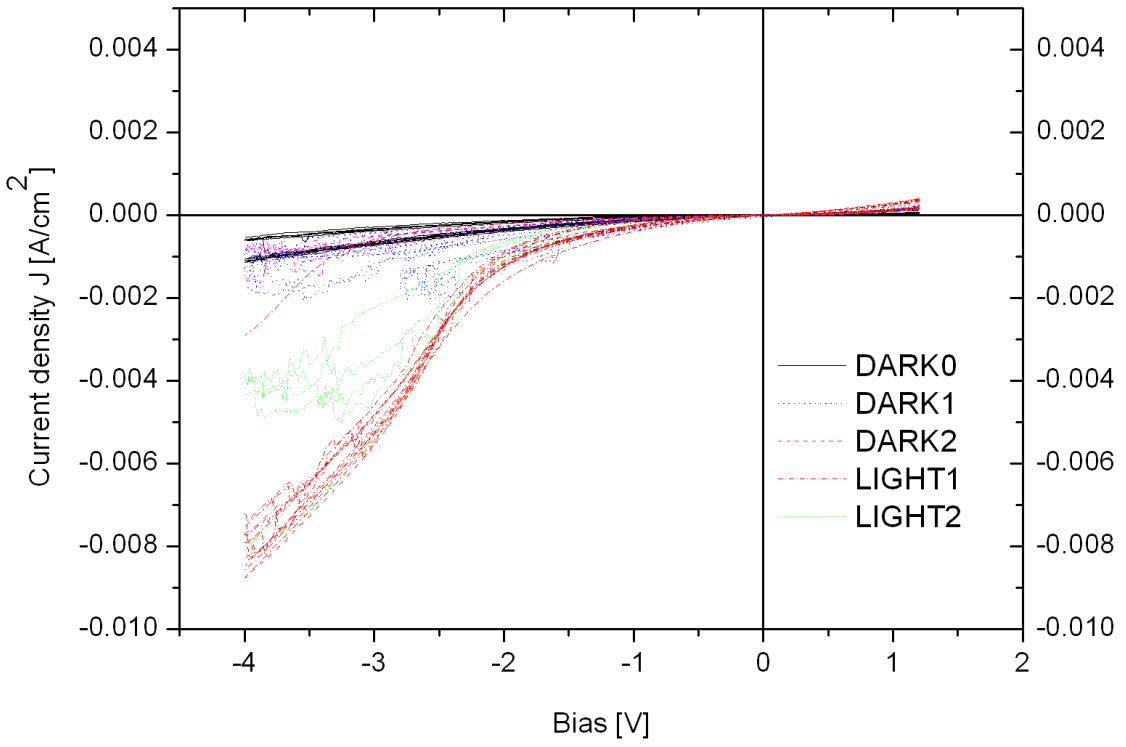

Fig. 6.13: I-V characteristics of the solar cell (glass/ITO/2 nm Al_2O_3/AL(175 nm)/LiF/Al).

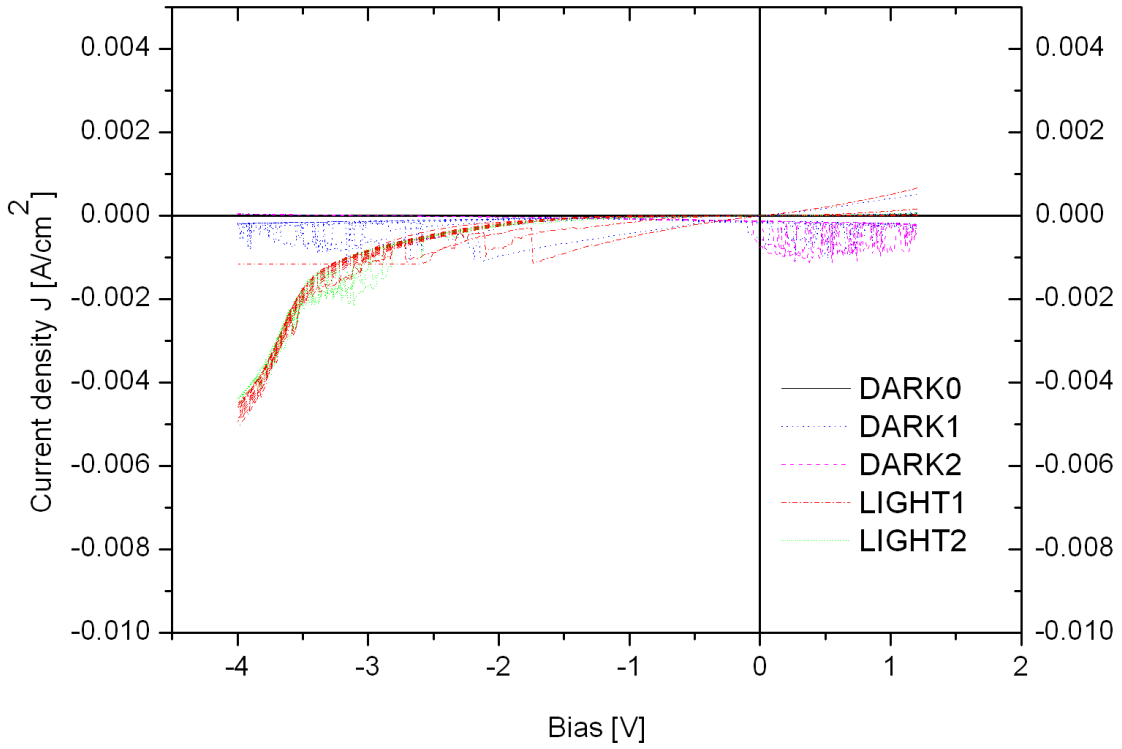

Fig. 6.14: I-V characteristics of the solar cell (glass/ITO/3 nm Al_2O_3/AL(175 nm)/LiF/Al).

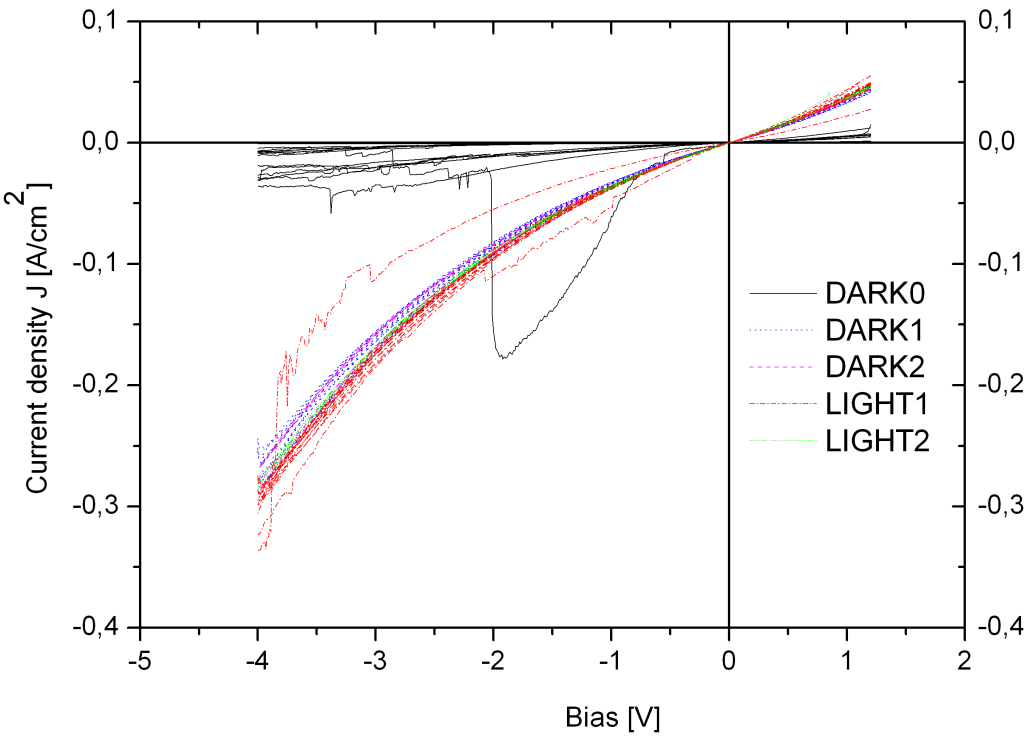

Fig. 6.15: I-V characteristics of the solar cell (glass/ITO/4 nm Al_2O_3/AL(175 nm)/LiF/Al).

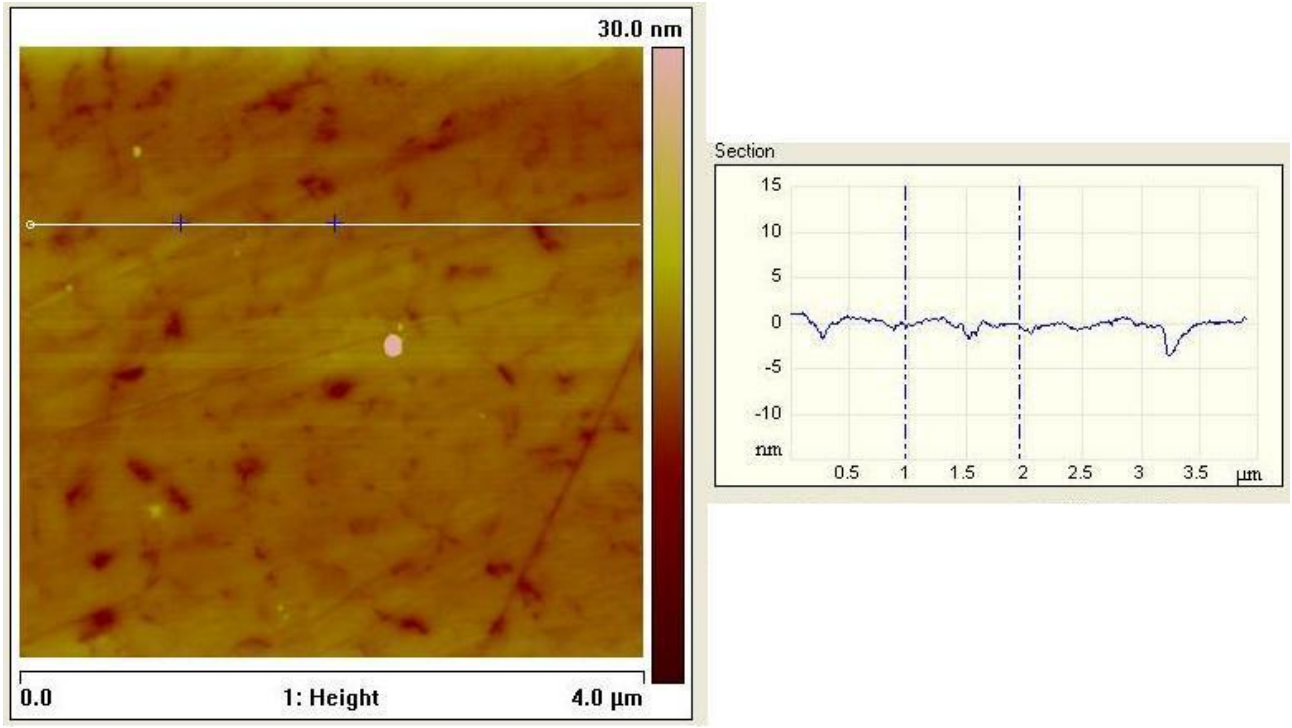

Fig. 6.16: AFM image ($4 \times 4\,\mu m^2$) left: topography, right: cross-section of the polished ITO

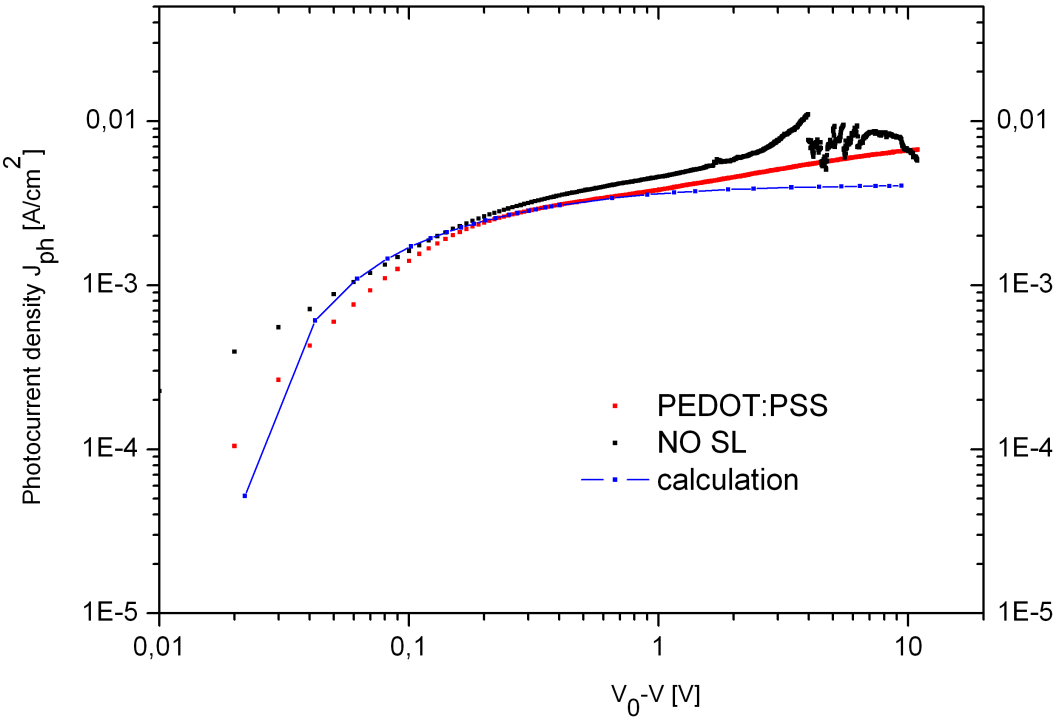

Fig. 6.17: Photocurrent densities of the solar cells (glass/ITO(polished)/AL(175 nm)/LiF/Al, glass/ITO(polished)/PEDOT:PSS/AL(175 nm)/LiF/Al).

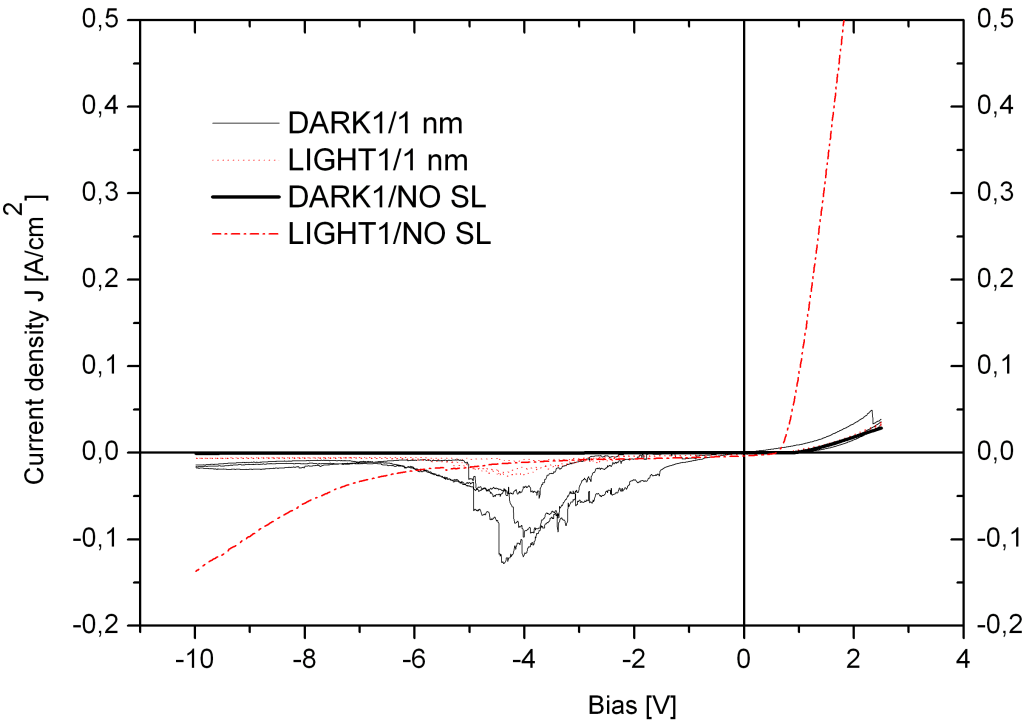

Fig. 6.18: I-V characteristics of the solar cells (glass/ITO(polished)/no SL and 1 nm Al_2O_3/ AL(175 nm)/LiF/Al).

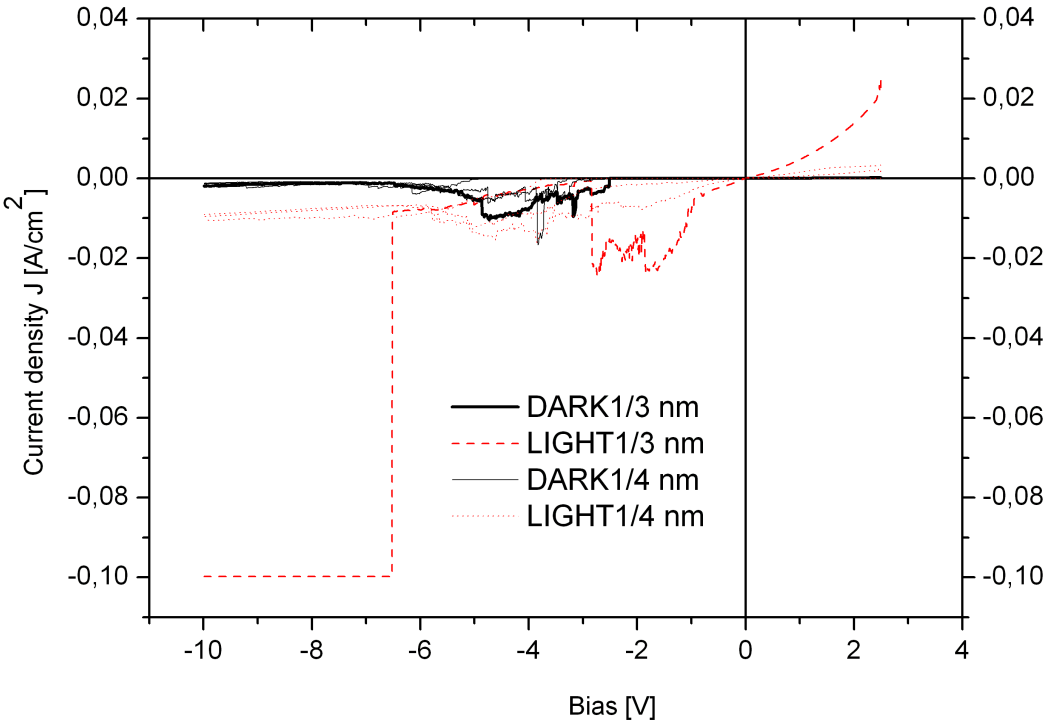

Fig. 6.19: I-V characteristics of the solar cells (glass/ITO(polished)/3 nm and 4 nm Al_2O_3/ AL(175 nm)/LiF/Al).

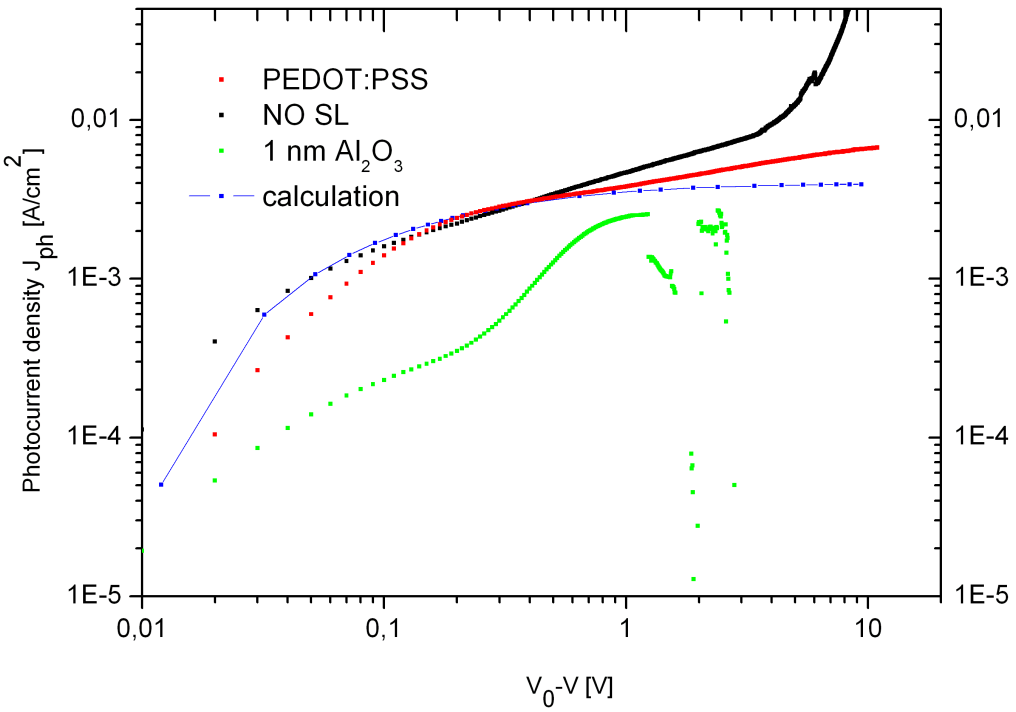

Fig. 6.20: Photocurrent densities of the solar cells (glass/ITO(polished)/. . . /AL(175 nm)/ LiF/Al).

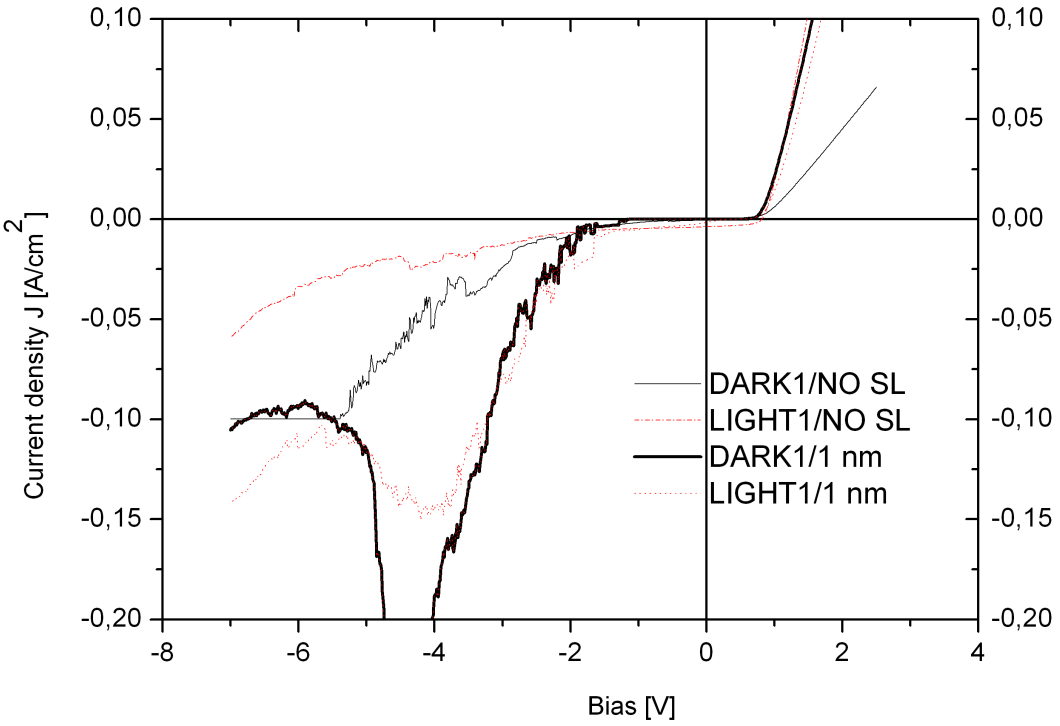

Fig. 6.21: I-V characteristics of the solar cells (glass/ITO(polished)/no SL and 1 nm Al_2O_3/ AL(75 nm)/LiF/Al).

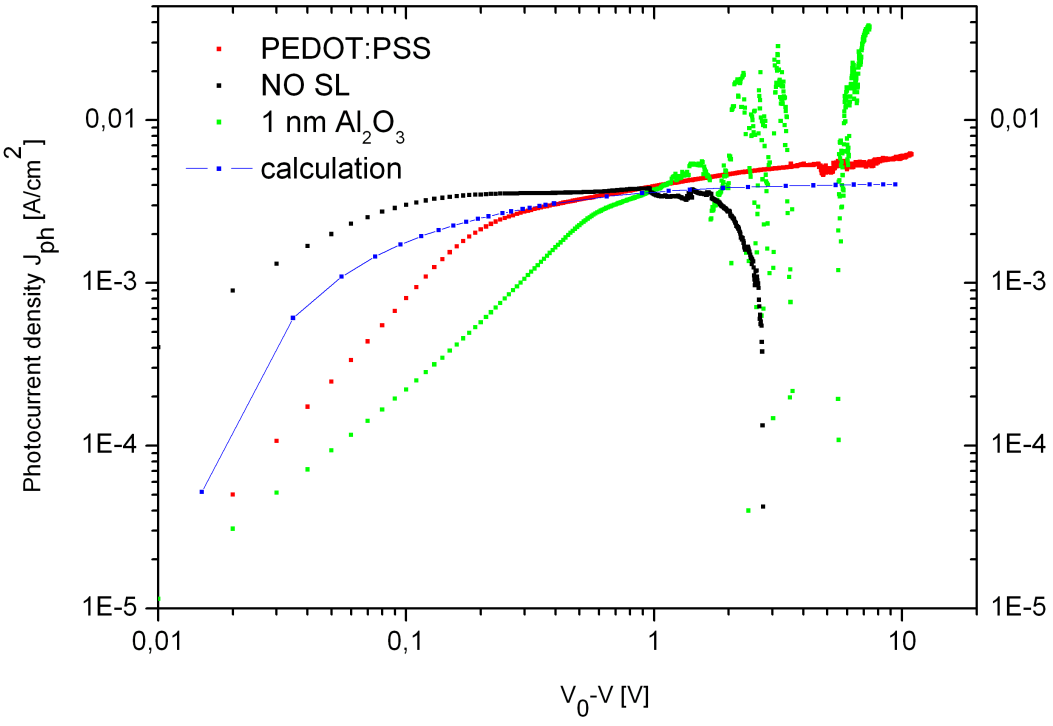

Fig. 6.22: Photocurrent densities of the solar cells (glass/ITO(polished)/. . . /AL(75 nm)/ LiF/Al).

SL	AL thickness [nm]	ITO	I_{SC}[mA/cm^2]	V_{OC} [V]	FF	Fig.
NO	175	non-polished	4.29	0.95	0.65	6.8
PEDOT:PSS	175	non-polished	4.38	0.96	0.63	-
0.5 nm TiO_2	175	non-polished	4.51	0.91	0.62	6.9
1.5 nm TiO_2	175	non-polished	3.82	0.64	0.46	6.10
1.5 nm Al_2O_3	175	non-polished	0.00	0.01	0.00	6.12
2 nm Al_2O_3	175	non-polished	0.00	0.00	0.00	6.13
3 nm Al_2O_3	175	non-polished	0.00	0.00	0.00	6.14
4 nm Al_2O_3	175	non-polished	0.00	0.00	0.00	6.15
NO	175	polished	3.69	0.61	0.56	6.18
PEDOT:PSS	175	polished	4.42	0.96	0.65	-
1.5 nm Al_2O_3	175	polished	2.31	0.48	0.26	6.18
3 nm Al_2O_3	175	polished	0.00	0.00	0.00	6.19
4 nm Al_2O_3	175	polished	0.00	0.00	0.00	6.19
NO	1500	polished	3.92	0.72	0.60	6.21
PEDOT:PSS	72	polished	4.35	0.95	0.63	-
1.5 nm Al_2O_3	75	polished	2.52	0.48	0.29	6.21

Tab. 6.2: I-V characteristic of SCs.

Chapter 7

KP - AFM measurement of organic solar cells

7.1. Introduction

The transport of charges in organic semiconductors was studied in many works [29,32,33,74].

The shift in the CPD of SCs under and after the illumination was explained [74]. It was supposed that the shift in the CPD of MDMO-PPV (e-donor) would take place towards lower values and the shift in the CPD of PCBM (e-acceptor) to higher values. It was surprising that the shift for both MDMO-PPV and PCBM was observed in the same direction. For investigation this effect the SL is used to block a charge injection to the ITO electrode from AL.

Principle of the measurement with KP - AFM is described in section 2.7.

7.2. Experiment

All samples were prepared in the way listed in subsection 5.2.6. The MultiMode^{TM} (Veeco) AFM microscope with the Electric extender model was used for KP - AFM measurements (0.01 % basic accuracy with 5 - digit resolution), a white halogen lamp (spectrum of light: 385 - 720 nm) was used for illumination. All measurements were performed in a nitrogen atmosphere (less than 1 ppm of H_2O and 1 ppm of O_2) to avoid oxidation of AL. The tip with Pt coating (OMCL-AC240TM-B2 Olympus, apex radius <15 nm, $k \gg 2$ N/m, cone angle 25°, resonant frequency ~ 70 kHz) was used.

At first, the samples without any previous illumination (DARK0) were measured, than the light was turned on (LIGHT1). At the end the light was turned off to measure the samples again (DARK1). From each measurement a CPD map of the sample was obtained. This map was processed to CPD histogram as a distribution of the number of points with the same voltage (see Fig. 7.1).

The results of CPD measurements of samples with Al_2O_3 or TiO_2 are in Fig 7.2 - 7.7. Note that due to poor lateral resolution of KP - AFM only one integral peak instead of two ones was observed. The schematic of the results is in Fig. 7.8.

Experiment DARK0→DARK1

- **TiO_2**: The layer of TiO2 blocks the transport of holes to ITO from AL. Holes are pilled up in AL. It causes the CPD shift to the higher value. But with an increasing

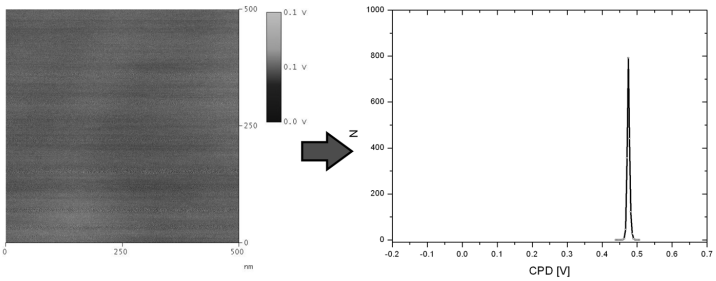

Fig. 7.1: The CPD map (500x500 nm^2) and the histogram obtained for the sample with 3 nm TiO_2 layer, DARK0

thickness of TiO_2 more negative interface states of TiO_2 are filled. It causes the CPD shift back to the lower value (see Fig. 7.8 TiO_2 DARK0→DARK1).

- **Al_2O_3**: The difference between DARK0 and DARK1 has no predict development and can be caused by measurement errors for thicknesses 2 and 3 nm (see Fig. 7.8 Al_2O_3 DARK0→DARK1). It is caused by the fact that the layer of Al_2O_3 blocks both charge carriers.

Experiment DARK1→LIGHT1

- **TiO_2**: The layer of TiO_2 blocks transport of holes into ITO from AL (Fig. 5.7). Holes are pilled up in AL. CPD shifts to the lower value (see Fig. 7.8 TiO_2 DARK1→LIGHT1).
- **Al_2O_3**: The little shift in CPD to the higher value shows the small amount of electrons. But this shift is so small that it can neglected (see Fig. 7.8 Al_2O_3 DARK1→LIGHT1).

7.3. Summary

The CPD measurements of the samples with Al_2O_3 have not revealed any significant charge transfer on average. It was causing by big blocking barrier for both charge carriers.

The CPD measurements of the samples with TiO_2 have indicated pilling up holes. But for thicker layers interface negative states were created and electrons were pilled up into them. It caused the CPD shifts to lower values.

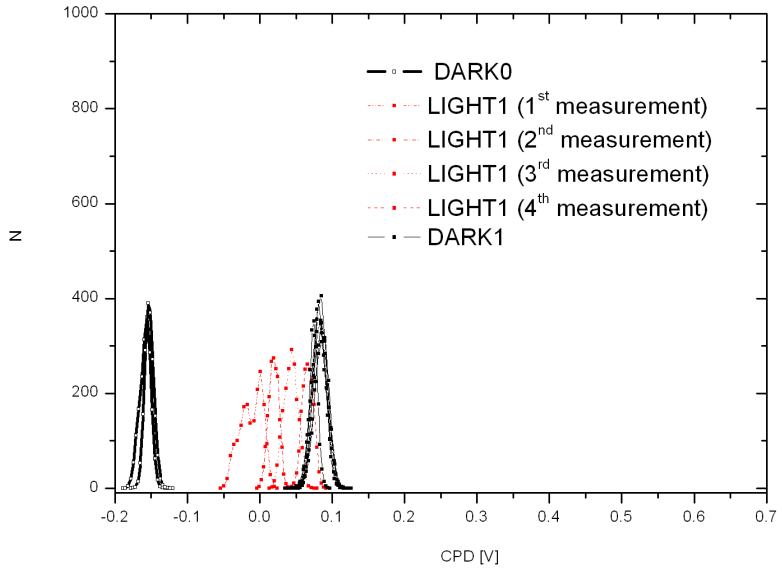

Fig. 7.2: CPD histogram (glass/ITO/1 nm TiO_2/AL(75 nm)

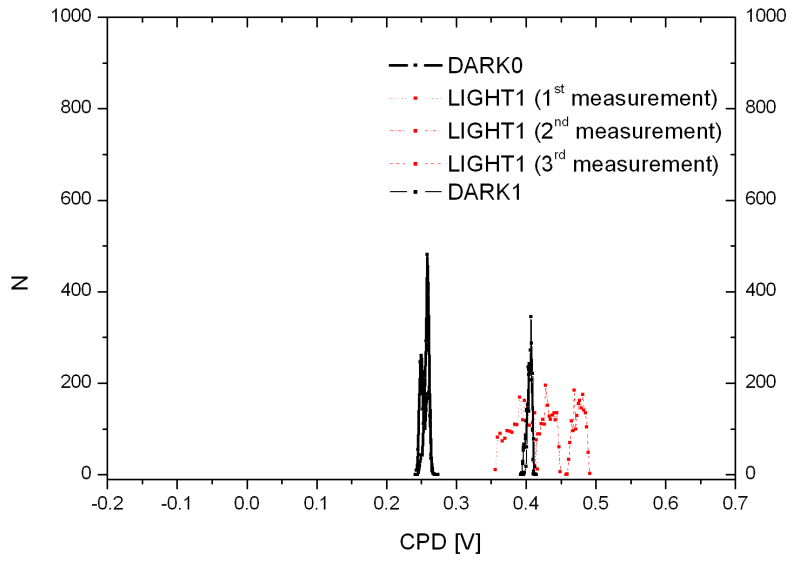

Fig. 7.3: CPD histogram (glass/ITO/2 nm TiO_2/AL(75 nm)

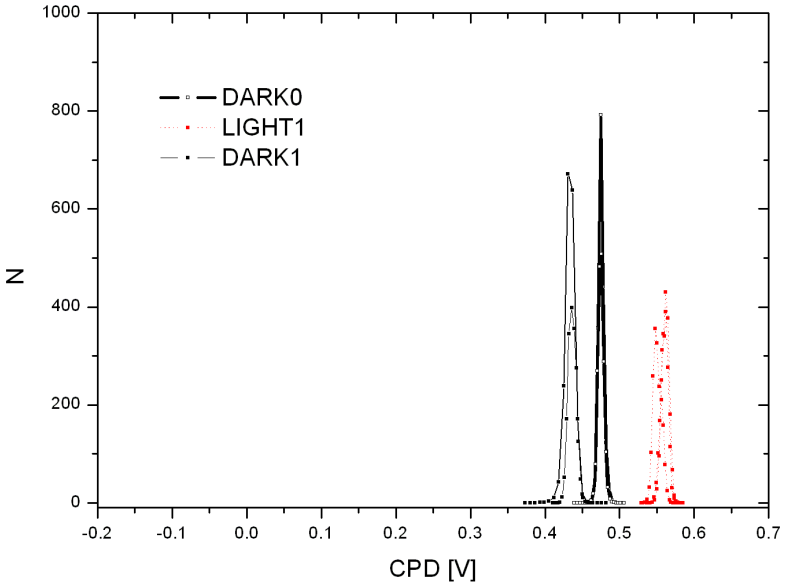

Fig. 7.4: CPD histogram (glass/ITO/3 nm TiO_2/AL(75 nm)

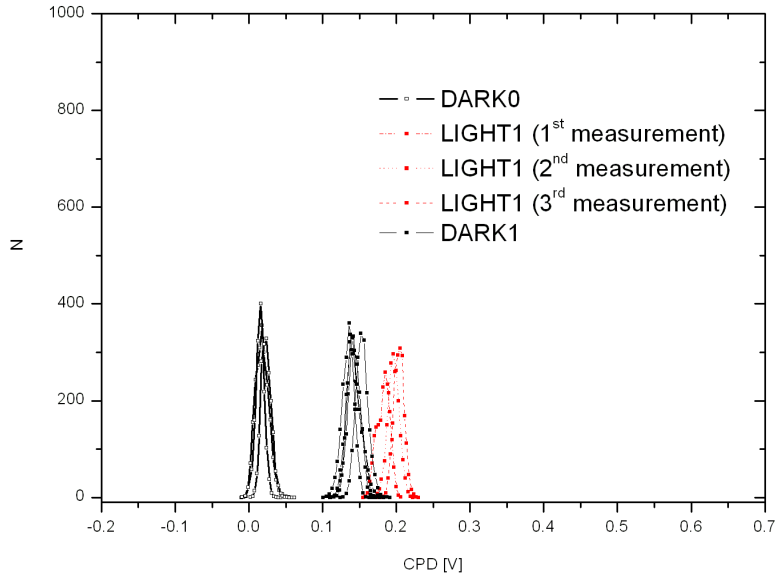

Fig. 7.5: CPD histogram (glass/ITO/1 nm Al_2O_3/AL(75 nm)

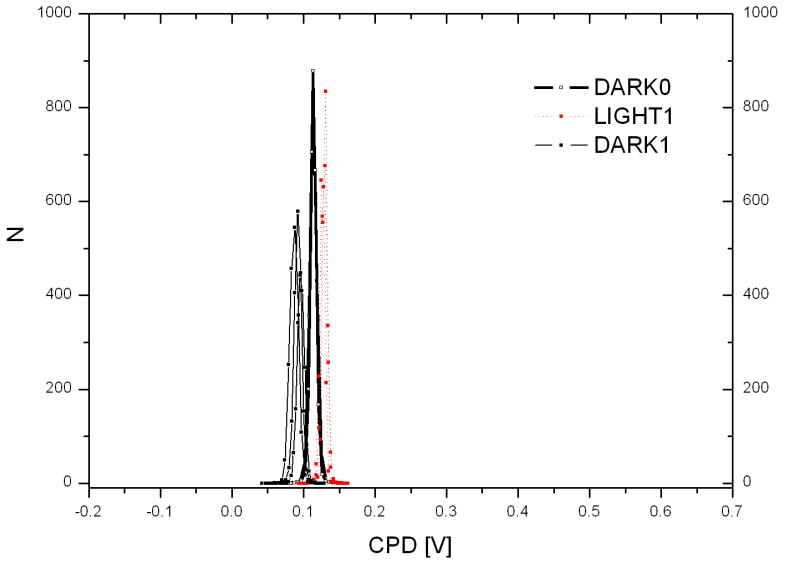

Fig. 7.6: CPD histogram (glass/ITO/2 nm Al_2O_3/AL(75 nm)

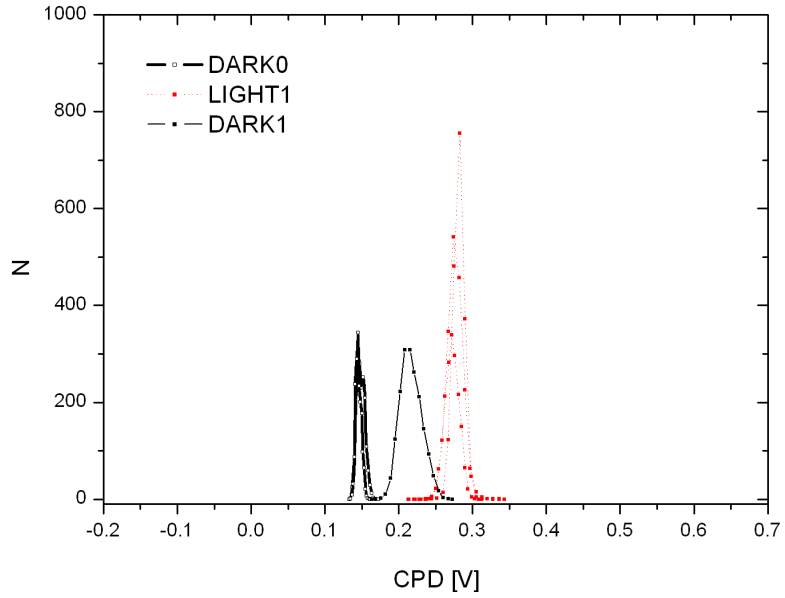

Fig. 7.7: CPD histogram (glass/ITO/3 nm Al_2O_3/AL(75 nm)

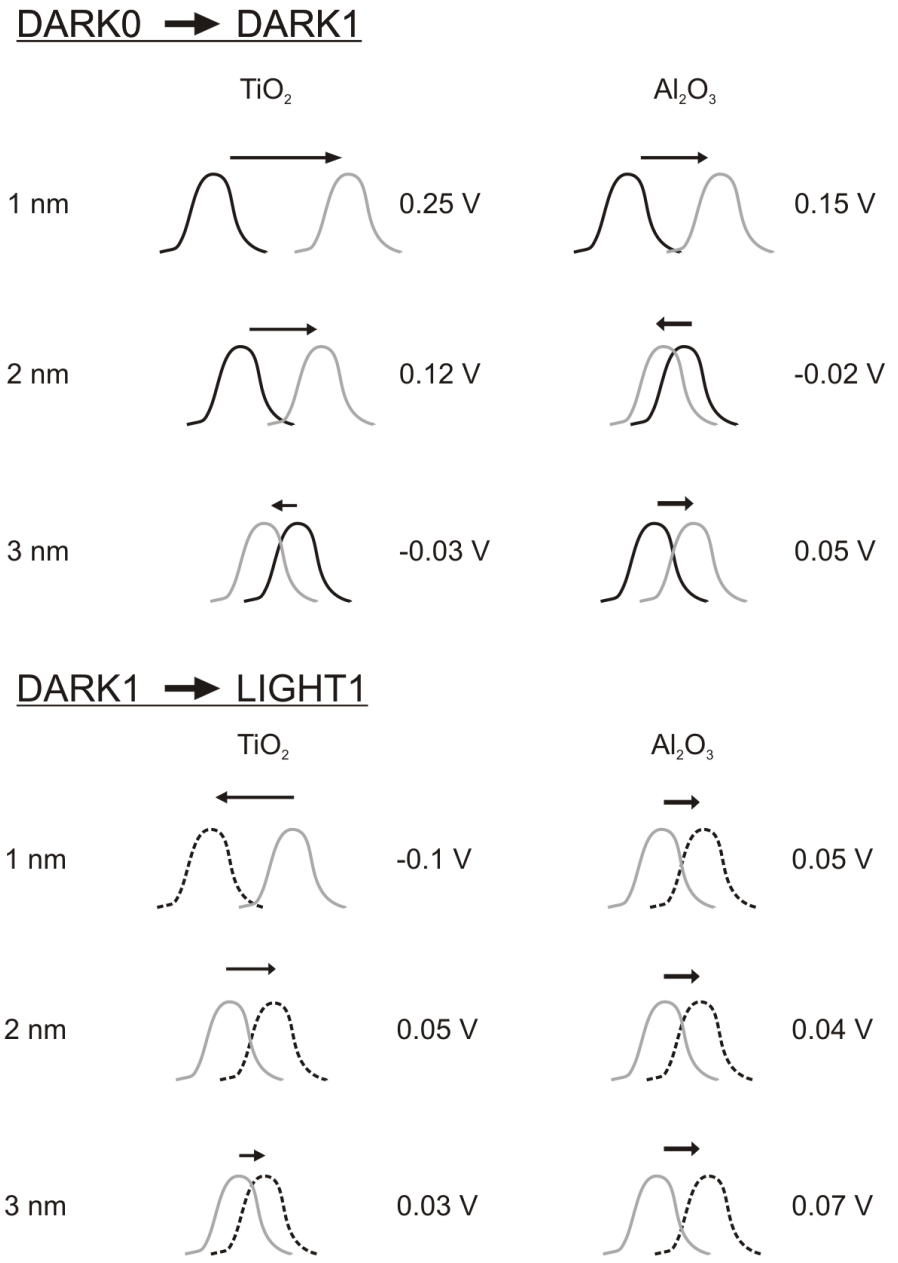

Fig. 7.8: The schematic histograms of CPD: 1, 2, 3 nm of Al_2O_3 and TiO_2; DARK0 - black line, DARK1 - grey line, LIGHT1 - dashed line.

Chapter 8

Preparation of gold tips for STM/STS

8.1. Introduction

STM/STS technique offers us an extreme spatial resolution. But for this resolution we need the well-defined tip geometry with a very sharp and narrow symmetric apex. For preparation of those tips Au wire with the diameter 0.2 mm was used. The modified procedure described by Michael G. Boyle *et al.*[76] was followed. The final apex radius was around 40 - 60 nm.

The gold tips have some advantages compared to the platinum ones. They have better conductivity and better stability under the air conditions. The platinum tip becomes covered with an oxide layer and so the work function of the tip increases.

8.2. Preparation

The following things have to be done before the beginning of the etching:

- Ultrasonic cleaning of the 99.999% pure Au straight wire (lenght ∼20 mm) in ethanol. The upper end is coated with a common nail varnish along a distance of 3.5 mm.
- Preparation of the fresh solution of 20% $CaCl_2$ in H_2O.
- Platinum loop (0.5 mm diameter of wire) with a diameter of 10 mm.

8.3. Etching process

The etching process has two steps and the fabrication uses the "drop-off" technique [77]. The advantage of this procedure is that no toxic chemicals are used.

8.3.1. First step

The outline of etching setup is in Fig. 8.1 a). The procedure consists of the steps as follows:

- The gold wire is dipped into the solution slightly above the coated end.

- The voltage is set up to $U_{DC} = -5\,\mathrm{V}$, with the AC modulation voltage $U_{PP} = 9\,\mathrm{V}$ (peak to peak) and the frequency $f = 2\,kHz$. The values of voltages are chosen in such a way that the etching voltage remains negative to avoid cathodic deposition on the wire.
- The current is kept in the range of 20 - 25 mA.
- The etching is interrupted as soon as the diameter of the wire neck (see Fig. 8.1 b)) is close to 10 μm. The diameter is controlled with a magnifying glass. The etching coarse takes 15 - 40 seconds. Its exact time depends on the concentration of solution and characteristics of the power source.

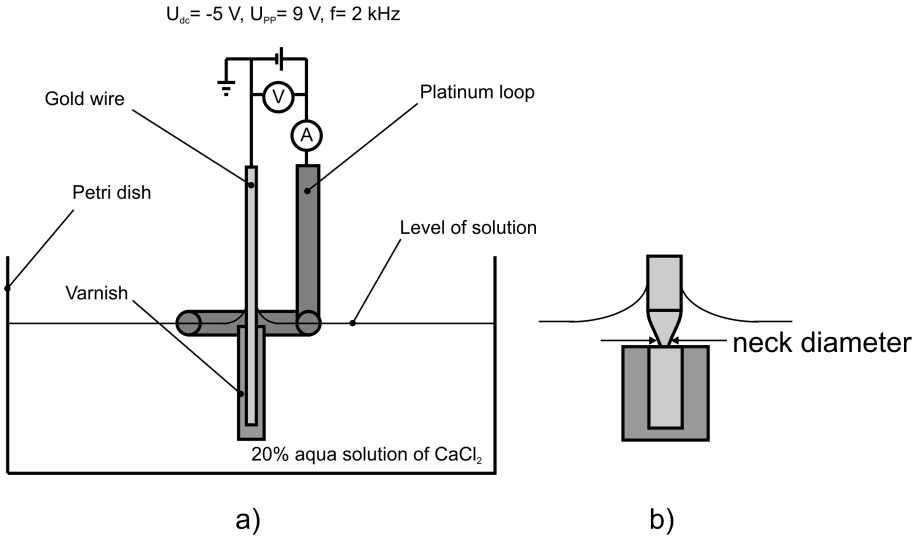

Fig. 8.1: The first etching step: a) set up, b) the neck of the gold wire.

8.3.2. Second step

The second step of etching is the same as for the first step, but the DC voltage is changed as follows:

- $U_{DC} = -5\,\mathrm{V}$.
- The etching continues until the coated part of the wire drop off. This final etching takes from 10 s to 2 min. The exact time depends on the neck diameter. The best time for shut off with respect to the best shape of the apex is reported 250 ns [76]. This is done by a control circuit. The control unit measures the etching current and when the lower part of the tip drops off the etching current decreases very fast and the control unit turns off the DC voltage.

8.4. Experiment and results

The first three etchings were done with a carbon rod electrode instead of the platinum loop to the verify etching process. The resulting tips are shown in Fig. 8.2 - 8.5. The apex radius was around 80 - 100 nm. The etching process was turned off manually.

During etching big bubbles were created. It was decided to use another solution for etching to decrease the size of bubbles and the apex radius. A solution of $CaCl_2$:C_2H_5OH:H_2O in the mass ratio 2:8:1 [78] was prepared. The bubbles were slightly smaller but the wire collected much more impurities than the tips fabricated in solution without ethanol (see Fig. 8.6).

The solution of $CaCl_2$:H_20 in the mass ratio 1:4 was used again, but the etching solution was cooled with ice. The pictures of resultant tips are in Fig. 8.7-8.9. The apex radius was around 40 nm.

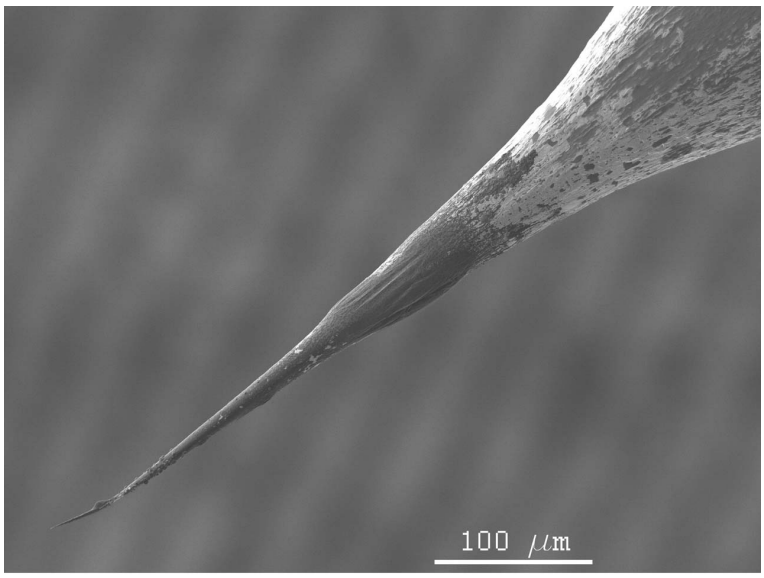

Fig. 8.2: The apex of a gold tip (carbon rod electrode, manual turn off, $CaCl_2$:H_2O, SE SEM picture).

Fig. 8.3: The apex of a gold tip (carbon rod electrode, manual turn off, $CaCl_2$:H_2O, SE SEM picture).

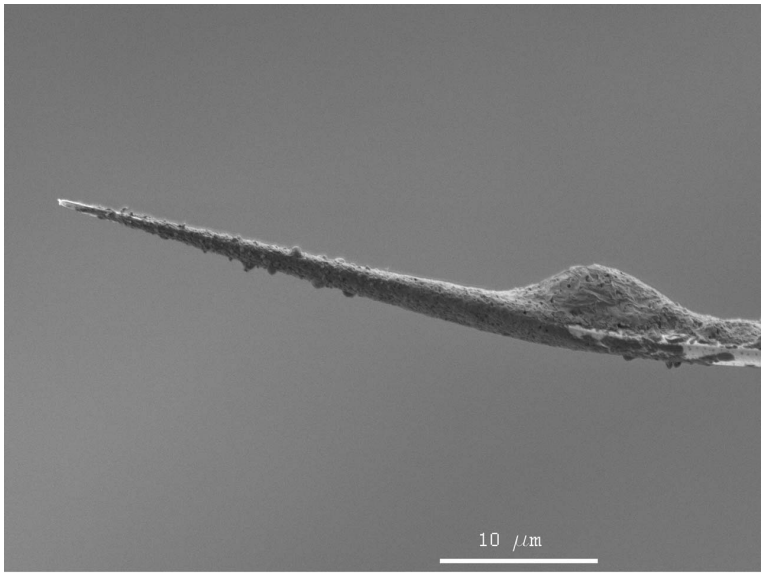

Fig. 8.4: The apex of a gold tip (carbon rod electrode, manual turn off, $CaCl_2$:H_2O, SE SEM picture).

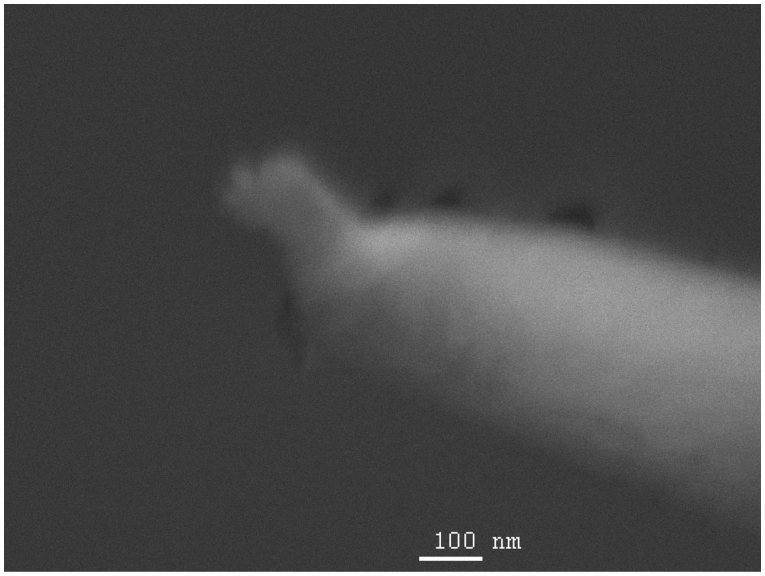

Fig. 8.5: The apex of a gold tip (carbon rod electrode, manual turn off, $CaCl_2$:H_2O, SE SEM picture).

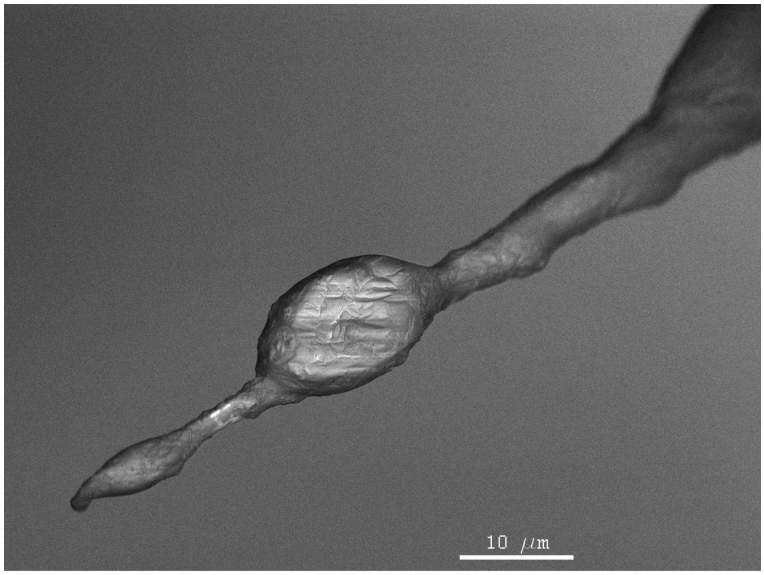

Fig. 8.6: The apex of a gold tip (carbon rod electrode, manual turn off, $CaCl_2$:C_2H_5OH:H_2O, SE SEM picture).

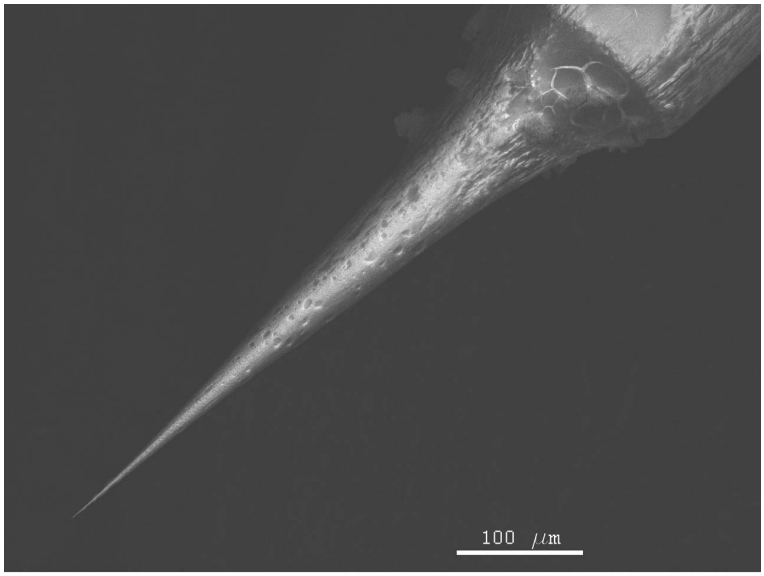

Fig. 8.7: The apex of a gold tip (carbon rod electrode, manual turn off, $CaCl_2$:H_2O, ice cooling, SE SEM picture).

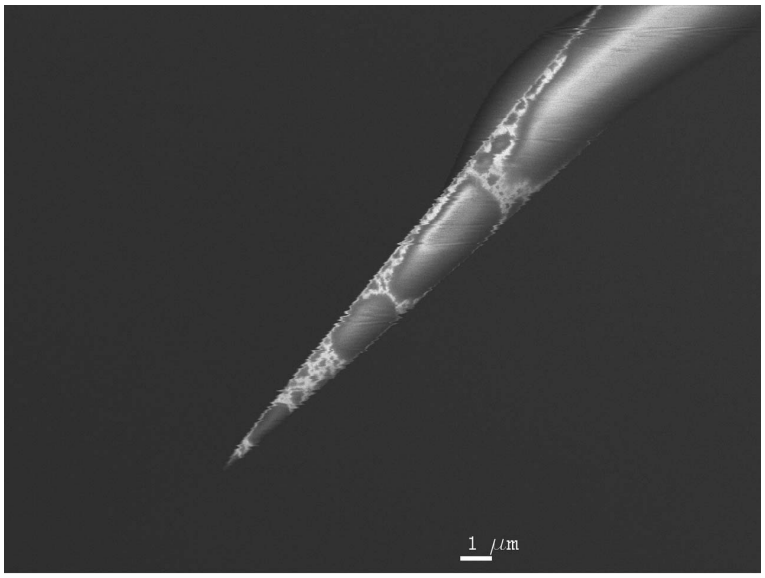

Fig. 8.8: The apex of a gold tip (carbon rod electrode, manual turn off, $CaCl_2$:H_2O, ice cooling, BSE SEM picture).

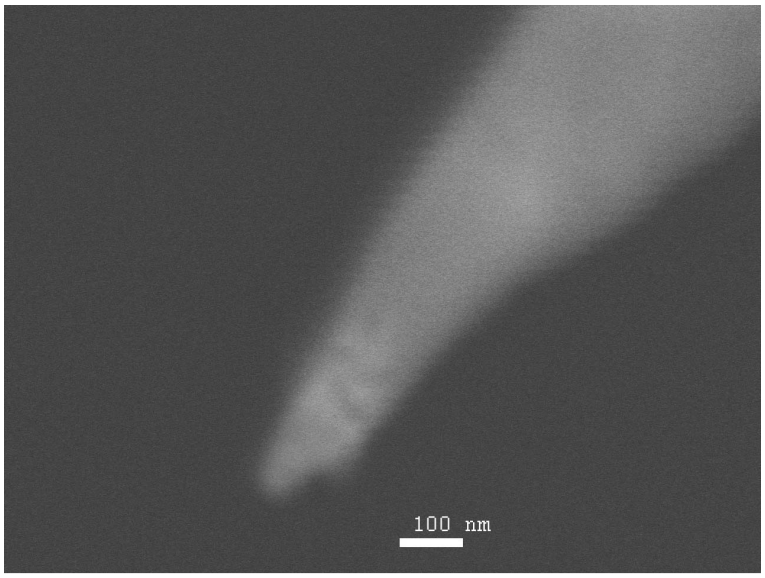

Fig. 8.9: The apex of a gold tip (carbon rod electrode, manual turn off, $CaCl_2$:H_2O, ice cooling, SE SEM picture).

Chapter 9

Conclusions

A study of the combined AFM/SEM system was presented in this diploma thesis. AFM and SEM techniques (the detection of backscattered and Auger electrons or X-ray spectroscopy) can be used simultaneously. To provide it a previous design of AFM was modified. Especially, a new design of mirror and sample transport system had to be made.

The second part of this diploma thesis deals with the problem of organic solar cells, the topic having been studied during a 6 - month study period of the author at Eindhoven University of Technology (ERASMUS exchange mobility school). In this part the spacer layers (Al_2O_3 or TiO_2) were used for the investigation of the charge transport in the organic solar cells.

In the bulk I-V measurements of these devices a high leakage current was present. This problem was solved by using a thicker layer of the AL (175 nm) and by polishing of ITO. TiO_2 without polished ITO decreased the value of the photocurrent. The samples with Al_2O_3 possessed a high leakage current and switching behaviour in the region of our interest.

We succeeded to perform CPD measurements on the samples with Al_2O_3 and TiO_2. Measurements on the samples with Al_2O_3 did not show any significant shift. It was caused by a high blocking barrier of Al_2O_3 for both charge carriers. Layers of TiO_2 should block only holes, but with higher thicknesses of TiO_2 layers more negative interface states of TiO_2 were created and filled.

Gold tips with the apex radius around 40 - 60 nm were prepared. This fabrication is easily reproducible, nontoxic and fast.

Chapter 10

Appendix

10.1. List of data on the enclosed CD

folder	files	description
SSS - MARRA		
	AI_HR4_10000E_XY.CATPart	model of the *xy* transport system
	dn35r-1.CATPart	model of the Conflat DN35
	dn100-1.CATPart	model of the Conflat DN100
	dn100-2.CATPart	model of the Conflat DN100
	dn150-1.CATPart	model of the Conflat DN150
	dn150-2.CATPart	model of the Conflat DN150
	dno-komory-1.CATPart	model of the chamber bottom
	EDX-35-16mm-1.CATPart	model of the EDX detector
	laserovy paprsek.CATPart	model of laser beam trace
	M8x55-1.CATPart	model of the bolt M8-55
	matice M8-1-1.CATPart	model of the nut M8
	matice M8-1.CATPart	model of the nut M8
	podlozka pro M8-1.CATPart	model of the washer for M8
	priruba na EDX-1.CATPart	model of the conflat for EDX detector
	RBSE-LM-1.CATPart	model of the RBSE detector
	SAM - OMICRON-1.CATPart	model of the SAM analyzer
	SAM - OMICRON-rd.CATPart	model of the redesigned SAM analyzer
	SAM - SPECS-150-1.CATPart	model of the SAM analyzer
	SAM - SPECS-150-rd.CATPart	model of the redesigned SAM analyzer
	SE_detector.CATPart	model of the SE detector
	spodni priruba-1.CATPart	model of the bottom flange
	SSS - MARRA.CATProduct	SSS - MARRA assembly
	TBF-00_s_FIB_ob.CATPart	model of the SEM microscope
	telo-trubka.CATPart	model of the UHV chamber
	Tes-komoraVs.dno-1.CATPart	model of copper ring
	trubka na SAM-1.CATPart	model of the SAM flange
	VlnovecZ.CATPart	model of the bellows

folder	files	description
SSS - MARRA sd		slope design
	AFM-uprava.CATPart	model of the modified AFM
	Cantilever.CATPart	model of the cantilever
	dn35r-2.CATPart	model of the Conflat DN35
	dn100-2.CATPart	model of the Conflat DN100
	dn150-2.CATPart	model of the Conflat DN150
	dno komory-2.CATPart	model of the chamber bottom
	Drzak_cant_n.CATPart	model of the new cantilever holder
	EDX-35-16mm-2.CATPart	model of the EDX detector
	Inchworm.CATPart	model of the inchworm
	M1.6_NUT.CATPart	model of the M1.6 nut
	laserovy paprsek-2.CATPart	model of laser beam trace
	miniperko.CATPart	model of the cant. holder spring
	MIRA-2.CATPart	model of the SEM microscope
	Nova_zakladni_deska.CATPart	model of the new bottom AFM desk
	Nova_vrchni_deska.CATPart	model of the new top AFM desk
	priruba na EDX-2.CATPart	model of the conflat for EDX detector
	SAM - SPECS-150-2.CATPart	model of the SAM analyzer
	sestava.CATProduct	assembly of SSS - MARRA slope design
	telo - sikme SEM.CATPart	model of the UHV chamber
	Tes-komoraVs.dno-2.CATPart	model of copper ring
	trubka na SAM-2.CATPart	model of the SAM flange
	Trubka pro RBSE.CATPart	model of the RBSE flange
	trubka pro SAM.CATPart	model of the modified SAM flange
-\Navrh_xyz_posuvu		x,y,z motion system design
	burt_pero.CATPart	model of the leaf spring
	burt_pero_2.CATPart	model of the leaf spring
	Drzak_inchwormu.CATPart	model of the inchworm holder
	Inchworm.CATPart	model of the inchworm
	M3_NUT.CATPart	model of the M3 nut
	M4_NUT.CATPart	model of the M4 nut
	M3x12_SCREW.CATPart	model of the M3x12 srew
	M3x30_SCREW.CATPart	model of the M3x30 srew
	M4x8_SCREW.CATPart	model of the M4x8 srew
	M4x12_SCREW.CATPart	model of the M4x12 srew
	Navrh_xyz_posuvu.CATProduct	assembly of x,y,z motion system
	Piezo_5x5x1.CATPart	model of the piezoceramic 5x5x1 mm
	Saf_pulvalecky.CATPart	model of the sapphire halfrod
	Scanner.CATPart	model of the scanner
	Sym_M3_NUT.CATPart	model of the M3 nut
	Sym_M3x30_SCREW.CATPart	model of the M3x30 nut
	Sym_Piezo_5x5x1.CATPart	model of the piezoceramic 5x5x1 mm
	X_stolek.CATPart	model of the x - wagon
	Y_desticka_1.CATPart	model of the y - bar-1
	Y_desticka_2.CATPart	model of the y - bar-1
	Y_stolek.CATPart	model of the x - wagon

folder	files	description
-\Zrcadla		
	Kot_jedna-sp.CATPart	model of the kotouc_1 vrch
	Kot_jedna-vr.CATPart	model of the kotouc_1 spodek
	M2x6_SCREW	model of the M2x6 screw
	M2x8_SCREW	model of the M2x8 screw
	M2x10_SCREW	model of the M2x10 screw
	perko.CATPart	model of the leaf spring
	Piezo_5x5x0.5	model of the piezoceramic 5x5x0.5 mm
	prichyt.CATPart	model of the mirror base
	pruzina.CATPart	model of the leaf spring
	saf_pulval.CATPart	model of the sapphire halfrod
	Zrcadla.CATProduct	assembly of the mirror system
	Zrcadlo.CATPart	model of the mirror
DRAWINGS		
	zrcadla_design_I.dwg	mirror rotation system design I
	xyz_motion_system.dwg	x,y,z motion system

Bibliography

[1] BINNIG, G., QUATE, C., F., GEBER, C.: Atomic force microscope, *Phys. Revol. Lett.*, 1986, vol. 56, p. 930-933, ISSN 0031-9007

[2] MEYER, E., HUG, H., J., BENNEWITZ, R.: *Scanning Probe Microscopy, The Lab on a Tip*, Berlin, Heidelgerg: Springer-Verlag, 2004, p. 8-86, ISBN 978-3540431800

[3] MIRONOV, V. L.: *Fundamentals of the scanning force microscopy*, The textbook for students of the senior courses of higher educational institutions, Nizhnyj Novgorod, The Russian academy of science, Institute of physics of microstructures, 2004, p. 6-85

[4] ISRAELACHVILI, J. N.: *Intermolecular and Surface Forces*, New Work: Academic Press, 1991, p. 4-18, ISBN 0-12-375181-0

[5] SAINT JEANT, M., *et. al.*: Van der Waals and capacitive force in atomic force microscopes, *J. Appl. Phys, vol. 86*, 1999, vol. 86, p. 5245 5248, ISSN 0021-8979

[6] FEYMAN, R. P., LEIGHTON, R. B., SANDS, M.: *Feynmanovy přednášky z fyziky 1/3*, Praha: Fragment, 2000, p. 177, ISBN 0-201-02116-1-P

[7] KŘENEK, V.: *Návrh ultravakuového sondového mikroskopu AFM*, [diploma thesis], BUT, FME, Brno University of technology, 2003, p. 50-62

[8] LOPOUR, F.: *Návrh zařízení pro sledování povrchů pevných látek v podmínkách ultravakua metodou STM/SFM*, [diploma thesis], Brno: BUT, FME, 1997, p. 23-42

[9] datasheets of Veeco AFM/SPM system, downloadable from: <http://www.veeco.com/products/Metrology_and_Instrumentation/AFM___SPM/ >, 4.3.2008

[10] Omicron NanoTechnology GmbH, *Multi-mode UHV Scanning Probe Microscope*, datasheet, downloadable from: <http://omicron.de/products/spm/room_temperature/uhv_afm_stm/media/uhv_afm_stm_1.pdf>, 4.3.2008

[11] RUGAR, D., *et al.*: Force Detection of Nuclear-Magnetic-Resonance, *Science*, 1994, vol. 264, p. 1560 1563, ISSN 0036-8075

[12] MIDZOR, M. M., *et al.*: Imaging mechanisms of force detected FMR microscopy, *J. App. Phys.*, 2000, vol. 87, p. 6493-6495, ISSN 0021-8979

[13] GEISSIBL, F. J.: Atomic resolution of silicon(111)7x7 by atomic force microscopy though repulsive and attractive forces, *Science*, 1995, vol. 267, p. 68-71, ISSN 0036-8075

[14] MANALIS, S. R., MINNE, S. C. and QUATE, C. F.: Atomic force microscopy for high speed imaging using cantilevers with an integrated actuator and sensor, *Appl. Phys. Lett.*, 1996, vol. 68, p. 871-873, ISSN 0003-6951

[15] MANALIS, S. R.: High-speed atomic force microscopy using an integrated actuator and optical lever detection, *Rev. Sci. Instrum.*, 1996, vol. 67, 3294-3297, ISSN 0034-6748

[16] Veeco, *MSNC-MFM - Microlever Probes - Cobalt Coated*, data sheet downloadable from: <https://www.veecoprobes.com/probe_detail.asp?ClassID=83>, 4.3.2008

[17] Veeco, *MESP - ESP Series Probes - Cobalt/Chrome Coated*, data sheet, downloadable from: <https://www.veecoprobes.com/probe_detail.asp?ClassID=31>, 4.3.2008

[18] NT-MDT,*NSG01_DLC_10*,data sheet, downloadable from: <http://www.ntmdt-tips.com/catalog/dlc/products/NSG01_DLC_10.html>, 5.3.2008

[19] SADER, J. E.: Parallel beam approximation for V-shaped atomic force microscope cantilevers, *Rev. Sci. Instr.*, 1995, vol. 65, p. 4583-4587, ISSN 0034-6748

[20] SADER, J. E.: Calibration of rectangular atomic force microscope cantilevers, *Rev. Sci. Instr.*, 1995, vol. 66, p. 4583–4587, ISSN 0034-6748

[21] Nanosensors™, probe catalogue, downloadable from: <http://nanosensors.com/products_catalog.html>, 5.3.2008

[22] Veeco, eshop, <https://www.veecoprobes.com/probes.asp>, 5.3.2008

[23] NT-MDT, eshop, <http://www.ntmdt-tips.com/index.php>, 5.3.2008

[24] SAYA, D., *et al.*: Fabrication of single-crystal Si cantilever array, *Sens. and Act. A*, 2002, vol. 95, p. 281-287, ISSN 0924-4247

[25] JOACHIMSTHALER, I., HEIEDERHOFF, R. and BALK, L. J.: A universal scanning-probe-microscope-based hybrid system, *Meas. Sci. Tehnol.*, 2003, vol. 14, p. 87-96, ISSN 0957-0233

[26] Nanonics Imaging Ltd., *Transparently combining SEM, TEM & FIBs with AFM/SPM & NSOM*, data sheet, downloadable from: <http://nanonics.co.il/files/b58edbaf682f19fd33a9bb5a9c6eca1b.pdf>, 1.4.2008

[27] BRABEC, C. J., *et al.*: Origin of the open circuit voltage of plastic solar cells, *Adv. Funct. Mater.*, 2001, vol. 11, p. 374-380, ISSN 1616-301X

[28] SPANGGAARD, H., and KREBS, F. C.:, A brief history of the development of organic and polymeric photovoltaics, *Solar Energy Materials & Solar Cells*, 2004, vol. 83, p. 125-146, ISSN 0927-0248

[29] MICHAILETCHI, V. D., *et al.*: Photocurrent Generation in Polymer - Fullerene Bulk Heterojunction, *Phys. Rev. Lett.*, 2004, vol. 93, p. 23 31, ISSN 0031-9007

[30] SAVENIJE, T. J., *et al.*: Mobility and decay kinetics of charge carriers in photoexcited PCBM/PPV blends, *Phys. Rev. B*, 2004, vol. 69, ISSN 1098-0121

[31] GLATZEL, T., *et al.*: Kelvin Probe Force Microscopy Study of Conjugated Polymer/Fullerene Organic Solar Cells, *Jpn. J. Appl. Phys.*, 2005, vol. 44, p. 5370-5373, ISSN 0021-4922

[32] BARTH, S., *et al.*: Extrinsic and intrinsic dc photoconductivity in a conjugated polymer, *Phys. Rev. B*, 1997, vol. 56, p. 3844-3851, ISSN 0163-1829

[33] GOMMANS, H. H. P., *et al.*: Field and temperature dependence of the photocurrent in polymer/fullerene bulk heterojunction solar cells, *Appl. Phys. Lett.*, 2005, vol. 87, ISSN 0003-6951

[34] KEMERINK, M., *et al.*: Temperature-dependent built-in potential in organic semiconductor devices, *Appl. Phys. Lett.*, 2006, vol. 88, ISSN 0003-6951

[35] http://en.wikipedia.org/wiki/Solar_cell, 1.8.2007

[36] HALLS, J. J. and FRIEND, R. H.: *Clean Electricity form Photovoltaics*, edited by ARCHER, M. D. and HILL, R., London: Imperial College Press, 2001, p. 14-24, ISBN 18-609-4161-3

[37] GRÄTZEL, M.: Photoelectrochemical cells, *Nature*, 2001, vol. 414, p. 338-344, ISSN 0028-0836

[38] TANG, C. W.: 2-layer organic photovoltaic cell, *Appl. Phys. Lett.*, 1986, vol. 48, p. 183-185, ISSN 0003-6951

[39] YU,G., PAKBAZ, K. and HEEGER A. J.: Semiconducting polymer diodes - large-size, low-cost photodetectors with excellent visible-ultraviolet sensitivity, *Appl. Phys. Lett.*, 1994, vol. 64, p. 3422-3424, ISSN 0003-6951

[40] HAGFELDT, A. and GRÄTZEL, M.: Light-induced redox reactions in nanocrystallinge systems, *Chem. Rev.*, 1995, vol. 95, p. 46-68, ISSN 0009-2665

[41] KIRSCH, P. D., *et al.*: Nitrogen interface engineering in Al_2O_3 capacitors for improved thermal stability, *J. Vac. Sci. Technol. B*, 2004, vol. 22, p. 2462-2466, ISSN 1071-1023

[42] LI, W., *et. al*: Breakdown mechanism of Al_2O_3 based metal-to-metal antifuses, *Solid-State Electronics*, 2000, vol. 44, p. 1557-1562. ISSN 0038-1101

[43] KROEZE, J. E., SAVENIJE, T. J. and WARMAN, J. M.: Electrodeless determination of the trap density, decay kinetics, and charge separation efficiency of dye-sensitized nanocrystalline TiO_2, *J. Am. Chem. Soc.*, 2004, vol. 126, p. 7608-7618. ISSN 0002-7863

[44] NONNEMACHER, M., O´BOYLE, M. P. and WICKRAMASINGHE, H. K.: Kelvin probe force microscopy, *Appl. Phys. Lett.*, 1991, vol. 58, p. 2921-2923. ISSN 0003-6951

[45] KIKUKAWA, A., HOSAKA, S. and IMURA, R.: Vacuum compatible high-sensitive Kelvin probe force microscopy, *Rev. Sci. Instrum*, 1996, vol. 67, p. 1463-1467. ISSN 0034-6748

[46] KITAMURA, S. and IWATSUKI, M.: High-resolution imaging of contact potential difference with ultrahigh vacuum noncontact atomic force microscope, *Appl. Phys. Lett.*, 1998, vol. 72, p. 3154-3156. ISSN 0003-6951

[47] *Electric Techniques on MultiMode*^{TM} *Systems*, Support Note 231, Revision E, Veeco Metrology Group

[48] OUISSE, T., *et. al*: Theory of electric force microscopy in the parametric amplification regime, *Physical Review*, 2005, vol. 71, 205404. ISSN 1098-0121

[49] FEI, *Inspect F FEG SEM for high-resolution material inspection and characterization*, data sheet, downloadalbe from: <http://www.fei.com/uploadedFiles/Documents/Content/2006_06_InspectF.pdf>, 30.4.2008

[50] NEBESÁŘOVÁ, J., *Elektronová mikroskopie pro biology*, p. e-book, downloadable from: <http://www.paru.cas.cz/lem/book/Podkap/1.0.html>, 23.4.2008

[51] REICHELT, R., *Science of Microscopy*, chapter *Scanning Electron Microscopy*, edited by: HAWKES, P. W. and SPENCE, J. C. H., Springer Science+Bussines Media, LLC, New York, 2007, p. 137-191. ISBN 0-387-25296-7

[52] <http://en.wikipedia.org/wiki/Electron_microscope>, 22.4.2008

[53] LENC, M. and LENCOVÁ, B., *Metody analýzy povrchů, Elektronová mikroskopie a difrakce*, chapter *Optické prvky elektronových mikroskopů*, edited by: ECKERTOVÁ, L. and FRANK, L., Academia, Praha, 1995, p. 20-89

[54] LENCOVÁ, B., *Částicová optika*, students learning text, p. 1-14, downloadable from: <http://www.isibrno.cz/~bohunka/co2004.pdf>, 28.4.2008

[55] HULÍNSKÝ, V. and JUREK, K., *Zkoumání látek eletronovým paprskem*, SNTL - Nakladatelství technické literatury, Praha, 1982, p. 111-258. ISBN 04-817-83

[56] Kimball Physics Inc., homepage, downloadable from: <http://www.kimphys.com/cathode/cath_prod.htm>, 7.5.2008

[57] Tescan, s.r.o., Mira overview, downloadable from: <http://www.tescan.com/cz/an_mira2.html>, 1.4.2008

[58] KLEINDIEK, S., *et. al*: Miniature three-axis micropositioner for scanning proximal probe and other applications, *J. Vac. Sci. Technol. B*, 1995, vol. 13, p. 2653-2656. ISSN 1071-1023

[59] KALINA, P., *Návrh rastrovacího tunelového mikroskopu s inerciálním krokovým motorem*, [diploma thesis], Brno: BUT, FME, 2006, p. 37-48

[60] LewVac LLP, *DATA SHEET - A-H27D*, data sheet, downloadable from: <http://www.lewvac.co.uk/index_files/a-h27d.pdf>, 9.4.2008

[61] ANTOŠ, S., *Vývoj UHV AFM*, [diploma thesis], Brno: BUT, FME, 2006, p. 69-82

[62] AlioIndrustries, *AI-HR4-10000E-XY data sheet*, data sheet, downloadable from: <http://www.alioindustries.com/docspdfs/OPEN_MOTOR_LINEAR_STAGES/100MM_STAGES/LINEAR_ALIO_Open_Motor_Linear_Precision_SERVO_STAGE_AI-HR4-10000E-XY.htm>, 9.4.2008

[63] PAVELEC, J., *Vývoj UHV STM/AFM*, [bachelor thesis], Brno: BUT, FME, 2008

[64] Nanosensors™, *AdvancedTEC™ Silicon-SPM-Probes*, data sheet, downloadable from: <http://nanosensors.com/AdvancedTEC.pdf>, 17.4.2008

[65] Nanonics Imaging Ltd., *Optical Fiber AFM Probes*, product overview, downloadable from: <http://nanonics.co.il/optical-fiber-afm-probes.html>, 17.4.2008

[66] BAIKIE, I. D., *et. al*: Noise and the Kelvin method, *Rev. Sci. Instrum*, 1991, vol. 62, p. 1326-1332. ISSN 0034-6748

[67] JACOBS, H. O., KNAPP, H. F. and STEMMER, A.: Practical aspects of Kelvin probe force microscopy, *Rev. Sci. Instrum*, 1999, vol. 70, p. 1756-1760. ISSN 0034-6748

[68] SOMMERHALTER, CH., *et. al*: Kelvin probe force microscopy in ultra high vacuum using amplitude modulation detection of the electrostatic forces, *Applied Surface Science*, 2000, vol. 157, p. 263-268. ISSN 0169-4332

[69] CRAIG, P. P. and RADEKA, V.: Stress Dependence of Contact Potential: The ac Kelvin Method, *Rev. Sci. Instrum*, 1970, vol. 41, 258–264. ISSN 0034-6748

[70] ERTL, G. and KÜppers, J. *Low Energy Electron and Surface Chemistry*, Monographs in Modern Chemistry 4, Verlag Chemie, Weinheim, 1974, p. 111-115. ISBN 08-957-3065-0

[71] MAEDO, T. and SAITO, S.: Work Function and Dipole Barrier of Sputter-Cleaned Fe-Ni Alloy Surfaces, *Jpn. J. Appl. Phys.*, 1986, vol. 25, 1623-1627. ISSN 0021-4922

[72] LENERS, K. H., KEARNEY, R. J. and DRESSER, M. J.: Stress-dependent contact potential in copper, *Phys. Rev. B*, 1972, vol. 6, p. 2943-&

[73] McCORMICK, K. L., *et. al*: Scanned potential microscopy of edge and bulk currents in the quantum Hall regime, *Phys. Rev. B*, 1999, vol. 59, p. 4654-4657. ISSN 0163-1829

[74] MATUROVÁ, K., KEMERINK, M. and JANSSEN, R. A. J.: Scanning Kelvin Probe Microscopy on operational organic solar cells, to be published in *App. Phys. Lett.*

[75] MÉLIN, T., *et. al*: Probing nanoscale dipole-dipole interactions by electric force microscopy, *Phys. Rev. Lett.*, 2004, vol. 92, 166101. ISSN 0031-9007

[76] BOYEL, M. G., FENG, L. and DAWSON, P.: Sharp gold tips for light emission in scanning tunneling microscopy: safe etching protocol, [unpublished]

[77] BRYANT, J., *et. al*: Technique for shaping scanning tunneling microscope tips, *Rev. Sci. Instrum*, 1987, vol. 58, p. 1115-1115. ISSN 0034-6748

[78] ABBOU, J., *et. al*: Fabrication of submicrometer-sized gold electrodes of controlled geometry for scanning electrochemical-atomic force microscopy, *Anal. Chem.*, 2002, vol. 74, p. 6355-6363. ISSN 0003-2700